Master Thesis

CFD simulations of the flow around a tanker in shallow water with muddy seabed

K. Leijs

Delft University of Technology

Master Thesis

CFD simulations of the flow around a tanker in shallow water with muddy seabed

by

K. Leijs

to obtain the degree of Master of Science in Offshore & Dredging Engineering
at the Delft University of Technology,

Student number:	4467175	
Thesis committee:	Dr. ir. G.H. Keetels,	TU Delft
	S. Lovato, MSc.	TU Delft, daily supervisor
	Ir. J.W. Settels,	Maritime Research Institute Netherlands (MARIN), daily supervisor
	Dr. ir. S.L. Toxopeus,	Maritime Research Institute Netherlands (MARIN)
	Dr. ir. P.R. Wellens	TU Delft

Faculty of Mechanical, Maritime and Materials Engineering (3mE)
.
Delft University of Technology

Abstract

Alternative dredging methods could reduce the costs in harbours significantly. However, implementing these would mean ships may have to sail close to or even through a fluid mud layer which can affect the ship manoeuvrability. To guarantee safety, the effect of the fluid mud layer and its mud characteristics on the ship manoeuvrability need to be known. This study has made a step in understanding this effect better.

In order to study the effects of the different mud characteristics on the passing vessels, non-Newtonian models have been implemented in ReFRESCO, the CFD code developed by the Maritime Research Institute Netherlands (MARIN) in collaboration with several non-profit organisations around the world. The objective of this study was to test the ability of ReFRESCO to simulate and assess the influence of a fluid mud layer on the resistance of a ship. RANS simulations are performed for the flow around a KVLCC2 benchmark vessel at model-scale with a depth of h/T=1.2 and a Froude number of Fn=0.064. The fluid mud is modelled with a regularized Bingham model. The simulations are performed with varying mud layer thickness ($h_{mud}/T = 0.1-0.3$), varying mud density ratio ($\rho_{mud}/\rho_{water} = 1.05-1.2$) and varying mud yield stress ($\tau_y = 0-1Pa$). The ship is always sailing in the supercritical regime for the water-mud interface, which means that the internal Froude number Fn_i is always larger than 1.

The results show that the resistance of the ship increases in the presence of a mud layer. This increase is mainly in the pressure resistance. The pressure resistance peaks when the internal Froude number Fn_i approaches one. Therefore, it is suspected that the resistance increase is due to the dead-water resistance and thus is highly dependent on the ship's velocity, the mud layer thickness and the density ratio between water and mud. The influence on the resistance due to yield stress is dependent on the density ratio between the water and mud density. The results suggest that the increase in pressure resistance due to yield stress is due to the viscous pressure resistance component. Surprisingly, the frictional resistance shows little influence due to an increase in mud yield stress.

Preface

This research is the conclusion of the process of obtaining a Masters degree in Offshore & Dredging Engineering at Delft University of Technology. The main objective of this study was to test the ability of the CFD code ReFRESCO to simulate and assess the influence of a fluid mud layer on the resistance of a ship. The knowledge obtained during this research could be applied in further studies into safe navigation in shallow water with a muddy seabed. More insights in this topic could help harbours improve their maintenance dredging to reduce costs, emissions and improve the biodiversity in the harbours.

The research was provided by Delft University of Technology and the Maritime Research Institute Netherlands (MARIN). MARIN has been able to provide me with the resources needed to complete this research. I would like to thank them both for the opportunity.

This research has been a challenge and I would like to thank everybody who has helped me to successfully finish it. First, I would like to thank all of my supervisors, Ir. S.L. Lovato, Ir. J.W. Settels, Dr. ir. G.H. Keetels and Dr. ir. S.L. Toxopeus, for their guidance and support during this process. Especially my two daily supervisors, Ir. S.L. Lovato and Ir. J.W. Settels, who helped me out every single week. Thank you all for your enthusiasm in the subject, you have taught me a lot.

I also would like to thank my friends and family for their love, support and encouragement. During this thesis, they helped me to stay motivated. I feel very lucky to have you all!

I hope you enjoy your reading.

K. Leijs
Delft, April 2021

Contents

Nomenclature

Abbreviations

CFD	Computational Fluid Dynamics
FV	Finite Volume
ITTC	International Towing Tank Conference
RANS	Reynolds-averaged Navier-Stokes
SIMPLE	Semi-Implicit Method for Pressure-Linked Equations
SST	Shear-Stress Transport
TVD	Total Variation Diminishing
UKC	Under Keel Clearance
VOF	Volume-of-Fluid

Greek Symbols

α	Density ratio, ρ_2/ρ_1 where $\rho 2 > \rho_1$.	$[-]$
Δ	Displacement volume	$[m^3]$
ϵ	Rate of dissipation	$[m^2 \cdot s^{-3}]$
$\dot{\gamma}$	Shear rate	$[s^{-1}]$
λ	Wave length	$[m]$
μ	Dynamic viscosity	$[kg \cdot m^{-1} \cdot s^{-1}]$
μ_{app}	Apparent viscosity	$[kg \cdot m^{-1} \cdot s^{-1}]$
μ_T	Turbulent viscosity	$[kg \cdot m^{-1} \cdot s^{-1}]$
ν	Kinematic viscosity, $\nu = \frac{\mu}{\rho}$	$[m^2 \cdot s^{-1}]$
ω	Specific rate of dissipation, $\omega = \epsilon / k$	$[s^{-1}]$
Φ	Fluidisation parameter	$[-]$
ϕ	Generic quantity	$[-]$
ψ	Half-wedge angle	[deg]
$\Psi(r)$	Flux limiter	$[-]$
ρ	Density	$[kg \cdot m^{-3}]$
$\tau, \boldsymbol{\tau}$	Stress tensor	$[Pa]$
τ_y	Yield stress	$[Pa]$
υ	Turbulent length scale	$[m]$

Roman Symbols

B	Ship beam	$[m]$
b	Local blockage factor, $b = \frac{\text{ship's cross section}}{\text{channel cross section}}$	$[-]$
Bm	Bingham number, $Bm = \frac{\tau_y L}{\mu V}$	$[-]$
c	wave celerity	$[m \cdot s^{-1}]$
C_{dw}	Coefficient for force due to the internal wave	$[-]$
C_f	Frictional force coefficient	$[-]$
c_i	Volume fraction of the i · th fluid	$[-]$
$c_{i,crit}$	critical velocity of the internal wave	$[m \cdot s^{-1}]$
C_p	Pressure coefficient	$[-]$
C_v	Viscous force coefficient	$[-]$
$\frac{\partial \mathbf{e}}{\partial t}$	Strain rate	$[s^{-1}]$
$\mathbf{e}$	Strain	$[-]$
$\mathbf{F}$	Forces	$[N]$
F_{dw}	Force due to the internal wave	$[N]$
F_f	Frictional force, tangential forces	$[N]$
Fn	Froude number based on the ship length, $Fn = \frac{V}{\sqrt{gL}}$	$[-]$
Fn_h	Froude number based on water depth, $Fn_h = \frac{V}{\sqrt{gh}}$	$[-]$
Fn_i	Froude number based on the internal wave as defined by Miloh et al. [1], $Fn_i = \frac{V}{\sqrt{g(1-1/\alpha)\frac{h_1 h_2}{h_2/\alpha+h_1}}}$	$[-]$
Fn_n	Critical Froude number of water depth as described by Yeung and Nguyen [2]	$[-]$
F_p	Force due to normal force components, forces due to pressure	$[N]$
F_v	Total viscous force	$[N]$
G	Shear modulus	$[Pa]$
$g, \mathbf{g}$	Acceleration due to gravity ($g = 9.81$ in z-direction)	$[m \cdot s^{-2}]$
h	Total water depth	$[m]$
h^*	Effective depth	$[m]$
I_3	Tensor representation of the Kronecker delta δ_{ij}	$[-]$
K	Consistency parameter	$[kg \cdot m^{-1} \cdot s^{-2+n}]$
k	Turbulent kinetic energy per unit of mass	$[m^2 \cdot s^{-2}]$
k_f	Form factor of a vessel	$[-]$
L	Ship length between perpendiculars	$[m]$
l	Turbulent length scale	$[m]$
M	Mass	$[kg]$
m	regularization parameter	$[s]$

N	Brunt-Vaisala Frequency	$[s^{-1}]$
n	flow index	$[-]$
Ω	Cell volume	$[m^3]$
p	Pressure	$[Pa]$
$\mathbf{R}$	Reynolds stress	$[Pa]$
R_h	Hydraulic radius, $R_h = \frac{\text{cross section area}}{\text{perimeter of the fluid touching solid boundaries}}$	$[m]$
Ri	Richardson number, $Ri \frac{gh}{V^2}$	$[-]$
Rn	Reynolds number, $Rn = \frac{VL\rho}{\mu}$	$[-]$
Rn_e	Effective reynolds number	$[-]$
Rn_y	Yield Reynolds number based on the Bingham model, $Rn_y = \frac{V^2\rho}{\tau_{Bm}}$	$[-]$
$\mathbf{S}$	Rate of strain tensor	$[s^{-1}]$
S	Cell surface	$[m^2]$
σ	Standart deviation	[%]
S_{wa}	Wetted surface of the ship	$[m^2]$
$\mathbf{T}$	Stress tensor	$[Pa]$
T	Ship draught	$[m]$
t	time	$[s]$
$\mathbf{u}$	velocity vector	$[m \cdot s^{-1}]$
U	Uncertainty	[%]
u^+	Non dimensional velocity, $u^+ = \frac{u}{u_\tau}$	$[-]$
U_{crit}	Critical velocity	$[m \cdot s^{-1}]$
U_m	Critical velocity for the mud layer as described by Vantorre [3], $U_m = \sqrt{\frac{8}{27} g h_1 (1 - 1/\alpha)(1 - b)^3}$	$[m \cdot s^{-1}]$
u_τ	Friction velocity, $u_\tau = \sqrt{\frac{\tau_{wall}}{\rho}}$	$[-]$
V	Ship velocity	$[m \cdot s^{-1}]$
V_∞	Inflow velocity	$[m \cdot s^{-1}]$
y^+	Non dimensional distance to the wall, $y^+ = \frac{\rho y_{normal} u_\tau}{\mu}$	$[-]$
y_{normal}	Normal distance between cell centre and the wall	$[m]$

List of Figures

List of Tables

1

Introduction

Ships are amongst the most efficient methods of transport. Despite being much slower than airplanes, emissions and costs per ton-mile are significantly lower. In order to be even more efficient, the capacity of newly built cargo ships has been increasing over the years. As access channels do not as easily grow in size, this could result in manoeuvrability problems and even damage of the vessels. In addition, the depth of access channels often decreases due to incoming sediments from sea and/or river outflows. These sediments form a mud layer on the bottom of the channels which could influence the manoeuvrability and safety of vessels as well.

The mud layers formed could be removed by intensive dredging operations. These operations are not only costly, but also reduce the biodiversity within the harbour [4]. Another option is to stop dredging and impose restrictions on the draft of the vessel, which is again not economically viable for the harbours. The third option is for ships to sail through the mud layer and see whether safety can be guaranteed. Sailing through the mud could help in limiting dredging operations and, since the top mud is often soft, it would hardly damage the ship. Unfortunately, there is limited information of the behaviour of ships sailing through fluid mud. This thesis will examine the effects on the ship resistance due to the presence of a fluid mud layer.

1.1. Background

Safe navigation of ships through shallow waters is ensured by setting a minimum distance between the ship's keel and the bottom, which is called Under Keel Clearance (UKC). When waterways have a muddy seabed, determining the location of the bottom and thus the UKC will be difficult.

The preferred option to select the reference bottom is by using the concept of nautical bottom. PIANC [5] defines this concept as *the level where physical characteristics of the bottom reach a critical limit beyond which contact with a ship's keel causes either damage or unacceptable effects on controllability and manoeuvrability*. The distance between the water surface and the nautical bottom is subsequently called the nautical depth.

The nautical bottom is mostly determined by the rheological behaviour and the density of fluid mud. Fluid mud typically shows non-Newtonian behaviour, which means that the shear stress and the shear rate are not linearly correlated and thus do not follow Newton's law of viscosity. Specifically, fluid mud is shear-thinning, which means the viscosity reduces as stress is applied [6]. In addition, fluid mud is said to have a yield stress, which needs to be surpassed before the fluid mud is able to flow. This is called visco-plastic behaviour [7]. Despite this general description, the behaviour of fluid mud is very dependent on the composition of the mud, which differs around the world. Therefore, the determination of the nautical bottom may differ from one location to another.

Due to this varying mud behaviour, adequate measurements of the fluid mud layer and its characteristics are needed in order to determine the criteria for the nautical bottom as well as to maintain the nautical depth. Laboratory investigation can help in determining the overall characteristics and composition of the mud in the area. Along with this, in-situ surveys are needed. Surveying is often performed with echo-sounding equipment to detect the interface between water and mud. However, this method is used to detect sharp interfaces. Due to the large density gradients, this method is less able to detect the fluid mud layers [8]. In the last decade, techniques have been developed in order to measure in-situ fluid mud properties very quickly. Examples of these techniques are a Rheotune, which uses acoustics to measure the yield stress and density, or a Graviprobe, which can measure the undrained shear strength, which could in the future be linked to the shear strength profile [8]. A recent study also suggests a link between the seismic response of fluid mud and the shear strength [9].

Through the use of such equipment, the nautical depth can be monitored. Adequate monitoring could improve maintenance methods for the nautical depth. McAnally et al. [10] defined two different types of nautical depth: Passive Nautical Depth and Active Nautical Depth. The nautical depth is maintained either with (Active) or without (Passive) modification of the fluid mud. Passive Nautical Depth is practiced in many harbours by setting a density criterion [11, 12]. A form of Active Nautical Depth is found in the port of Emden, Germany, where the yield stress of the mud is set as criterion for the nautical bottom. Here, the fluid is exposed to air, which raises the oxygen levels in the mud. A gel is formed. This gel prevents settlement, making it easier for ships to sail through [10]. These kind of methods are less costly than conservative dredging operations [13, 14]. Therefore, using Active Nautical Depth could be an interesting option for other harbours.

While the composition and thus the behaviour of mud is important, the effects of the mud characteristics on the manoeuvrability of passing vessels needs to be known in order to determine the type and criteria for the nautical depth. One option to determine these effects is by experiments. Multiple full scale field tests have been performed [15–17]. The results of these tests revealed relations between the mud-water interface, the mud layer thickness and the ship behaviour on both manoeuvrability and ship speed. However, full scale tests exhibit high uncertainties since the situation is constantly changing. Little is known about the mud characteristics in these areas and, even if known, there would be a limited amount of data about the relation of the mud characteristics and the ship behaviour.

A more controlled experimental set-up can be found with model tests. Such tests [3, 15, 18, 19] show the influence of the mud layer on the manoeuvrability of vessels. Due to practical constraints, these model tests were performed with a Newtonian substitute for the mud. Therefore, it is not yet clear how the non-Newtonian behaviour of the fluid mud influences the vessels manoeuvrability.

Besides the limitations mentioned above, experiments are time consuming and costly for the amount of information retrieved. Another alternative is to use numerical prediction methods. Zilman and Miloh [20], Zilman et al. [21] performed calculations based on potential theory. According to these calculations, the dead-water phenomenon exists for a body moving with a constant speed over a shallow mud layer. The dead-water phenomenon occurs when sailing through stratified flows. An internal wave is generated at the interface between the fluids which causes an increase in resistance. This wave-making resistance caused by the internal wave is called the dead-water resistance.

More recent calculations based on potential theory regarding this subject were performed by Sano and Kunitake [22]. This research showed that sailing above a thick mud layer with a small keel clearance will result in the increase of wave-making resistance and sinkage. While potential theory gives insights about the wave-making resistance, viscous stresses are neglected.

Computational Fluid Dynamics (CFD) calculations that solve the full Navier-Stokes equations could take the viscous effects into account. Progress has been made with regard to the navigation in confined waters (for example by [23–26]), as well as the navigation through stratified flows with two Newtonian fluids [27, 28]. However, little information is available of a confined stratified flow taking the non-Newtonian behaviour of mud into account.
Gao et al. [29], Kaidi et al. [30] performed Reynolds-averaged Navier-Stokes (RANS) simulations for different types of vessels sailing through shallow water with a muddy seabed. Kaidi et al. [30] looked at the effect of mud density and mud viscosity on the resistance of the vessels. Despite partially using non-Newtonian models for the fluid mud, the effect of yield stress was not discussed. Gao et al. [29] used a single type of mud, while discussing the influence of the speed and mud layer thickness on the resistance of the vessels. The

non-Newtonian behaviour of mud was modelled, however, the effects of this behaviour were not discussed.

The effects of the mud yield stress on vessels sailing through shallow waters with a muddy seabed are not yet clear. Yield stress is already used as a criterion for defining the nautical bottom in some locations. For harbours to generally use this characteristic as a criterion, it is necessary to know more about the effect of mud yield stress on the behaviour of the vessels. One of the aims of this study is therefore to get more clarity on these effects.

1.2. Objectives

This study aims to get more insights about the effects of the yield stress of a fluid mud layer on passing vessels. A better knowledge about the the combined effect of yield stress and density of the fluid mud layer will help to optimise dredging activities, which will eventually lead to a reduction of costs and environmental impact.

In order to study the effects of the different mud characteristics on the passing vessels, non-Newtonian models have been implemented in ReFRESCO (www.refresco.org), the CFD code developed by the Maritime Research Institute Netherlands (MARIN) in collaboration with several non-profit organisations around the world. The Herschel-Bulkley model implemented in the code is used to model the shear-thinning and visco-plastic behaviour of mud. Therefore, simulations in ReFRESCO could give insight in the combined effect of wave-making resistance, rheology and the viscous forces. The code has already been successfully tested on non-Newtonian flows such as Poiseuille flow and the laminar flow around a sphere. ReFRESCO can now be tested on a more realistic maritime application such as the flow around a ship sailing above or through a mud layer.

The main objective for the thesis is to test the ability of ReFRESCO to simulate and assess the influence of the mud characteristics on the forces acting on a ship. Furthermore, more insights about the relation between the mud characteristics and the forces on the ship can be obtained. This knowledge is valuable when making decisions about the nautical bottom. Therefore, the main research question that needs to be answered is the following:

How does mud density, rheology and thickness affect the forces on a cargo ship moving at different speeds over a muddy seabed?

The main question is addressed by answering three subquestions:

- *How does yield stress affect the forces on a ship?*
- *How does yield stress in combination with changing density affect the forces on a ship?*
- *How is the water-mud interface influenced by the mud yield stress?*

The yield stress can be used as a parameter to decide the nautical bottom, as already done in the harbour of Emden. Most harbours, however, use a critical density as a deciding parameter for the nautical bottom [10]. When deciding the critical parameter, it is necessary to know the combined effect of yield stress and density. Unfortunately, this is not yet clear looking at the current literature. The first and second subquestions are therefore set in place to determine the effect of yield stress as well as this combined effect.

In addition, the internal wave will influence the resistance of the vessel due to the dead-water phenomenon. This can be visible in the wave-pattern of the mud-water interface. Therefore, the last subquestion will look at the influence of yield stress on the wave-pattern.

1.3. Approach

The approach to answer these questions is by simulating a ship sailing above a layer of fluid mud. When sailing above a layer of fluid mud, a number of parameters will influence the forces on the ship:

- mud rheology (yield stress, molecular viscosity)
- mud density
- mud layer thickness
- UKC
- velocity

When determining the research problem, the effects of yield stress, viscosity, density, mud layer thickness, and velocity are taken into account. For the research, the ship sails at a rather low Froude number ($Fn < 0.1$). Therefore, the effect air-water interface is assumed to be negligible and only one interface (water-mud) is modelled.

The problem of a ship sailing through shallow muddy waters is visualised in Fig. 1.1. For the water layer, the subscript is 1, whereas the properties of the fluid mud layer are always indicated with 2. The ship used for this research is the KVLCC2 (www.simman2008.dk). Since no drift angles are taken into account, the simulation were performed only on half of a domain.

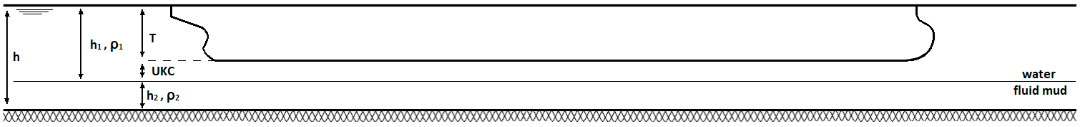

Figure 1.1: Schematic drawing of a ship sailing in shallow water with a muddy seabed.

The simulations are performed at model scale, which means the boundary layer thickness δ/L around the hull is larger. Therefore, less cells are needed in the boundary layer and this will reduce the computational costs. The results will not be scaled to full scale since it is not yet clear how the effects due to yield stress scale. Further research needs to address the scaling for this kind of flow.

Nevertheless, the research objective is to test the ability of ReFRESCO to simulate the flow around ships sailing in the presence of mud as well as finding a relation between the forces and the mud characteristics. These objectives can, to some extent, be achieved regardless of the scale. The main particulars of the KVLCC2 hull are shown in Table 1.1.

Table 1.1: The main particulars of the KVLCC2

Description	Full scale	Model scale	unit
Length between perpendiculars L_{pp}	320	7	m
Moulded breadth B	58	1.269	m
Moulded draught T	20.8	0.455	m
Displacement volume Δ	312635	3.273	m^3
Wetted surface area of the bare hull S_{wa}	27197	13.01	m^2

The simulations are divided into two parts: single-phase and the two-phase simulations. The single-phase simulations will focus on the ship sailing through shallow water domain with only mud. The yield stress is increased to see a trend between the forces and the yield stress without the presence of a wave. The velocity used in these simulations is $V = 0.53\ m{\cdot}s^{-1}$ ($Fn = 0.064$, $Fn_h = 0.23$ and $Re = 3.71{\cdot}10^6$ sailing through only water).

The grids used in the single-phase simulations will also be used to approximate the discretisation uncertainties. These uncertainties give an indication on the quality of the grids. For the two-phase simulations a similar grid is used with refinement around the mud-water interface to accommodate free surface effects.

The two-phase simulations are performed to see the combined effect of the stratified flow and the rheological changes. Simulations are performed with constant velocity equal to the velocity used in the single phase simulations.

1.4. Outline

This report is divided into seven chapters. In Chapter 2, an overview of the underlying physics of the problem is given. The underlying physics of sailing through fluid mud can be divided into three simpler subproblems: navigation in shallow water, navigation through stratified flow and physics of mud.

The modelling strategies can be found in Chapter 3 and the numerical techniques used for the simulations are discussed in Chapter 4. The mathematics and software are discussed by explaining the modelling strategies and the numerical techniques involved in CFD and in particular ReFRESCO. The importance of these two sections is in understanding the value of the results as well as explaining the calculation strategy.

The results of the single-phase simulations can be found in Chapter 5. Chapter 6 focusses on the two-phase simulations: water and mud. Finally, the conclusions of this work and the recommendations for future research are given in Chapter 7.

This thesis has multiple appendixes. In Appendix A, scaling rules are discussed. The grid generation is discussed in Appendix B. The influence of the position of the inlet was checked and the results can be found in Appendix C. Appendix D will elaborate on the descretisation uncertainties in the pressure resistance. The influence of the regularisation parameter, used for the modelling of fluid mud, on the resistance is discussed in Appendix E. Lastly, Appendix F and Appendix G show results of additional simulations that were performed but considered of secondary importance with regard to the main conclusions.

2

Physics underlying sailing through fluid mud

This chapter will focus on the physics involved when sailing through shallow muddy waters. The first section will give a brief overview of the composition of ship resistance in general. Second, the effects due to sailing through shallow water are discussed. Following this, general effects of stratified flow are discussed. The fourth section will focus on the non-Newtonian behaviour of mud and the effects on a moving body through such a fluid. This chapter is concluded with a literary review on the total subject.

2.1. Resistance decomposition

The total ship resistance can be divided into two main components. In the presence of a free surface a wave is generated, which causes the wave-making resistance. On the other hand, the viscosity of water causes the viscous resistance. For practical purposes, it is often assumed that the wave-making resistance depends only on the Froude number:

$$Fn = \frac{V}{\sqrt{gL}} \tag{2.1}$$

and the viscous resistance only upon the Reynolds number:

$$Rn = \frac{\rho V L}{\mu} \tag{2.2}$$

V $[m \cdot s^{-1}]$ is the ship velocity, g $[m \cdot s^{-2}]$ is the gravitational acceleration, L $[m]$ is the length of the vessel, ρ $[kg \cdot m^{-3}]$ is the water density and μ $[kg \cdot m^{-1} \cdot s^{-1}]$ is the water viscosity. In reality, both resistance components depend on both numbers [31].

The wave-making resistance can be divided into two components: the wave breaking resistance and the wave pattern resistance. When a vessel sails along a fluid interface, the fluid parcels are removed from there equilibrium position and waves are generated. If waves are too steep, the waves will break and part of the wave energy is dissipated causing the wave breaking resistance. The wave pattern will transport the remaining wave energy, causing the wave pattern resistance.

The viscous resistance consists of four subcomponents: flat plate resistance, roughness effect, form effect on friction and form effect on pressure Larsson and Raven [31]. The flat plate resistance is the friction that is generated by the water flowing along the hull and is in general the most dominating subcomponent. The roughness effect is an additional friction which occurs since the hull is not smooth. In addition, due to the three dimensional shape of the ship, the velocity distribution along the hull changes. The additional friction component due to the form is the form effect on friction.

The last subcomponent is the form effect on the pressure. This is the only component in the viscous resistance that gives a normal force on the vessel instead of a tangential. In an incompressible, inviscid fluid without free surface, the drag of a body is zero. This is known as the d'Alembert's paradox [32]. The pressure at the front of the body and at the aft will cancel each other. However, in a viscous fluid the boundary layer alters the pressure distribution and the forces on the front and aft do not cancel anymore, thus resulting in a resistance [31]. In this report, this resistance is generally referred to as the viscous pressure resistance.

In Chapter 5 and Chapter 6, the resistance is divided into two different components: pressure resistance, which is the sum of the normal forces in longitudinal direction, and the frictional resistance, which is the sum of all the tangential forces. This means that viscous pressure resistance and wave resistance are both subcomponents of the pressure resistance.

2.2. Sailing through shallow water

Shallow-water effects are the effects observed while sailing through shallow waters compared to deep waters. The definition of shallow water depends on the dimensions of a ship and its environment. ITTC Manoeuvring Committee [33] considers shallow water when the depth to draft ratio is below 4 ($h/T < 4$).

As a ship approaches relatively shallow water, the available space below the ship decreases causing the speed below the hull to increase, as shown in Fig. 2.1. According to Bernoulli's equation for steady flow,

$$p_a + \rho g h_a + \frac{1}{2}\rho V_a^2 = p_b + \rho g h_b + \frac{1}{2}\rho V_b^2 = \text{constant} \tag{2.3}$$

an increase in the velocity leads to a decrease in the pressure. This drop in the pressure will cause the ship to sink (*sinkage*). Furthermore, the pressure distribution can change over the length causing a pitch moment adjusting the trim of the vessel. These effects combined are called *squat*.

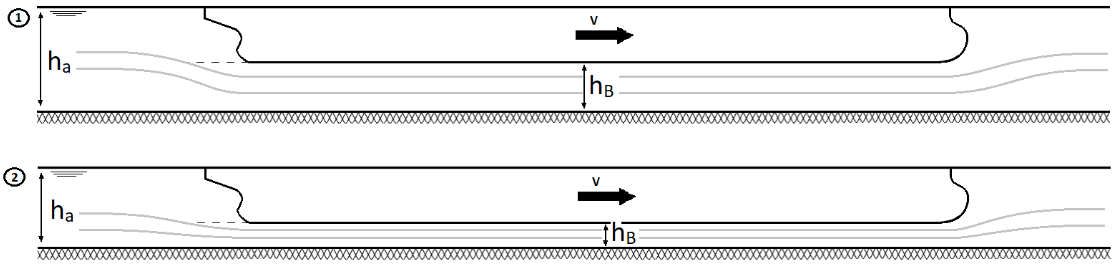

Figure 2.1: Schematic drawing of flow around a hull sailing through seaways with different UKC.

2.2.1. Wave patterns

Shallow water will affect the energy that is transported with the waves. For waves travelling in waters with finite depth, the propagation speed of the wave crest, called wave celerity, can be described by the dispersion relation:

$$c = \sqrt{\frac{g\lambda}{2\pi}\tanh\frac{2\pi h}{\lambda}} \tag{2.4}$$

Here, λ [m] is the wave length and h [m] is the water depth.
The dispersion relation shows the influence of the depth on the wave celerity, and thus on the energy contained in the wave. When the water depth h becomes small, the ratio between the wave length λ and the

depth h becomes very large. The wave velocity will then approach the following limiting value:

$$c = \sqrt{gh} \tag{2.5}$$

With propagation speed c, the wave components in the wave pattern travel in numerous directions. This speed depends on the angle between the direction of the wave and the ships longitudinal axis, called the half-wedge angle. As discussed above, there is an upper limit to wave speed in shallow waters that causes different wave patterns. The Froude number based on the water depth describes the relation between the ship speed and the wave speed:

$$Fn_h = \frac{V}{\sqrt{gh}} \tag{2.6}$$

Based on this value, Larsson and Raven [31] defined the following flow regimes:

- Low subcritical: $Fn_h < 0.7$
- High subcritical: $0.7 < Fn_h < 0.9$
- (Trans) critical: $0.9 < Fn_h < 1.1$
- Supercritical: $Fn_h > 1$

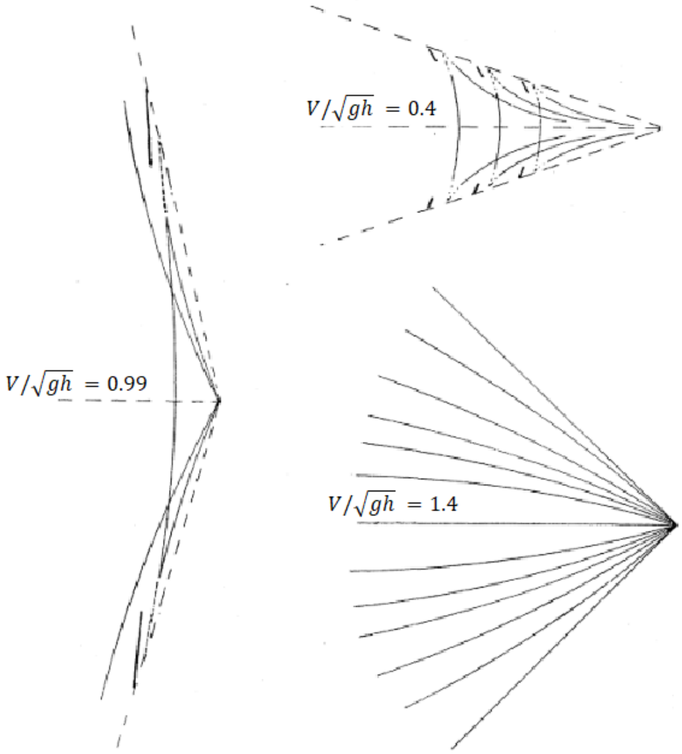

Figure 2.2: wave patterns in subcritical, critical and supercritical regime [34].

For each of these flow regimes the wave patterns are different. The wave patterns in different regimes are shown in Fig. 2.2. When the water depth is more than one-third of the wave length, as in case of the low subcritical regime, there will be no influence on the wave pattern. The wave patterns start to change in the high subcritical regime. The waves will increase in length since the velocity cannot exceed the limited speed for that depth. In addition, the Kelvin wedge, which is the angle between which the waves are contained, will increase. At an angle of around 90 degrees the Kelvin wedge disappears and only the divergent waves will be visible. This will happen around $Fn_h \approx 1$, in the (trans)critical regime. The waves will then move with the maximum wave speed as shown in Eq. (2.5).

In the supercritical, regime the ship speed will be larger than the maximum wave propagation speed. The half-wedge angle is now determined by a ratio of the wave speed and the ship's speed.

2.2.2. Resistance

The previously described shallow water effects will also affect the total viscous force. The increase in velocity around the ship causes an increase in the frictional resistance. The frictional resistance is usually determined using the frictional resistance of a flat plate with the same Reynolds number of the ship and using correlations. Generally, the ITTC57 correlation line is used [35]. However, this correlation line is determined for vessels sailing in deep water.

Zeng [26] computed the flat plate resistance for shallow waters. Since the velocity around the hull increases, the boundary layer is thinner and there is an increase in frictional resistance. For low Reynolds numbers($Re \approx 4 \times 10^5$) the frictional resistance coefficient could even increase by 50% compared to the deep water conditions. To capture the increase in frictional resistance, a new extrapolation method was introduced for sailing through shallow waters [36] (see Appendix A).

In addition to the frictional forces, the viscous pressure forces are also altered by the shallow water effects. The higher velocities around the hull affect the boundary layer and the pressure distribution changes, which is shown in Fig. 2.3. The higher pressure gradients that occur will increase the viscous pressure forces on the vessel [37].

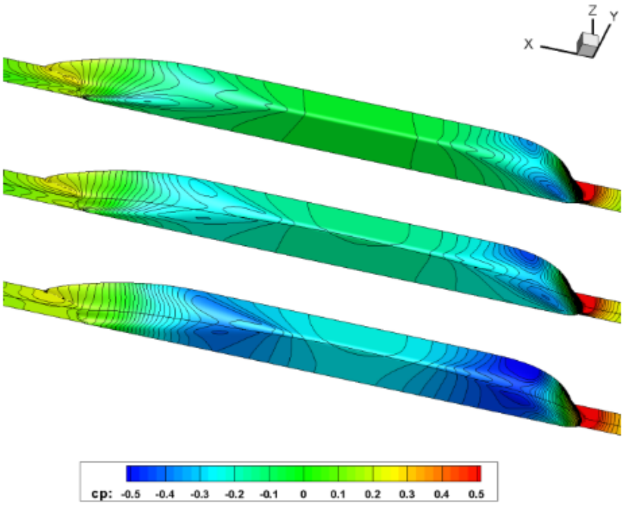

Figure 2.3: Pressure distribution over the hull of a model scale cargo vessel. The top is deep water, the middle has a depth-draft ratio of $h/T = 1.96$ and the bottom has a $h/T = 1.24$. Figure is from Raven [37].

Conventionally, the viscous pressure forces are described as a factor of the frictional resistance called the form factor k_f. In 1989, Millward [38] investigated the change of the form factor due to different water depths by performing model-scale experiments. An empirical correction for the form factor for different water depths was suggested [39]:

$$\Delta k_f = 0.644\left(\frac{T}{h}\right)^{1.72} \tag{2.7}$$

T $[m]$ is the draft of the vessel.

The viscous pressure resistance can then be defined as $(k_f + \Delta k_f) \cdot R_f$, in which R_f $[N]$ is the frictional resistance. Raven [37] and Toxopeus [40] both showed that CFD results are in good agreement with Eq. (2.7).

Both the frictional forces and the viscous pressure forces are dependent on the viscosity. The last resistance component, the wave-making resistance, is also affected when sailing through shallow water. A boundary layer is created on the seabed causing dissipation of a part of the wave energy. Therefore, the wave-making resistance is also dependent on the viscosity, making all resistance components subject to scale effects [26].

2.2.3. Squat

As said above, sinkage and trim effects are part of the shallow water effect under the name squat. Sinkage will occur in the subcritical and critical regime. In the supercritical regime, the ship will experience a rise [41]. The sinkage effects are larger when sailing with a drift angle, since the blockage will increase [42]. The trim effects are mostly visible in the subcritical and critical regimes [43].

Ships sailing through confined waterways will most likely sail in the subcritical regime. Mucha et al. [44], Elsherbiny et al. [45], Bechthold and Kastens [46] all performed CFD calculations to look at the squat of a vessel sailing in the subcritical regime. In these calculations, overall sinkage was always in agreement with experimental results. Trim was either not evaluated or not in agreement with the experimental results. The effect of the propellers on the squat effects was not investigated.

2.3. Sailing through stratified flows

Stratified flows in oceans exist due to changes in salinity, temperature or sediment concentration. These effects lead to density variations over the depth causing the occurrence of internal waves when the stratification is disturbed. These internal waves can affect the ships resistance and manoeuvrability. Looking at stratified flows, there are two parameters that have a dominant effect on the stability of the stratification and eventually the internal wave. The first is the the Brunt-Vaisala Frequency:

$$N^2 = -\frac{g}{\rho_0}\frac{\partial \rho}{\partial z} \tag{2.8}$$

The second is the Richardson Number:

$$Ri_g = \frac{-(\frac{g}{\rho_0}\frac{d\rho}{dz})}{(\frac{du}{dz})^2} \tag{2.9}$$

The origin of the axis system is generally taken at the air-water interface, thus the z-axis is pointing down. The Brunt-Vaisala frequency, also called buoyancy frequency, is the frequency at which a particle will oscillate when moving vertically in a stratified environment. When N^2 is less than zero, the density difference over height is positive (high density at the top, low density below) causing unstable stratification [28]. For a N^2 equal to zero, there is a neutral stratification and when N^2 is positive, there should be a stable stratification. This frequency will become important when looking at an actual density gradient, not for a sharp interface.

The Richardson number gives the ratio between the buoyancy forces and the vertical shear. This vertical shear occurs when two flows with a different density move at different speeds. When the shear becomes dominant, thus decreasing the Richardson number, Kelvin-Helmholtz waves can appear. The Richardson number is in some ways interchangeable with the internal Froude number [47]:

$$Ri = \frac{\Delta\rho}{\rho_0}\frac{1}{Fn_h^2} = \frac{1}{Fn_i} \tag{2.10}$$

Here, Fn_i is the internal Froude number, which characterizes the flow regimes of the internal waves:

$$Fn_i = \frac{V}{c_{i,crit}} \tag{2.11}$$

in which the critical velocity for the internal wave $c_{i,crit}$ is:

$$c_{i,crit} = \sqrt{\frac{\Delta\rho}{\rho_0} g h_0} \tag{2.12}$$

Here, h_0 $[m]$ is the thickness of the upper layer and $\Delta\rho$ is the density difference over height.

The internal waves that are generated in a disturbed stratified flow are similar to the gravity waves at the air-water interface. A difference is that the density gradient within the fluid is much lower than the gradient at the air-water interface, therefore the restoring forces are weaker in stratified flows. This causes internal waves to have longer periods, larger amplitudes and smaller celerity.

Due to the energy needed to generate these waves, the resistance can be affected. If the celerity of the internal wave is close to the speed of the ship, there is a large resistance increase and a loss of manoeuvring capacity. This phenomenon is called the dead-water phenomenon [28].

2.3.1. Wave patterns

For internal waves, there is an upper limit to wave speed. This critical speed of the wave (equation Eq. (2.12)) will influence the wave patterns behind the vessel as well as the wave-making resistance. The flow regimes in which the different wave patterns are formed are similar to the flow regimes for the surface waves in shallow water (see Section 2.2) [48]. While the critical speed, and thus the wave patterns, in shallow water are mostly dependent on the total depth, the critical speed of the internal waves also depends on the density gradients and the layer thickness. In practice, this means the critical speed is often lower for internal waves. The internal waves will also hardly affect the surface waves [49].

Miloh et al. [1] looked at the dead-water effect and the wave pattern in waters with finite depth using potential flow theory assuming that the density difference between the upper and lower layer is very small ($\alpha = \rho_2/\rho_1 \approx 1$, where ρ_1 belongs to the upper layer). Miloh et al. [1] defined the internal Froude number for depth:

$$\begin{aligned} c_{i,crit}^2 &= g(1-\frac{1}{\alpha})\frac{1}{\frac{1}{\alpha h_1}+\frac{1}{h_2}} \\ Fn_i &= \frac{V}{\sqrt{g(1-\frac{1}{\alpha})\frac{h_1 h2}{\frac{1}{\alpha}h_2+h1}}} \end{aligned} \tag{2.13}$$

Here, h_1, h_2 $[m]$ are the different heights of the different layers as shown in Chapter 1.

When the critical Froude number for the internal wave Fn_i is around 0.9 there is a peak in the wave resistance, which explains the dead-water effect. Normally, this peak is expected at a Froude number of 1. However, Miloh et al. [1] describes that the peak is at a lower Froude number due to the inclusion of the shallow water effects in the calculations.

A more elaborated look at the wave patterns in stratified flows of finite depth is given by Yeung and Nguyen [2], who also looked at the coupled motion between the waves. Yeung and Nguyen [2] defined the internal Froude number for finite depth as the following ratio: Fn_n/Fn_h. Here, Fn_h is the Froude number based on depth and Fn_n is defined as:

$$Fn_n^2 = \frac{1}{2} + (-1)^{n+1}\sqrt{\frac{1}{4} - \frac{(1-\frac{1}{\alpha})h_1 h_2}{(h_1+h_2)^2}} \tag{2.14}$$

Here, n specifies which free-surface, where n=1 means the air-water interface and n=2 the free surface of the two fluids.

Fig. 2.4 shows the effects of the relative thickness of the fluids on the half-wedge angle Ψ, as well as the relation between the half-wedge angle and the ratio of the depth Froude number with the critical depth Froude number Fn_n/Fn_h.

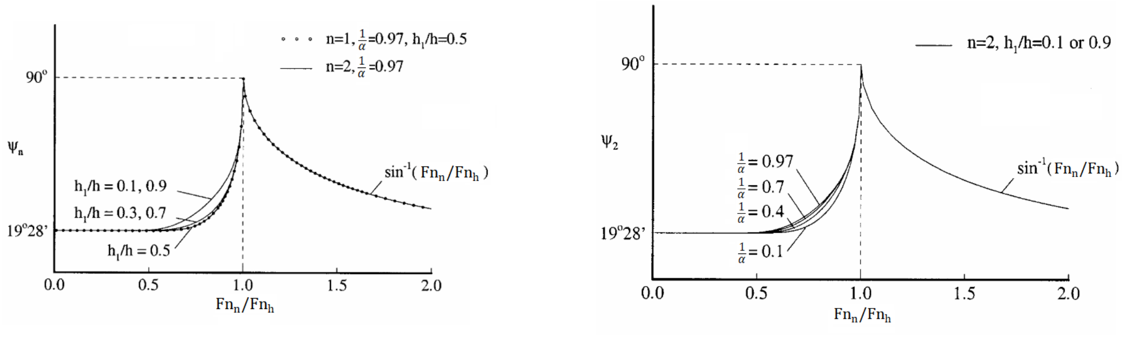

(a) The effect of the layer thickness

(b) The effect of the density ratio $\alpha = \frac{\rho_2}{\rho_1}$

Figure 2.4: The effects of the layer thickness and the density ratio on the half-wedge angle [2].

Radko [50] extended the study of Yeung and Nguyen [2] by using three-layers. An extra relation is shown for a multilayer model:

$$\sum_{i=1}^{n} c_n^2 = gh \tag{2.15}$$

Where c_n $[m \cdot s^{-1}]$ is the critical velocity of the different interfaces n.

The wave amplitude along the crestlines depends on the location of the source compared to the total depth, the thickness of the layers compared to the total depth, the density difference and the Froude numbers [2]. It was concluded that the wave amplitude of the internal wave is largest around the critical regime ($Fn_{n=2} \approx 1$) and will decrease when the source moves further in the supercritical regime. If the UKC or the ratio of h_2/h increase or the density ratio α decreases, the wave amplitude will increase as well.

Literature shows multiple internal Froude numbers. The internal Froude number defined by Miloh et al. [1] describes a two-phase flow without modelling the air-water interface. Since this is the situation modelled in this study, this internal Froude number is used to describe the flow (see Section 6.4).

2.3.2. Resistance

The wave-making resistance due to the internal wave increases significantly in stratified flow. Especially, when sailing around the critical speed of the internal wave, as shown by Miloh et al. [1]. The resistance due to the internal wave seems to be of the same magnitude as the viscous resistance.

The internal wave-making resistance is also called dead-water resistance F_{dw}. Grue [51] showed that in the low subcritical regime ($Fn_i < 0.6$), $F_{dw} \approx 0$, whereas in the high subcritical range of $Fn_i \approx 0.65-0.75$ the dead-water resistance coefficient reached a maximum. The maximum resistance is higher when the keel comes closer to the bottom layer.

Esmaeilpour et al. [28] analysed stratified flow and the dead-water phenomenon by performing RANS calculations. Instead of a sharp interface with respect to density, they modelled a density gradient over height. Calculations were performed for the subcritical regime and the supercritical regime, changing the internal

Froude number $0.64 \leq Fn_i \leq 2.73$ by either changing the velocity of the ship or the depth of the first layer. Their results confirmed the results of Miloh et al. [1] by seeing a large increase in resistance around internal Froude numbers of $0.8 \leq Fn_i \leq 0.9$. An increase in resistance was also noticed when the vessel touched the water layers with a higher density.

When sailing through one homogeneous fluid, the frictional resistance is the largest contributor in the total resistance. [28] also observed that when sailing through a stratified flow the frictional component is not the biggest contributor to the total resistance due to a large increase in pressure resistance. The frictional resistance does still increase up to 30% around an internal Froude number of 0.9. This increase is the result of an acceleration of the flow around the vessel since the pressure changes due to the internal wave.

2.3.3. Dynamic behaviour of a vessel sailing through stratified flow

Sailing through stratified flow with a constant thrust can give additional dynamic behaviour. Mercier et al. [52] performed experiments in which the ship was pulled with a constant force. In this situation, the speed of the vessel and thus the resistance of the ship are free to evolve. The experiments showed fluctuations in speed when sailing with a constant thrust below the critical speed ($Fn_i < 1$), thus a steady state could not be reached.

Fourdrinoy et al. [53] go more in depth on this phenomenon by making a distinction of two different wave resistance phenomena, both named the dead-water phenomenon: Nansen wave-making drag and Ekman wave-making drag. The Nansen wave-making drag causes a constant higher resistance on the ship, whereas the Ekman wave-making drag is responsible for the velocity oscillations shown by Mercier et al. [52]. Fourdrinoy et al. [53] concluded that this phenomenon is caused by an undulating depression produced during the initial acceleration, which causes the unexplained oscillations. The drag caused by this undulation modifies the Nansen wave-making drag until the Ekman wave-making drag becomes negligible. It was also shown that a limited width of the domain amplifies both the Ekman and Nansen wave-making drag. This explains the experimental results of Mercier et al. [52], where the limited width of the tank influenced the measurements.

2.4. Physics of fluid mud

Mud is the name for a cohesive material which contains clay, water, organic matter and a small amount of silt and sand [54]. In estuaries, rivers, mud layers are formed when matter in the water is transported. When the kinetic energy decreases, for instance when the stream slows down or a river widens, this sediment will sink to the seabed. When enough sediment sinks, the concentration of the matter in water increases and mud layers are formed.

Eventually, this mud layer becomes thicker, and the weight causes a pressure on bottom layers that pushes out the water. This process is called consolidation.

Due to the cohesive nature of mud, the clay particles coagulate (stick together) into flocs. Organic matter creates slimes, which will enhance this process. The size of these flocs depends on the experienced forces, which are the hydrodynamic forces, coagulation of particles and the forces due to the composition of the solid. The size of the flocs determines the settling velocity. The settling velocity is the settling flux per unit concentration.

The coagulation of the particles and the settling of the matter, together with external influences, entrainments by the waves and current, influence the concentration profile over the depth causing the existence of multiple layers [7]. The layered structure of sediment is shown in Fig. 2.5.

The top layer is a mixed layer with a low sediment concentration, which behaves as a Newtonian fluid. Below this layer, a more stratified suspension is located with more sentiment particles and thus larger flocs. However, this layer has an insufficient amount of particles to show significant non-Newtonian properties. Going further down, concentration is rising again, causing non-Newtonian behaviour. This mud is called fluid mud, which is a liquid substance that behaves as a thick soup. Going further down, there will be a rigid layer which can be deformed by the waves. Enough deformation can even liquefy this layer, therefore turning it into fluid mud. Below this layer a rigid stationary bed is found.

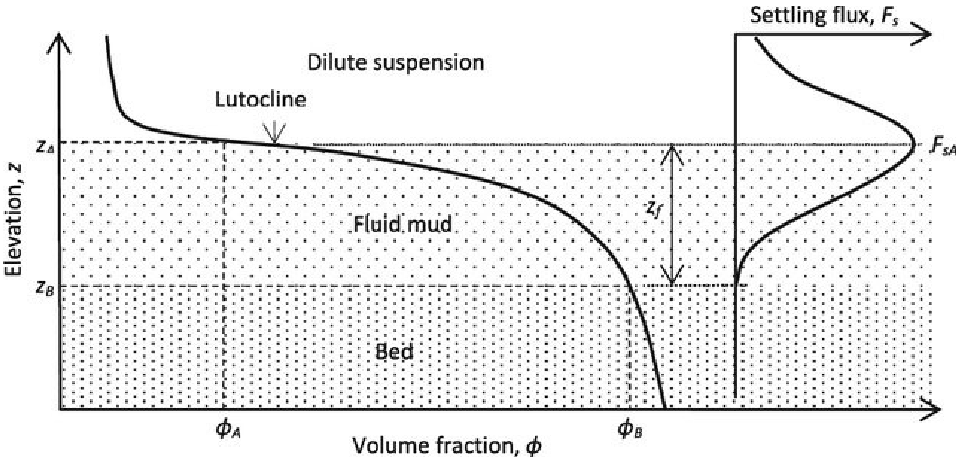

Figure 2.5: Schematic drawing of different layers over the depth of the seaway. The concentration of sediment is increasing with depth, creating these different layers [55].

Fluid mud is formed by fluidisation, which is the opposite effect of consolidation, for which the amount of water in the mud layer increases. This process is for instance used in the maintenance of the Harbour of Emden, as discussed in Section 1.1.

2.4.1. Behaviour of fluid mud

Fluid mud typically exhibits non-Newtonian rheology, as discussed in Section 1.1. The relation between shear stress and shear rate for simple shear flow can be written in the simple form:

$$\tau = \mu_{app}\dot{\gamma} \tag{2.16}$$

in which μ_{app} $[kg \cdot m^{-1} \cdot s^{-1}]$ is the apparent viscosity and $\dot{\gamma}$ $[s^{-1}]$ is the shear rate. When a fluid exhibits Newtonian behaviour, the apparent viscosity will be independent of the shear rate.

For a non-Newtonian fluid, the apparent viscosity μ_{app} is also depending on the shear rate $\dot{\gamma}$. Non-Newtonian fluids/materials can be grouped into three classes:

- time-independent fluid behaviour
- time-dependent fluid behaviour
- visco-elastic behaviour

As said in Section 1.1, mud shows visco-elastic behaviour since it shows characteristics of both solid and fluid [7]. Experiments show that mud is a shear-thinning fluid, which means that the apparent viscosity decreases as the shear rates increase [6]. Furthermore, fluid mud exhibits visco-plastic behaviour. This means a stress level needs to be surpassed in order for the fluid to flow, i.e. the fluid exhibits a yield stress. The shear-thinning and visco-elastic behaviour are visualised in Fig. 2.6.

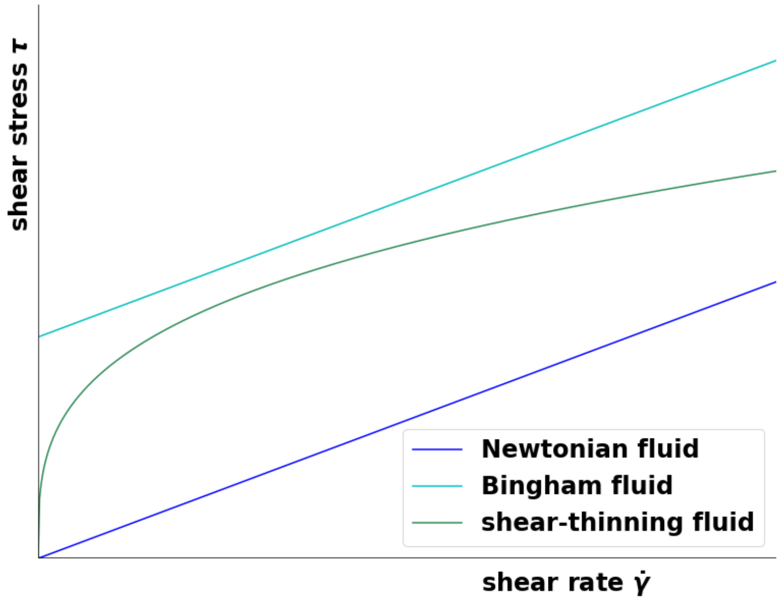

Figure 2.6: Types of flow behaviour.

On top of the shear-thinning and visco-plastic properties, the mud characteristics change over time. When stresses are applied, the fluid mud will decrease in strength. After a period of rest, the fluid mud will regain its strength. This means that the behaviour of the mud also depends on the stress history [6]. This time-dependent behaviour is called thixotropy. This research neglects the thixotropic effects.

The visco-plastic behaviour of a fluid can be described by the Bingham model. The Herschel-Bulkley model can also incorporate the shear-thinning behaviour. Both models are described in Chapter 3. The input of these models are highly dependent on the mud composition. The change of composition, as for instance changing the amount of organic matter, could change the rheological behaviour completely [54]. This is not as surprising since the organic matter is known to create slimes, which prevent the settling of the sediment.

2.4.2. Turbulence within a mud layer

The flow around ships is generally turbulent. Normally, the Reynolds number Rn (see Eq. (2.2)) is used to determine whether a flow is turbulent. For the flat plate, the critical Reynolds number at which the flow transitions to turbulent flow is about $3 \cdot 10^6$ in ideal conditions according to Larsson and Raven [31]. For a visco-plastic fluid in an open channel, the transition range is given by the effective Reynolds number [56, 57]:

$$\frac{1}{Rn_e} = \frac{1}{4 * Rn} + \frac{1}{8 * Rn_y} \tag{2.17}$$

Herein, the local Reynolds number of the channel is determined with the thickness of the fluid mud layer h_2 (for a rectangular channel):

$$Rn = \frac{\rho_2 V h_2}{\mu_2} \tag{2.18}$$

Rn_y is the yield Reynolds number taking the visco-plastic effects into account, using the yield stress τ_y as defined by the Bingham model:

$$Rn_y = \frac{\rho_2 V^2}{\tau_y} \tag{2.19}$$

τ_y $[Pa]$ is the yield stress.

This effective Reynolds number is similar for the effective Reynolds number for a Herschel-Bulkley fluid in open channel flow as described by Haldenwang et al. [58]:

$$Rn_e = \frac{8\rho V^2}{K(\frac{2V}{R_h})^n + \tau_y} \tag{2.20}$$

where R_h $[m]$ is the hydraulic radius, n is the flow index and K $[kg \cdot m^{-1} \cdot s^{-2+n}]$is the consistency parameter. The flow index and the consistency parameter are input to the Herschel-Bulkley model as described in Section 3.2.

For the local Reynolds number of a channel, the transition is expected to be between $10^3 - 10^4$ [32]. Liu and Mei [56] showed that when the effective Reynolds number exceeds 2000-3000, the flow of the fluid mud layer is expected to be turbulent. However, Haldenwang et al. [58] stated that the transition from laminar to turbulence is complex for non-Newtonian fluids, especially at high concentration of sediment. Burger et al. [59] even stated that the transition range of the Haldenwang Reynolds number is found between 5 and 15000. This range is rather broad and shows again that the behaviour of fluid mud is extremely dependent on the composition.

2.5. Sailing through fluid mud

For a more complete application of the nautical bottom criterion, it is necessary to know the effects of sailing through shallow stratified flow where one fluid shows non-Newtonian behaviour.

2.5.1. Experimental results

As already mentioned in Chapter 1, both full scale and model scale experiments have serious challenges when sailing with a bottom layer of fluid mud. Full scale experiments are expensive and difficult to repeat, since the influence on the environment is limited. Model scale experiments are also difficult to repeat because of the thixotropy of mud. Furthermore, it is not clear how to translate model-scale results to full scale because of the complex rheology of mud. Therefore, all results at model scale use a Newtonian alternative for the mud. Despite these disadvantages, experimental results do give an insight into the effects on resistance, squat and the internal wave when sailing through fluid mud.

Resistance seems to always increase in the presence of a mud layer, as shown by the full-scale and model-scale experiments performed by Sellmeijer and Van Oortmersen [15], Brossard et al. [18]. The additional resistance due to the mud layer seems to be larger when the keel touches the mud layer and when the ship is sailing at higher velocities [16].

As explained in Section 2.2, when sailing through shallow water, the vessel experiences squat effects. Sellmeijer and Van Oortmersen [15] reported smaller squat effects in the presence of a fluid mud layer. Brossard et al. [18] also noticed that the ship seemingly climbed up on the mud layer rather than sailing through. This decrease in sinkage due to the presence of a denser layer could be explained by an additional buoyancy effect since the density of mud is higher than the density of water.

Internal waves, as experienced when there is a density difference in the fluid, also occur in the presence of a fluid mud layer. Sellmeijer and Van Oortmersen [15] noticed that for increasing density of the mud layer, increasing UKC or decreasing mud layer thickness, the internal wave height reduces. This is supported by the potential theory results for stratified flow in waters with finite depth (see Section 2.3).

Delefortrie [19] described the same effects on the undulation when performing model tests. In addition, the undulation seemed to increase for lower viscosities. In particular, Delefortrie [19] noticed that undulation seemed to increase with increasing velocity. However, after a certain velocity, the undulation decreased again. At lower speed with low viscosities, mostly a transverse wave is visible. When sailing faster, only a divergent wave is visible. This is similar to the behaviour of surface waves in shallow water, as discussed in Section 2.2. The critical velocity of the internal wave seemed to increase when the viscosity of the mud layer increased [60].

The position of the wave crest at the hull also changes with the velocity. A simplified mathematical model based on the continuity and the Bernoulli equations was compared to model results by Ferdinande and Vantorre [61] and Vantorre [3]. It was shown that the crest will move to the aft of the ship when the velocity increases. At a certain moment, when the ship reaches the velocity U_m,

$$U_m = \sqrt{\frac{8}{27} g h_1 (1 - \frac{1}{\alpha})(1-b)^3} \tag{2.21}$$

in which b is the blockage factor, the elevation is said to appear only behind the hull. It needs to be noted that the simplified model assumes an inviscid fluid. For very viscous mud, this equation is not applicable [62].

Based on model tests, Delefortrie [19] made some simulations in which the manoeuvrability was tested. It showed that, with a decreasing UKC, the turning diameters became larger. However, when the UKC becomes negative, controllability became better and the turning diameter decreased.

In addition, when sailing through a mud layer with a UKC around 0%, the ship experiences instabilities in rudder action, as reported by Ferdinande and Vantorre [61] (model-scale), van Craenenbroeck et al. [16] (model-scale) and Barth et al. [17] (full-scale). The undulation close to the aft seems to influence the inflow for the propeller and rudder causing a change in the propeller efficiency and the above mentioned instabilities in rudder action.

Based on model test results of Delefortrie [19], a mathematical manoeuvring model was created for vessels sailing through the harbour of Zeebrugge. The model has been extended to take into account the effects of the mud by additional forces to correct for the mud effect as well as the determination of the equivalent depth h^*. The equivalent depth is a corresponding depth above the solid bottom, leading to similar forces, which could replace the real depth as the nautical depth. This equivalent depth is determined as:

$$h^* = h_1 + \Phi h_2 \tag{2.22}$$

in which Φ is a fluidisation parameter ranging from 0 (solid mud) to 1 (very fluid mud). It is possible, however, that a really disadvantaged undulation of the mud layer could make the fluidisation parameter go negative. The definition of the fluidisation parameter should be taken with care due to the many assumptions made for this model. However, the definition of equivalent depth could be valuable.

2.5.2. Potential theory

Outside from experimental results, the problem was also studied using the potential flow theory. Zilman and Miloh [20] gave a theoretical overview for linear calculations of the wave resistance of an object moving over a fluid mud layer, assuming the mud to be a Newtonian viscous fluid. Due to the stratified origin, the dead-water phenomenon (see Section 2.3) is visible. A large increase in resistance coefficient is shown around the critical Froude numbers ($Fn_i \approx 0.9$), similar to what is described for stratified flow (see Section 2.3). A small increase in viscosity seems to decrease the wave resistance due to the damping of the waves.

This work is extended by Zilman et al. [21] for ships sailing through all regimes with different channel width and assuming the mud as a visco-elastic substance. They, as well as Miloh [63] and Doctors et al. [64], used the Kelvin-Voight model to model the mud layer:

$$\tau = G\mathbf{e} + \mu_2 \frac{d\mathbf{e}}{dt} \tag{2.23}$$

Here, G $[Pa]$ is the shear modulus of mud, μ_2 $[kg \cdot m^{-1} \cdot s^{-1}]$ is the mud viscosity and $\mathbf{e}$ stand for the shear strain.
Zilman et al. [21] showed that by further increasing the viscosity, the dissipation of the waves becomes negligible and the mud layer becomes as stiff as a solid bottom. In this case, the resistance due to the air-water interface is almost equal to the resistance in a more shallow waterway. The increase in the mud shear stiffness gives a similar effect as increasing the viscosity [63].

Looking at trim and sinkage, a similar effect was observed. Again, for a very rigid mud layer (high viscosities and/or high shear stiffness) the squat effects are comparable to that in a less deep waterway [64]. In addition, smaller domain size increases the squat effects.

Lately, Sano and Kunitake [22] used potential theory for stratified flow with finite depth to determine the wave pattern as well as the wave resistance of a full scale benchmark ship, the KVLCC2, sailing through shallow muddy waters. A large increase in resistance is observed around the critical Froude number as defined by Yeung and Nguyen [2]. This can be associated with the dead-water phenomenon (see Section 2.3).

2.5.3. RANS calculations of ship sailing through shallow water with a muddy seabed

Although potential theory can help understanding the forces due to waves, the viscous effects are neglected. Numerical methods that solve the Reynolds-averaged Navier-Stokes (RANS) equations can help determining the total forces including the viscous forces. For the problem of a ship sailing through shallow water with a muddy seabed, this has already been applied by Gao et al. [29] and Kaidi et al. [30]. The input data used in their calculations are summarised in table Table 2.1.

Gao et al. [29] determined the resistance and the undulation of both interfaces (air-water, water-mud) for the Wigley hull. Both resistance components (pressure and friction) increased with the presence of a mud layer. The pressure resistance became more dominant with the presence of the mud layer, however it was still smaller in magnitude than the frictional resistance. Both resistance components became more significant as the mud layer thickness increased. When the keel touched the mud layer, this increase becomes more significant. Regarding the undulation of both interfaces, Gao et al. [29] concluded that the mud layer thickness would influence the air-water undulation insignificantly.

Kaidi et al. [30] also performed resistance calculations for a ship moving through confined waters with a muddy seabed, where only the water-mud interfaced was modelled. The resistance as well as the undulations do seem to be influenced by the density and the viscosity, as shown in Fig. 2.7.

Kaidi et al. [30] concluded that using the Newtonian model for the mud gives an acceptable estimation of the ships resistance, although the undulation was overestimated. Therefore, all calculations were performed with a Newtonian model for mud. However, it is not clear how the mud rheology was converted to the Newtonian model. Due to this lack of information, the assumption that the Newtonian model for the mud layer gives acceptable results will not be used in this research.

RANS calculations showed that the wave pattern seemed to be influenced by the viscosity [30]. When the viscosity increases, transverse waves seem to appear. This is unexpected, since increasing viscosity was expected to decrease the critical velocity according to potential flow results. Therefore, the flow is more in supercritical regime as viscosity increases. In the supercritical regime, no transverse waves should be visible. Due to the contradicting results, the influence of viscosity on the flow regimes is not yet clear.

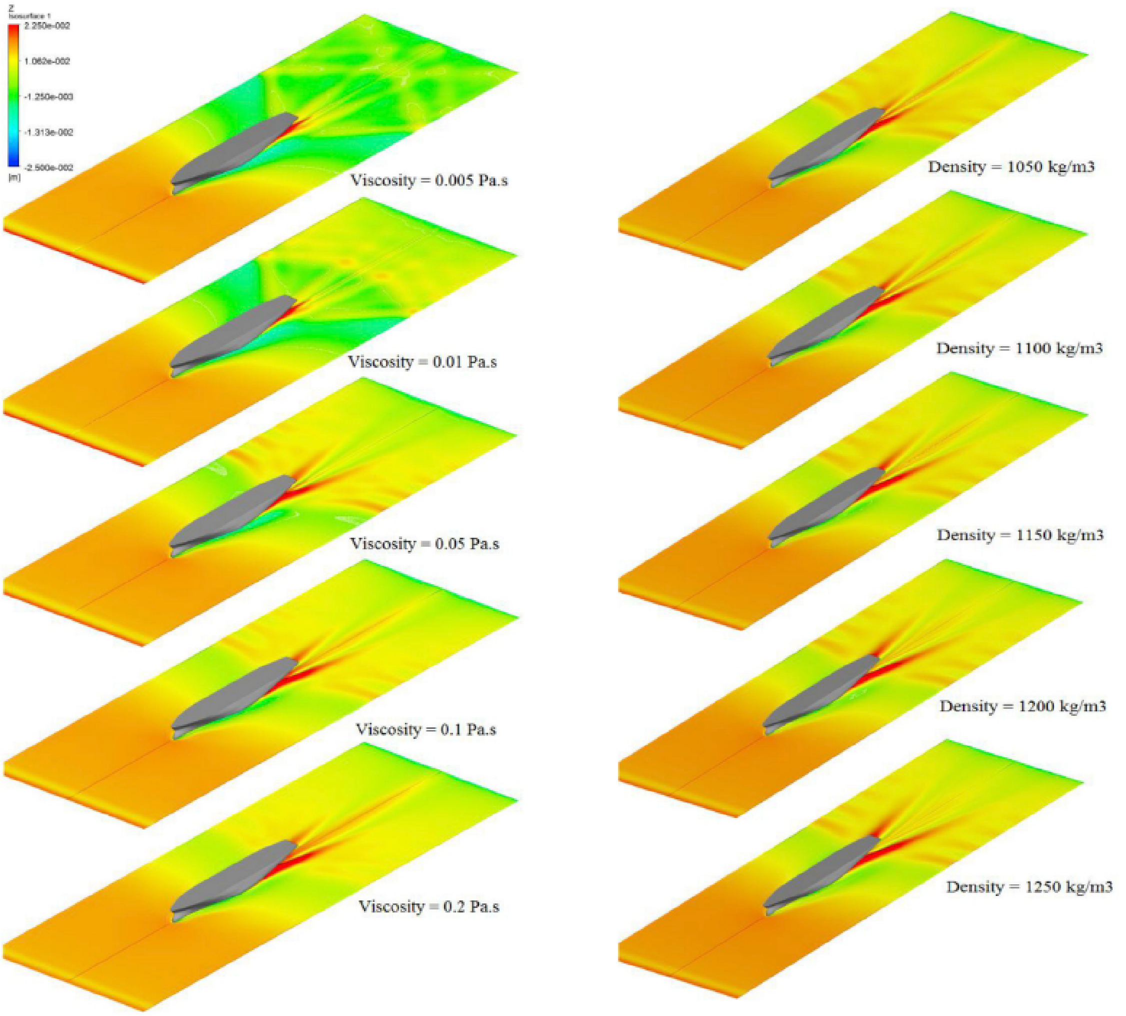

(a) Viscosity variation **(b) Density variation**

Figure 2.7: Internal wave for viscosity variation and density variation obtained by Kaidi et al. [30]. The results are for a case with a depth of $h = 1.2T$ and a mud layer thickness of $h_2/T = 0.3$. For the cases with varying mud viscosity,the mud density is $\rho_2 = 1100\ kg \cdot m^{-3}$. For the cases with varying mud density, the mud viscosity equals $\mu_2 = 0.1\ kg \cdot m^{-1} \cdot s^{-1}$.

Table 2.1: CFD models used when simulating a ship sailing through shallow water with a muddy seabed

Authors	Gao et al. [29]	Kaidi et al. [30]
CFD package:	Ansys-FLUENT 12.0	Ansys-FLUENT 13.0
free surface model	VOF (air-water-mud)	VOF (water-mud)
soil model	Herschel-Bulkley	Herschel-Bulkley
turbulence model	k-ϵ	k-ω SST
specifics grid	Hexahedral grid with +/- 0.75 millions cells	Unknown
non-dimensional first cell height y^+	+/- 30, wall functions are used	Unknown
total water depth	1.2T	1.2T-1.4T
mud layer thickness	0T-0.4T	0-0.3T
Froude number Fn	0.1-0.316	0.02-0.1
depth Froude number Fn_h	0.4-1.26	0.096-0.480
mud density	1256 $[kg/m^{-3}]$	1050-1250 $[kg/m^{-3}]$
mud molecular viscosity	Unknown	0.025-0.260 $[Pa \cdot s]$
mud yield stress	possibly +/- 7 $[Pa]$	Unknown

3

Modelling strategies

This chapter will focus on the modelling strategies involved in the numerical simulations of a ship sailing through shallow water with a muddy seabed. For the non-Newtonian behaviour of mud, the Bingham model is adopted. The water-mud interface is captured with the Volume-of-Fluid (VOF) method, whereas the turbulence is modelled with two eddy-viscosity models: $k-\omega$ SST 2003 and the $k-\sqrt{k}L$.

Before discussing the modelling of the mud, the free surface and the turbulence, the general equations used in the RANS model are explained.

3.1. Governing equations

The laminar single-phase flow of incompressible fluid is governed by the Navier-Stokes equations:

$$\frac{\partial \rho}{\partial t} + \nabla \cdot (\rho \boldsymbol{u}) = 0 \tag{3.1}$$

$$\frac{\partial (\rho \boldsymbol{u})}{\partial t} + \nabla \cdot (\rho \boldsymbol{u}\boldsymbol{u}) = \nabla \cdot \boldsymbol{T} + \rho \boldsymbol{g} \tag{3.2}$$

Here, the $\boldsymbol{u}$ $[m \cdot s^{-1}]$ is the flow velocity vector, $\boldsymbol{g}$ $[m \cdot s^{-2}]$ is the acceleration vector due to gravity and $\boldsymbol{T}$ $[Pa]$ the stress tensor. The stress tensor can be written as:

$$\boldsymbol{T} = -p\boldsymbol{I} + \boldsymbol{\tau} \tag{3.3}$$

For a incompressible Newtonian fluid, the deviatoric stress tensor $\boldsymbol{\tau}$ $[Pa]$, can be rewritten as:

$$\boldsymbol{\tau} = 2\mu \boldsymbol{S} \tag{3.4}$$

in which $\boldsymbol{S}$ $[s^{-1}]$ is the rate of strain tensor:

$$\boldsymbol{S} = \frac{1}{2}(\nabla \boldsymbol{u} + (\nabla \boldsymbol{u})^T) \tag{3.5}$$

Additional information about the Navier-Stokes equation can be found in a number of textbooks such as White [32], Kundu et al. [65], Ferziger et al. [66].

3.1.1. Reynolds-averaged Navier-Stokes (RANS) equations

Solving the NS equations directly for turbulent flow around ships is impossible with the currently available computational power [31]. In addition, not all fluctuations in velocity and pressure obtained from such calculations are needed for practical purposes. A method to eliminate these fluctuations as well as reducing computational effort is with the help of Reynolds' time-averaging concept [32].

A particular flow quantity, such as velocity and pressure, can be expressed as the sum of a mean and a fluctuating part:

$$\begin{aligned} \boldsymbol{u} &= \overline{\boldsymbol{u}} + \boldsymbol{u}' \\ p &= \overline{p} + p' \end{aligned} \tag{3.6}$$

The equations from Eq. (3.6) can be substituted in the Navier-Stokes equations ,Eq. (3.1) and Eq. (3.2). The following averaging rules are applied to the equations:

$$\overline{\phi} = \frac{1}{T}\int_0^T \phi dt \tag{3.7}$$

$$\overline{\phi'} = \frac{1}{T}\int_0^T \phi' dt = \frac{1}{T}\int_0^T \phi - \overline{\phi} dt = 0 \tag{3.8}$$

$$\overline{\phi'^2} = \frac{1}{T}\int_0^T \phi'^2 dt \neq 0 \tag{3.9}$$

Here, ϕ is a particular quantity. Applying these rules will give the Reynolds-averaged Navier-Stokes (RANS) equations.

Assuming that Newtonian fluids are used, the RANS equations can be reduced to:

$$\nabla \cdot \overline{\boldsymbol{u}} = 0 \tag{3.10}$$

$$\frac{\partial(\rho\overline{\boldsymbol{u}})}{\partial t} + \nabla \cdot (\rho\overline{\boldsymbol{v}\boldsymbol{v}}) = -\nabla p + \nabla \cdot (\tau - \boldsymbol{R}) \tag{3.11}$$

The $\boldsymbol{R}$ in this equation is the Reynolds stress, which is given as:

$$\boldsymbol{R} = -\rho \boldsymbol{u}'\boldsymbol{u}' \tag{3.12}$$

To compute the Reynolds stresses, turbulence models are needed. More information about the derivation of the RANS equations as well as turbulence modelling can be found, for example, in the book of Pope [67].

3.2. Modelling of fluid mud

As said in Chapter 2, fluid mud is a visco-elastic fluid showing shear-thinning behaviour as well as visco-plastic behaviour. A simple model to describe the stress-shear relation of fluid mud is the Herschel-Bulkley model in 1D:

$$\tau = \tau_y + K\dot{\gamma}^n \tag{3.13}$$

For this research, the 3D Herschel-Bulkley model was used:

$$\begin{cases} \boldsymbol{\tau} = 2\left[\frac{\tau_y + K\dot{\gamma}^n}{\dot{\gamma}}\right]\boldsymbol{S} \text{ for } \tau > \tau_y \\ \boldsymbol{S} = 0 \text{ for } \tau < \tau_y \end{cases} \tag{3.14}$$

The shear rate is the magnitude of the rate of strain tensor, $\dot{\gamma} = \sqrt{2\boldsymbol{S}:\boldsymbol{S}}$ $[s^{-1}]$, τ_y $[Pa]$ is the yields stress, K $[kg \cdot m^{-1} \cdot s^{-2+n}]$ the consistency parameter and n is the flow index. With $n = 1$, the model is known as the Bingham model [68]. For shear-thinning fluid like mud, $n < 1$ [6]. Coussot and Piau [69] successfully fitted the flow curve of fine mud with the Herschel-Bulkley model, showing a range of n between $0.22 - 0.36$.

Due to the great variations in the content of the mud, it is difficult to generalize the flow properties. Coussot and Piau [69] showed that the behaviour can vary greatly with small changes in clay type, electrolyte concentration, acidity (pH) and solid concentration. Recently, Shakeel et al. [54] also emphasized the influence of the organic matter, as described in Section 2.4.

The Herschel-Bulkley model can capture the shear-thinning and visco-plastic behaviour of mud. However, it is not capable of capturing the thixotropy of mud (see Section 2.4). To take this into account, more complex models are needed. For the current research, the Bingham model and the Herschel-Bulkley model are implemented into the code. Thixotropy is neglected as it is considered of minor importance at this stage of the project.

The model described by Eq. (3.14) is a discontinuous function, which can be made continuous by using regularisation. For this work, the regularisation proposed by Papanastasiou [70] was used. For Bingham fluids, the regularised equation becomes:

$$\boldsymbol{\tau} = 2\left[\frac{\tau_y(1-e^{-m\dot{\gamma}})}{\dot{\gamma}} + K\right]\boldsymbol{S} \tag{3.15}$$

and for the Herschel-Bulkley model:

$$\boldsymbol{\tau} = 2\left[\frac{\tau_y(1-e^{-m\dot{\gamma}}) + K\dot{\gamma}^n}{\dot{\gamma}}\right]\boldsymbol{S} \tag{3.16}$$

Here, m [s] is the regularisation parameter. When this parameter goes to infinity, the regularised model will be exactly the same as the model in Eq. (3.14). The effect of the regularisation on the Bingham model is shown in Fig. 3.1.

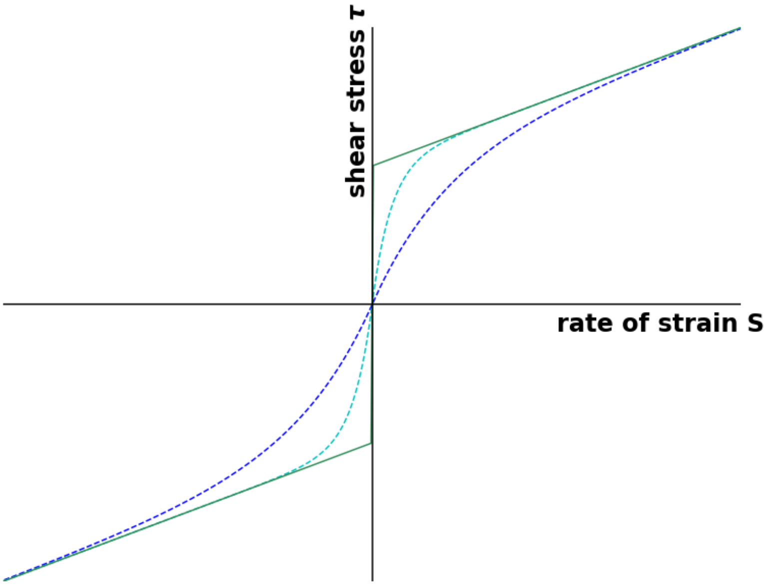

Figure 3.1: Relation of the shear stress and the rate of strain for the Bingham model (solid line), and the regularised model (dashed line).

More information about the implementation of the Herschel-Buckley model in ReFRESCO can be found in the paper of Lovato et al. [71].

3.3. Volume-of-fluid method

The Volume-of-Fluid (VOF) model was used to simulate cases with a free-surface. The model solves another equation in addition to the conservation of mass and momentum, the transport equation for the volume fraction. The density and viscosity of the flow are depending on the volume fraction c_i:

$$\mu = \sum_{i=1}^{n} \mu_i c_i \tag{3.17}$$

$$\rho = \sum_{i=1}^{n} \rho_i c_i \tag{3.18}$$

The volume fraction is a dimensionless variable defined as the volume occupied by a certain fluid divided by the total volume, meaning the volume fraction will vary between 0 and 1. The definition of the volume fraction is given by:

$$c_i = \frac{V_i}{\sum_{i=1}^{n} V_i} \tag{3.19}$$

When assuming incompressible flow, the sum of the volume fractions is equal to 1. Therefore, if there are two phases, only one volume fraction needs to be known. The transport equation for the volume fraction c_i results in:

$$\frac{Dc_i}{Dt} = \frac{\partial c_i}{\partial t} + \mathbf{u} \cdot \nabla c_i = 0 \tag{3.20}$$

The original description of the VOF model can be found in the paper of Hirt and Nichols [72]. More information about the implementation of the VOF model can be found in the paper of Vaz et al. [73] or Klaij et al. [74].

3.4. Turbulence modelling

The Reynolds stresses can be modelled by a turbulence model, either via the turbulent-viscosity hypothesis or more directly from modelled Reynolds-stress transport equations. For current research, the Reynolds stresses are determined via the turbulent-viscosity hypothesis.

The turbulent-viscosity hyposis, introduced by Boussinesq in 1877, assumes the Reynolds stress (see Eq. (3.12)) can be computed from the rate of strain, similar to how the viscous stresses are computed. The Reynolds stresses can then be defined as:

$$\boldsymbol{R} = \mu_T \boldsymbol{S} - 2/3\rho k \boldsymbol{I} \tag{3.21}$$

Here μ_T is the turbulent viscosity (or eddy viscosity) and k is the turbulent kinetic energy per unit mass. Dimensional analysis shows that the turbulent viscosity can be written as the product of one velocity scale v and one length scale l:

$$\mu_T = constant \cdot \rho v l \tag{3.22}$$

Historically, many models have been proposed in order to compute the turbulent quantities. In this research two two-equation models are used: k-ω SST 2003 and the k-$\sqrt{k}L$ (KSKL). In general, two-equation models solve two transport equations for different turbulence quantities.

The SST model is more widely used for external flows compared to the KSKL model. However, a disadvantage of the SST model is that the resulting frictional resistance is very dependent on the near-wall cell size

y^+ [75]. The KSKL model shows less dependence on the near-wall cell size.

More information about the other classes or methods of turbulence modelling can, for example, be found in the book of Pope [67].

3.4.1. k-ω SST-2003

The SST-2003 is a modification on the original SST model [76]. The original SST model is a combination of the well known original k-ϵ and k-ω models.
The SST-2003 solves transport equations for k and for the specific dissipation rate ω:

$$\begin{aligned} \frac{\partial \rho k}{\partial t} + \nabla \cdot (\rho \boldsymbol{u} k) &= \tilde{P_k} - \beta^* \rho k \omega + \nabla[(\mu + \sigma_k \mu_T)\nabla k] \\ \frac{\partial \rho \omega}{\partial t} + \nabla \cdot (\rho \boldsymbol{u} \omega) &= P_\omega - \beta \rho \omega^2 + \nabla[(\mu + \sigma_\omega \mu_T)\nabla \omega] + 2\rho(1 - F_1)\frac{\sigma_{\omega 2}}{\omega}\nabla k : \nabla \omega \end{aligned} \tag{3.23}$$

In these transport equations, μ_T is the eddy viscosity, F_1 is the first blending function and P_w are the production term of the specific rate of dissipation ω, which are defined as:

$$\begin{aligned} \nu_T &= \frac{a_1 k}{\max(a_1\omega, \boldsymbol{S}F_2)} \\ P_\omega &= \frac{\gamma}{\nu_T} P_k \\ F_1 = \tanh\left[\left(\min\left(\max\left(\frac{\sqrt{k}}{\beta^* \omega y}, \frac{500\nu}{y^2\omega}\right), \frac{4\rho\sigma_{\omega 2} k}{CD_{k\omega} y^2}\right)\right)^4\right] \end{aligned} \tag{3.24}$$

where $CD_{k\omega}$ is defined as:

$$CD_{k\omega} = \max\left(2\rho\sigma_{\omega 2}\frac{1}{\omega}\nabla k : \nabla\omega, 10^{-10}\right) \tag{3.25}$$

and the second blending function F_2 is defined as:

$$F_2 = \tanh\left(\max\left(2\frac{\sqrt{k}}{0.09\omega y}, \frac{500\nu}{y^2\omega}\right)\right) \tag{3.26}$$

The production term of kinetic energy $\tilde{P_k}$ is limited to prevent build-up of turbulence in stagnation regions:

$$\begin{aligned} \tilde{P_k} &= \min(P_k, 10\beta^* \rho k \omega) \\ P_k &= T\nabla \cdot \boldsymbol{u} \end{aligned} \tag{3.27}$$

In the SST model, σ_ω, σ_k, β and γ can be determined by the following formula (in which ϕ is one of the given constant described before):

$$\phi = \phi_1 F_1 + (1 - F_1)\phi_2 \tag{3.28}$$

For the SST-2003 model, the constants have the following values:

$$\begin{array}{rrrr} \sigma_{k1} = 0.85, & \sigma_{\omega 1} = 0.5, & \sigma_{k2} = 1, & \sigma_{\omega 2} = 0.856, \\ \beta^* = 0.09, & \beta_1 = 0.0750, & \beta_2 = 0.0828, & a_1 = 0.31, \\ \gamma_1 = 5/9 & \gamma_2 = 0.44 & & \end{array}$$

3.4.2. KSKL

The two-equation model named KSKL solves equations for k and for $\sqrt{k}L$, where L the integral Length. The integral Length is the length of the largest eddies, generated in the production phase. The KSKL model was first developed around 1970, but the model used is a modified version, first introduced in 2005 by Menter [77]. The transport equations are:

$$\begin{aligned}\frac{\partial \rho k}{\partial t} + \nabla\cdot(\rho \boldsymbol{u} k) &= P_k - c_\mu^{3/4}\rho\frac{k^2}{\Phi} + \nabla[(\mu+\frac{\mu_T}{\sigma_k})\nabla k]\\ \frac{\partial \rho \Phi}{\partial t} + \nabla\cdot(\rho \boldsymbol{u} \Phi) &= \frac{\Phi}{k}P_k(\zeta_1 - \zeta_2(\frac{L}{L_{vK}})^2) - \zeta_3\cdot\rho k + \nabla[(\mu+\frac{\mu_T}{\sigma_\Phi})\nabla\Phi] - 6\mu\frac{\Phi}{d^2}f_\Phi\end{aligned} \tag{3.29}$$

Hereby, $\Phi = \sqrt{k}L$, d is the distance to the wall and L_{vK} is the von Karman length:

$$L_{vK} = \kappa\frac{\boldsymbol{S}^2}{\nabla\boldsymbol{S}\times\nabla\boldsymbol{S}} \tag{3.30}$$

The production term of the turbulent kinetic energy is the same as for the k-ω SST 2003 model. The other term f_Φ is defined as:

$$\begin{aligned}f_\Phi &= \frac{1+c_{d1}\xi}{1+\xi^4}\\ \xi &= \frac{\sqrt{0.3k}d}{20\mu}\end{aligned} \tag{3.31}$$

The model uses a blending for the eddy viscosity:

$$\begin{aligned}\nu_T &= min(c_\mu^{1/4}\Phi, a_1 k/D)\\ a_1 &= a_1^{SST}f_b + (1-f_b)a_1^{REAL}\\ f_b &= tanh((\frac{20(c_\mu^{1/4}\Phi+\nu)}{\kappa^2 Dd^2+0.01\nu})^2)\end{aligned} \tag{3.32}$$

as well as a limiter for the von Karman length scale:

$$L/c_{l1} < L_{vK} < c_{l2}\kappa d \tag{3.33}$$

The following constants are used in the model:

$$\begin{array}{rrrr} \zeta_1 = 0.8 & \zeta_2 = 1.47 & \zeta_3 = 0.0288 & \kappa = 0.41\\ \sigma_k = 2/3 & \sigma_\Phi = 2/3 & c_\mu = 0.09 & c_{d1} = 4.7\\ a_1^{SST} = 0.32 & a_1^{REAL} = 0.577 & c_{l1} = 10 & cl2 = 1.3 \end{array}$$

4

Numerical techniques

As said in the introduction, the finite-volume CFD code ReFRESCO (www.refresco.org), which is developed and verified by the Maritime Research Institute Netherlands (MARIN), was used to simulate the ship sailing through shallow water with a muddy seabed. ReFRESCO solves multiphase incompressible viscous flows using the Navier-Stokes equations. The code is complemented with turbulence models and volume-fraction transport equations for different phases.

This chapter is organised in four sections. First, the discretisation methods and schemes are described. Second, the solution methods used are presented. This section is followed by a discussion about the boundary conditions used in this research. Lastly, guidelines about the choice of the computational grid are given

4.1. Discretisation methods and schemes

ReFRESCO uses the finite volume (FV) method with a cell-centred, collocated arrangement, where the computational domain is subdivided into a finite number of cells. The FV method uses the integral form of Navier-Stokes equations to determine the flux going in and out of each cell in the domain, storing all information in the cell centre. The FV method can accommodate any type of grid, therefore it is suitable for complex geometries like ship hulls. More general information about the FV method can be found in, for example, Ferziger et al. [66].

The FV method involves volume and surface integration over each cell. As an example, three Cartesian cells (or control volumes) are considered, identified with W,P and E, as shown in Fig. 4.1. The volume and surface integrals over the cell P read:

$$\begin{aligned} \int_{\Omega_p} \phi d\Omega &\approx \phi_P \Delta\Omega \\ \oint_{S_f} \phi dS &\approx \phi_f S_f \end{aligned} \tag{4.1}$$

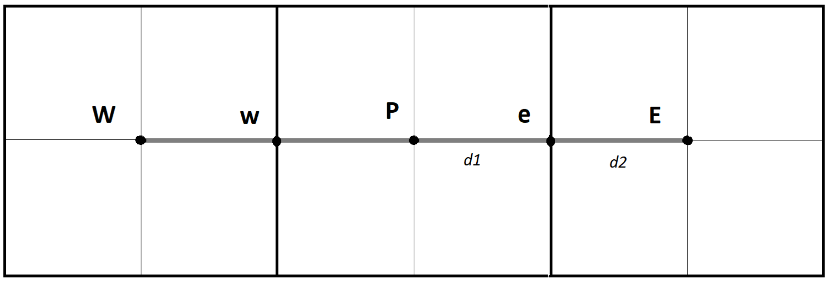

Figure 4.1: Example control volume.

ϕ_P is the value in the cell centre of P, $\Delta\Omega$ is the cell volume and ϕ_f and S_f are the value at the face F and the surface of the face respectively. The volume integral assumes that the value at the cell centre is the average over the whole volume. Likewise, the surface integral assumes that the value at the surface centre is the average of the whole surface.

For the volume integral, all information is available at the cell centre, making this integral easy to compute. The surface integral, however, needs the information at the faces around the cell, which is not directly available.

4.1.1. Approximation of the face values

To approximate the face values, there are multiple methods that can be used. Central difference is a widely used scheme, with second order accuracy:

$$\begin{aligned} \phi_e &= a\phi_E + (1-a)\phi_P \\ a &= \frac{|x_e - x_P|}{|x_E - x_P|} \end{aligned} \tag{4.2}$$

Unfortunately, this method is unbounded, which means it can lead to non-physical oscillations. A well-known bounded scheme is the upwind scheme. This scheme chooses a value based on the mass flow, $F = \rho S_e U_e \cdot n_f$:

$$\phi_e = \begin{cases} \phi_P & \text{if } F > 0 \\ \phi_E & \text{if } F < 0 \end{cases}$$

The disadvantage of this scheme is the first-order accuracy.

A scheme that is more accurate than the first-order upwind and is not as sensitive to non-physical oscillations is the Total Variation Diminishing (TVD) scheme. To explain the TVD scheme, first the κ-scheme is formulated:

$$\phi_e = \phi_P + \frac{|x_e - x_w|}{2}\left(\frac{1+\kappa}{2}\left(\frac{\partial\phi}{\partial x}\right)_e + \frac{1-\kappa}{2}\left(\frac{\partial\phi}{\partial x}\right)_w\right) = \phi_P + \frac{|x_e - x_w|}{2}\left(\frac{1+\kappa}{2}\left(\frac{\phi_E - \phi_P}{x_E - x_P}\right) + \frac{1-\kappa}{2}\left(\frac{\phi_P - \phi_W}{x_P - x_W}\right)\right) \tag{4.3}$$

When looking at this scheme, it shows that if κ equals 1, this scheme is equal to the central difference scheme without upwind. When κ equals -1, this scheme uses upwind and the scheme is equal to the so called linear-upwind interpolation (LUI) [78]. Linear schemes as the κ-scheme are still vulnerable to non-physical oscillations.

Godunov's theorem states that no linear scheme discretising partial differential equations with more than first-order accuracy can be monotonic. Therefore, it is interesting to look at non-linear schemes, which can be constructed using a flux limiter.

Flux limiters, as defined by Waterson and Deconinck [78], are "simple functions which define the convection scheme based on a ratio of local gradients in the solution field". An example is the following scheme:

$$\phi_e = \phi_P + \frac{|x_e - x_w|}{2} \Psi(r) \left(\frac{\partial \phi}{\partial x} \right)_w \tag{4.4}$$

$\Psi(r)$ is the limiter function and r is the ratio over the gradients of the face and the adjacent face,

$$r = \frac{\phi_E - \phi_P}{\phi_P - \phi_W} \tag{4.5}$$

For the TVD scheme, there is a limit on the behaviour of the flux limiter, as shown in Fig. 4.2 and defined by the following limit:

$$\Psi(r) = \begin{cases} \min(r, 1) & \text{if } r \geq 0 \\ 0 & \text{if } r \leq 0 \end{cases} \tag{4.6}$$

The convective flux of the momentum equations, turbulence equations and the volume-fraction equation† are discretised with Van Leer's harmonic TVD scheme, for which the flux limiter is defined as[66, 78, 79]:

$$\Psi(r) = \frac{|r| + r}{1 + r} \tag{4.7}$$

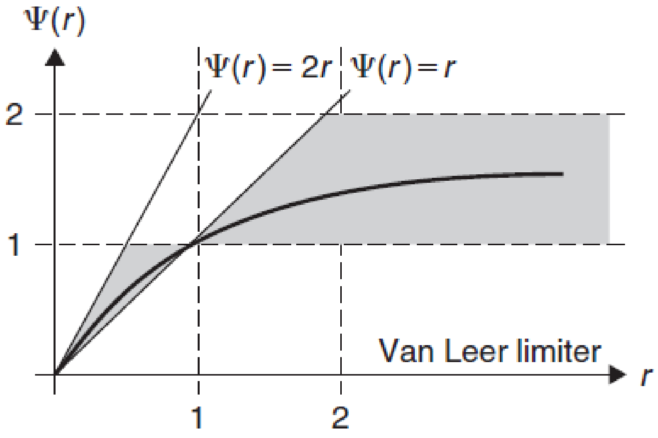

Figure 4.2: Flux limiter diagram with the limiting behaviour for the TVD schemes (grey area) and the "van Leer's " Harmonic scheme (continuous line) [79].

The diffusive flux of the volume-fraction and velocity equations have been discretised using the same scheme as for the convective flux. The other equations are discretised with geometric interpolation. For Cartesian grids, geometric interpolation scheme is defined as:

$$\begin{gathered} \phi_e = \alpha \phi_E + (1 - \alpha) \phi_P \\ \alpha = \frac{d1}{d1 + d2} \end{gathered} \tag{4.8}$$

---

† Lovato et al. [71] showed that ReFRESCO performs as intended for both single- and two-phase laminar flows of Herschel-Buckley fluids. They also showed that using a TVD discretisation scheme for the volume-fraction equation would improve the iterative convergence compared to using an interface-capturing scheme.

In this research, unstructured grids are used (see Section 4.4). Therefore, eccentricity corrections and non-orthogonality corrections are applied. More details about the general formulation for unstructured grids can be found in, for example, the book of Ferziger et al. [66].

4.1.2. Unsteady calculations

For unsteady calculations, the time derivative has to be discretised. This has been done with the implicit first-order backward Euler scheme. This results in:

$$\frac{\partial}{\partial t}\int_{\Omega}\rho\phi d\Omega \approx \frac{1}{\Delta t}[(\rho\phi_c\Delta\Omega)^n - (\rho\phi_c\Delta\Omega)^{n-1}] \tag{4.9}$$

n is the time level and Δt $[s]$ is the time step.

The implicit first-order backward Euler scheme has the benefit of being unconditionally stable [74]. Therefore, there is no need for restrictions in the Courant–Friedrichs–Lewy (CFL) number. A disadvantage of this scheme can be the first-order accuray. However, since the current research looks at a steady flow, higher-order time discretisation is not needed.

4.2. Solution methods

The solution methods used by ReFRESCO are described here. First, there are a number of non-linear terms which are linearised with Picard linearisation. Second, the Navier-Stokes equations are difficult to solve. Although the original problem has 4 equations and 4 unknowns (Pressure and three velocity components), there is no direct equation for pressure. To cover this problem, a "Semi-Implicit Method for Pressure-Linked Equations" (SIMPLE) -type method was used. Also, to prevent non-physical oscillations in the pressure, the Pressure-Weighted Interpolation (PWI) method was used.

4.2.1. Picard linearisation

To solve the equations, the non-linear terms have to be linearised. This is done by using the Picard linearisation approach. For the convection term, the mass flux is said to be known by previous iteration. The convection term in the momentum equation for the next iteration $i+1$ can thus be written as:

$$(\rho\mathbf{v}^2)^{i+1} = (\rho\mathbf{v})^i\mathbf{v}^{i+1} \tag{4.10}$$

4.2.2. The SIMPLE algorithm

The SIMPLE algorithm is a popular solution method proposed by Patankar and Spalding [80] to solve the Navier-Stokes equations. It is a pressure-correction method, which means it uses a pressure-correction equation to enforce mass conservation. The solving procedure can generally be described as:

1. Solve the linearised momentum equations for velocity using the pressure from the previous iteration.
2. Solve the pressure-correction equation and update the pressure field.
3. Use this pressure field to correct the velocity so the velocity field satisfies the continuity equation.
4. After this step, all other equations (for instance for the equations for volume-fraction and turbulence) will be solved sequentially.
5. If the corrections are small enough, the calculations will continue with the next time step. If not, these steps are repeated until the corrections are small enough.

As said, ReFRESCO uses a SIMPLE-type method, which is thus based on the method described above. For more information about the solution methods used in ReFRESCO, see Vaz et al. [73] or Klaij and Vuik [81].

4.3. Boundary conditions

In Section 2.5.3, two examples of RANS computations for a ship sailing through shallow muddy waters have been given. The boundary conditions used in this thesis are similar to those used in previous research. This paragraph describes the different boundary conditions used. For the domain and the conditions per boundary, see Chapter 5.

4.3.1. Wall

When the boundary condition is set to a wall, it mimics an impenetrable surface either at rest or moving at a given speed. The velocity component is therefore given at this boundary, which means a Dirichlet boundary condition is used for the velocity. Neumann boundary conditions are applied for other quantities, such as pressure and volume-fraction. However, this is different for the turbulence quantities. The turbulence quantities are set at zero, with the exception of ω, which is specified at the first node away from the wall.

Wall function are used in turbulence modelling when the number of cells required to accurately solve the viscous sublayer is excessively large. When the grid near the wall boundary is fine enough, these wall functions are not necessary. An explanation about these wall functions can be found in literature such as Wilcox [82] or Pope [67].

4.3.2. Symmetry and slip wall

For a slip wall, there is no flux through the boundary. The normal velocity components are set to zero, whereas the tangential velocity components are free to evolve. For perfectly flat surfaces, the symmetry boundary has the same treatment as the slip wall boundary in ReFRESCO.

4.3.3. Inflow and outflow

The inflow boundary condition uses a Dirichlet condition for all quantities except for the pressure for which there is a Neumann condition. The outflow condition has a Neumann condition for all quantities.

4.4. Grid

To solve the discretised problem, a computational grid is needed. This grid divides the domain into a finite number of control volumes, cells, for which the problem will be solved. For the current research, unstructured grids are used. More information about the different grids existing can for example be found in the books of Larsson and Raven [31], Ferziger et al. [66], Hirsch [79].

To create the unstructured grids, NUMECA's grid generator Hexpress (numeca.com) was used. Hexpress generates non-conformal body-fitted hexahedral unstructured methods with a 5 step approach. In these 5 steps, it will make a basic mesh, fit this onto the body and then iterate to get the best quality. Last, a local refinement for the boundary layer is added. For determination of the domain size as to the best refinement choices around the hull, see ITTC Quality system group [83].

To get a reliable estimation of the discretisation errors, a grid refinement study needs to be carried out. A grid refinement study is difficult to perform when using unstructured grids since it is difficult to get geometrical similar grids. Crepier [84] showed how to perform a grid refinement study with grids made in Hexpress. That study showed it is possible to get reliable error estimation with grids from Hexpress. However, the uncertainty highly depends on the turbulence model and will still give a higher uncertainty estimation than structured grids [84].

4.4.1. Grid quality

Grid refinement will almost always reduce the discretisation errors, however it could be more efficient to improve the grid quality. Grid quality can be improved by grid optimisation (which is also a step used in Hexpress). A number of criteria will be optimised, such as the orthogonality of the cells and the eccentricity.

Orthogonality is measured by the angle θ between the face normal n and the line connecting the cell centres, as shown in Fig. 4.3a. When this angle equals 0, the grid is seen as orthogonal. When this angle is far from 0, there could be large errors and iterative convergence problems [66]. Therefore, ReFRESCO uses non-orthogonality corrections.

Eccentricity is often measured by the distance between the face centre k and the point k' at which the line between the cell centres intersects with the face, as shown in Fig. 4.3b. The eccentricity can be reduced by for instance local refinement. ReFRESCO also uses eccentricity corrections in order to get more accurate approximations on the cell face.

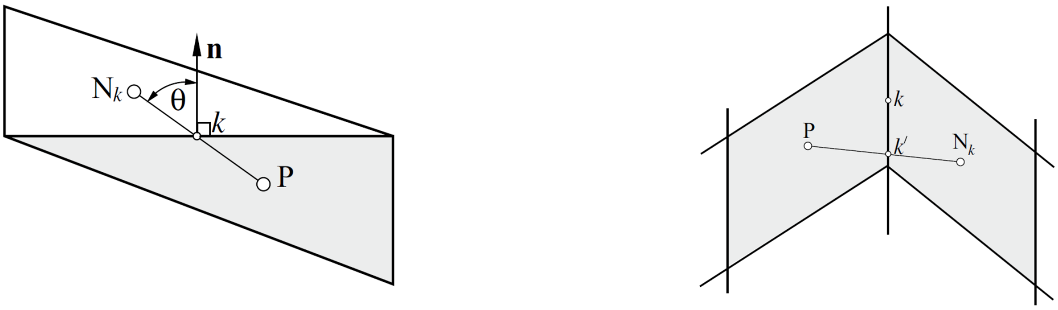

(a) Example of grid non-orthogonality

(b) Example of large eccentricity

Figure 4.3: Non-orthogonality and cell eccentricity [66].

More information about the effects of non-orthogonality and eccentricity on the results, as well as other measurements for grid qualities can be found in, for example, the book of Ferziger et al. [66].

5

Single-phase flow simulations

This chapter describes the single-phase flow simulations with uniform density, which focus on a ship sailing through only mud (see Fig. 5.1). The effects of a varying mud yield stress on the ship resistance has been analysed without the presence of any waves, free-surface waves or internal waves.

The first section describes the computational set-up. This section is followed by a discussion on the solution verification. The results are found in the last section.

Figure 5.1: Illustration of a ship sailing through only mud.

5.1. Computational set-up

The ship used for this research is the KVLCC2 at model scale with transom. The main particulars of the vessel can be found in Section 1.3. The appendages of the hull are not taken into account. The size of the domain is shown in Fig. 5.2a. The choices for the boundary conditions are shown in Fig. 5.2b.

Multiple grids have been generated with the grid generator HEXPRESS. A grid refinement study has been performed, in which four grids are used. The number of cells in these grids are shown in Table 5.1. Due to the use of unstructured grids, the number of faces on the hull $N_{s,i}$ is used to determine the grid refinement ratio r_i instead of the cell volume, as discussed by Rocha et al. [85]. The grid used for the final simulations is the second finest grid. Details about the grid generation can be found in Appendix B. Information about the influence of the position of the inlet on the ship resistance if found in Appendix C

Table 5.1: Grids used for the grid refinement study

Grid	number of cells in volume ($\times 10^{-6}$)	number of cells at hull $N_{s,i}$ ($\times 10^{-6}$)	$r_i = \sqrt{N_{s,1}/N_{s,i}}$
4	0.46	0.0085	3.866
3	3.33	0.032	1.981
2	**10.84**	**0.071**	**1.336**
1	24.92	0.127	1.000

The grids are used to solve a total of 6 equations: momentum equations, pressure correction equation and the two turbulence equations. The methods used to solve these equations are discussed in Chapter 4. The

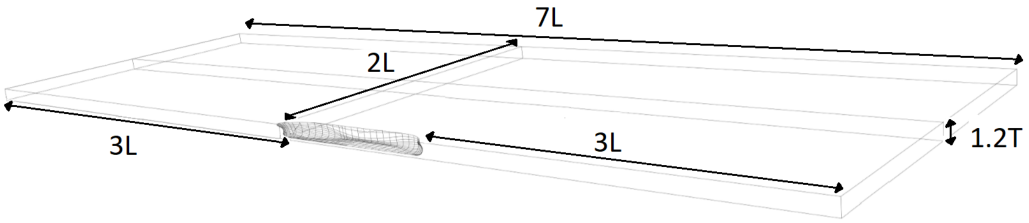

(a) Domain size

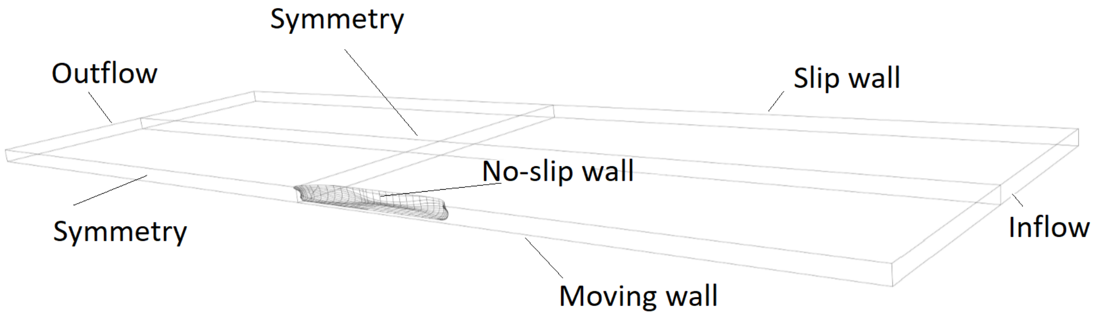

(b) Boundary conditions

Figure 5.2: Computational domain around the KVLCC2.

schemes used and the initialisation for the equations are shown in Table 5.2. simulations are performed for two different turbulence models: $k-\omega$ SST 2003 and the KSKL model, which are both described in Chapter 3. A wall-resolved grid is used around the hull to maintain accuracy. However, wall-functions are used to solve the flow close to the bottom, since the forces on the bottom are not of interest for this study.

Table 5.2: Main settings for the single-phase flow calculations

Equation:	Momentum	Pressure	Turbulence
Convection scheme	harmonic TVD	-	harmonic TVD
Initialisation	Inflow velocity	0	Turbulence intensity $I = 0.01$ (1%) , $\mu_T/K = 1$

Table 5.3: Non-dimensionalisation of quantities for the single-phase calculations

Quantity	Symbol	Formula	Notes
Force	F_i	$C_i = \frac{F_i}{\frac{1}{2}\rho S_{wa} V_\infty^2}$	
Pressure	p	$p^* = \frac{p}{0.5\rho V_\infty^2}$	
Velocity	u	$u_i^* = \frac{u_i}{V_\infty}$	
Yield stress of mud	τ_y	$\tau_y^* = \frac{\tau_y}{\tau_{y,max}}$	with $\tau_{y,max} = 1\ Pa$
Apparent viscosity of mud	μ_{app}	$\mu_{app}^* = \frac{\mu_{app}}{L_{pp} V_\infty}$	
Eddy viscosity	μ_T	$\mu_T^* = \frac{\mu_T}{L_{pp} V_\infty}$	

The non-dimensionalisation used for the different quantities is shown in Table 5.3.

Steady simulations are performed. The parameters used in the single-phase simulations are summarised in Table 5.4. Simulations are performed for $Fn = 0.064$, $Fn_h = 0.23$ and $Re = 4.452 \cdot 10^6$.

Table 5.4: Summary of the parameters used in the single-flow simulations

Description	-	unit
Density ρ	1200	$kg \cdot m^{-3}$
Consistency Parameter / molecular viscosity K	10^{-3}	$kg \cdot m^{-1} \cdot s^{-2+n}$
Flow index n	1	-
Regularisation parameter m	10	s
Yield stress τ_y	ranging from 0 to 1	Pa
Froude number Fn_h	0.23	-
Reynolds number Re	$4.452 \cdot 10^6$	-

5.2. Solution verification

Outside of the assumptions made in the modelling of the problem, numerical solutions are always affected by numerical errors. The numerical error consists of the following components:

- round-off error
  - Error due to the precision of the computer.
- iterative error
  - Error due to iterative methods to solve the discretised equations.
- discretisation error
  - Error due to the transformation of a system of partial differential equations into a system of algebraic equations.

It is possible to get an estimate of these numerical error by performing solution verification. More information about solution verification can be found in the standard of The Americam Society of Mechanical Engineers (ASME) [86].

For the current study, the iterative convergence is discussed to get an indication of the influence of the iterative errors. The uncertainty of the results due to spatial discretisation is determined with the help of a grid refinement study. The round-of error can be neglected because of the use of double precision.

5.2.1. Iterative convergence

Simulations are run until the L2-norm of the normalised residuals have dropped below a certain convergence tolerance or when a maximum number of iterations is reached. The influence of this convergence tolerance on the forces is shown in table 5.5. The difference between convergence tolerance of 10^{-6} and 10^{-7} is less than 0.2%. Therefore, the convergence tolerance is set at 10^{-6}.

Table 5.5: Influence of the outer loop convergence tolerance using the SST model

convergence tolerance	$C_T \cdot 1000$
10^{-4}	4.891
10^{-5}	4.719
10^{-6}	5.094
10^{-7}	5.101

The iterative convergence of a Newtonian flow are shown in Fig. 5.3 and Fig. 5.4. For Newtonian flow, the residuals of all quantities dropped below the convergence tolerance. For simulations with a non-Newtonian fluid and the SST turbulence model, the L2-norm of the residuals of ω stagnates at 10^{-1}, as shown in Fig. 5.5. Therefore, there is a possibility that the results are influenced by iterative errors.

The position in the domain of the highest residuals for ω are illustrated in Fig. 5.6. The highest residuals are found at the aft of the vessel. It is difficult to get a good grid quality at the stern due to the complex shape. This could be one of the reason for the poor iterative convergence. Another reason can be the presence of the transom. Around the transom, there is flow separation and reversed flow, leading to high residuals. A third reason may be the use of non-Newtonian fluids with a turbulence model that was developed for Newtonian fluids. This deserves further investigation.

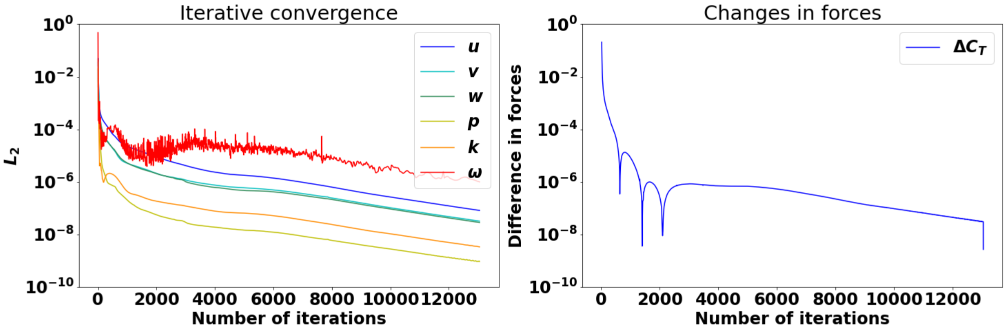

Figure 5.3: Iterative convergence using the SST model and Newtonian fluid.

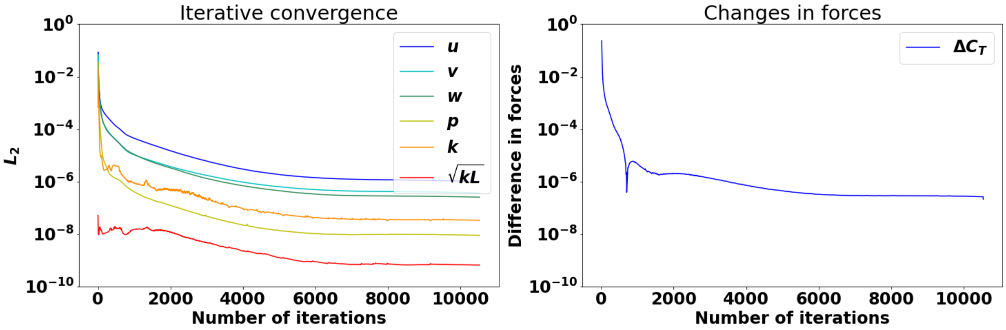

Figure 5.4: Iterative convergence using the KSKL model and Newtonian fluid.

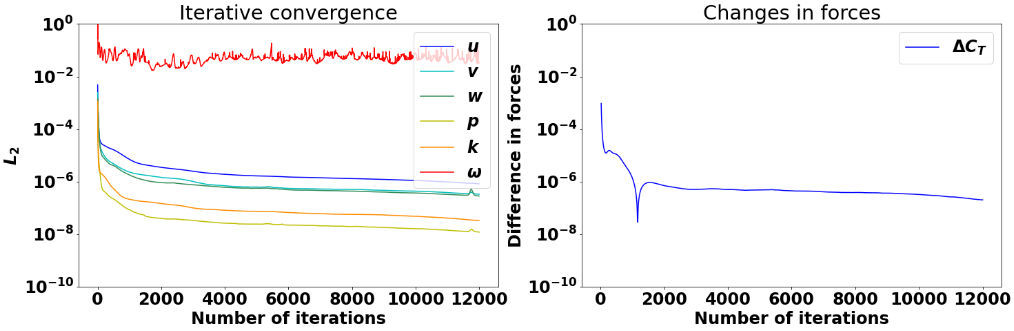

Figure 5.5: Iterative convergence using the SST model and non-Newtonian fluid ($\tau_y^* = 0.2$).

Figure 5.6: Residuals for ω that are larger than 0.1 (red) are at the aft of the vessel.

5.2.2. Discretisation uncertainty

The four grids shown in Table 5.1 are used to determine the uncertainty of the results due to the discretisation. The procedure proposed by Eça and Hoekstra [87] is used to estimate this uncertainty. In Table 5.6, the discretisation uncertainties for the second finest grid are shown for different combinations of turbulence models and different rheological models.

The uncertainties are significant for the pressure coefficient when using the SST turbulence model for the Newtonian fluid. This higher uncertainty for the pressure is also visible in the results of Crepier [84], who performed similar simulations for deep water conditions without transom.

Table 5.6: Uncertainty for second finest grid

	$C_P \cdot 10^3\,[-]$	U_{C_P}	$C_F \cdot 10^3\,[-]$	U_{C_F}	$C_T \cdot 10^3\,[-]$	U_{C_T}
$\tau_y^* = 0$						
SST	2.113	35.78%	4.201	1.80%	6.314	11.86%
KSKL	1.969	17.61%	4.114	3.67%	6.082	3.08%
$\tau_y^* = 0.2$						
SST	4.528	3.91%	4.404	1.09%	8.932	1.84%
KSKL	3.699	31.24%	3.066	2.43%	6.765	18.45%

The pressure force consists out of two large opposite forces on the bow and the aft of the ship. Both forces are affected by discretisation error, which becomes more visible when the two forces are summed together into a value which is much smaller in magnitude than both forces separately. Therefore, this error will influence the total pressure coefficient more than expected. This also explains why this uncertainty is not as large when using a yield stress. The yield stress seems to increase the pressure forces, making the discretisation error less influential to the total result. This is also shown in Appendix D.

5.3. Results

A fluid with yield stress gives different flow patterns than a Newtonian fluid. In regions with zero shear rate, the fluid with a yield stress has a very high viscosity and it behaves as a solid material. As the fluid meets the ship, the shear rate is no longer zero and the viscosity decreases. Therefore, the fluid near the ship behaves more like a liquid. Fig. 5.7 illustrates that this low-viscosity region becomes smaller as the yield stress increases. In addition, the low-viscosity in the wake shifts away from the symmetry plane. This shift in the wake is also visible in simulations of a sphere moving through a Bingham fluid in laminar regime [88].

The high viscosity in the far-field is dependent on the modelling of the mud. As described in Section 3.2, the mud is modelled with the Herschel-Bulkley model. The model is regularised, thus the regularisation parameter can influence the results. More information about the influence of this regularisation parameter is found in Appendix E.

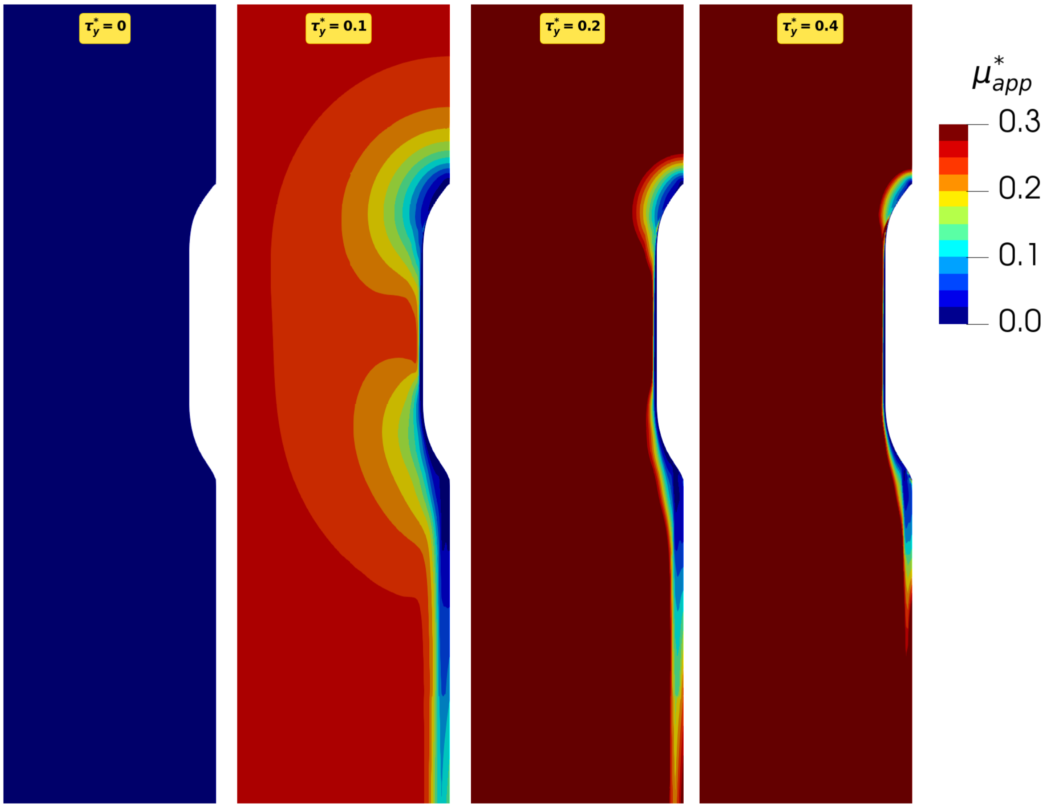

Figure 5.7: Top view of the apparent viscosity μ_{app}^* at half of the draft of the ship using the SST turbulence model.

The varying viscosity over the domain changes both the pressure forces and the frictional forces, as both forces have a viscous origin. These alterations in the flow field affect the resistance on the vessel. The total ship resistance for this case can be decomposed in a *viscous pressure resistance* and a *frictional resistance*, as previously described in Section 2.1.

The total resistance and the different components varying for different mud yield stress are presented in Fig. 5.8. The total force overall increases as the yield stress increases. While for Newtonian fluids the *frictional resistance* is the dominant component of the total resistance, the pressure component becomes more dominant as the yield stress increases.

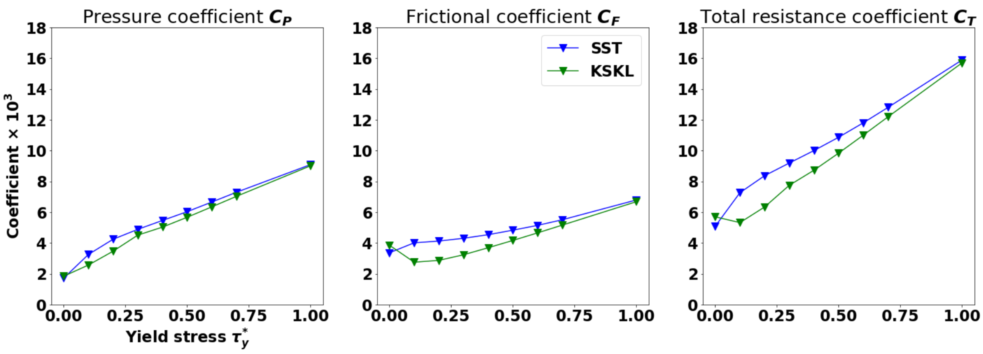

Figure 5.8: Ship's resistance versus normalised yield stress using the SST and KSKL turbulence models.

The viscous pressure is the force due to the difference between the pressure at the bow and the pressure at the aft and is dependent on the changing viscosity. As the mud yield stress increases, the pressure at the aft decreases. Therefore, the total *pressure resistance* increases overall. The increase in viscous pressure as yield stress increases is also shown in the literature, for example on a sphere moving through a Bingham fluid in laminar regime [88].

Although the different turbulence models do not agree perfectly for the *viscous pressure resistance*, they do agree on the overall trend. This is not the case for the *frictional resistance*. For the KSKL, the *frictional resistance* first appears to decrease and then to increase with the yield stress, whereas for the SST model the *frictional resistance* increases.

The different predictions for the two turbulence models is also observed in the eddy viscosity, which is illustrated Fig. 5.9. For the KSKL, the eddy viscosity decreases significantly for Bingham fluids, whereas for the SST model the eddy viscosity first increases and then starts to decrease. The SST model therefore predicts a higher level of turbulence behind the vessel when the yield stress increases. Further increase in yield stress does seem to damp out the turbulence, as expected.

Besides the changes in turbulence model, it is also not clear whether the flow is fully turbulent. The increasing yield stress causes the apparent viscosity to vary over the domain, which makes it difficult to say whether a flow is turbulent or laminar. For current calculations, turbulence is assumed. This assumption may be incorrect for cases with high yield stress.

Summarising, the KSKL and the SST models produce results that are significantly different when changing the yield stress. However, which model is more accurate is unclear.

5.4. Conclusions

The resistance of a ship sailing in a homogeneous mud layer has been computed at different mud yield stress. These computations were performed to see the influence of the discretisation of the domain on the forces and the influence of mud yield stress on the ship resistance.

Solution verification is performed to see whether the simulation is sufficiently accurate for the given objective. The iterative convergence is acceptable for Newtonian fluids. For non-Newtonian fluids, ω does not converge well. The reason for this is unknown. The discretisation error seems acceptable for the *frictional resistance* but not for the *pressure resistance*. The result using the SST model has a high uncertainty, 35%, for the *pressure resistance*. However, other studies using an unstructured grid made with Hexpress show similar results [84]. Furthermore, this uncertainty decreases as the fluid yield stress increases.

Both iterative convergence and grid refinement studies show an influence of the numerical errors on the results. For the current objective, however, this influence is not necessarily a problem. The trend of the results could still be determined. Regardless, the issues that emerged in the solution verification are instructive to improve the approach for future studies.

The total resistance increases as the yield stress increases. The *viscous pressure resistance* increases significantly when the yield stress increases. For high yield stress, the *viscous pressure resistance* even becomes the most dominant contribution in the total force. The influence of the yield stress on the *frictional resistance* is unclear as the *frictional resistance* appears to be highly dependent on the choice of turbulence model.

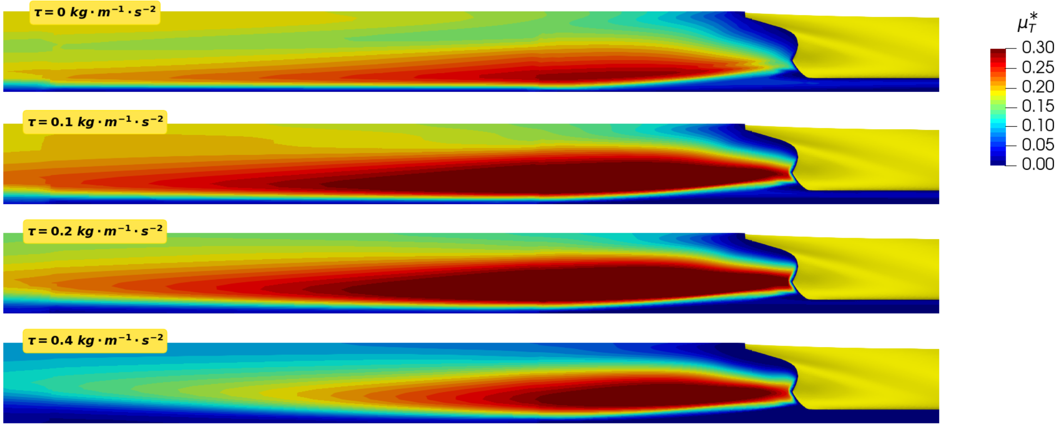

(a) SST

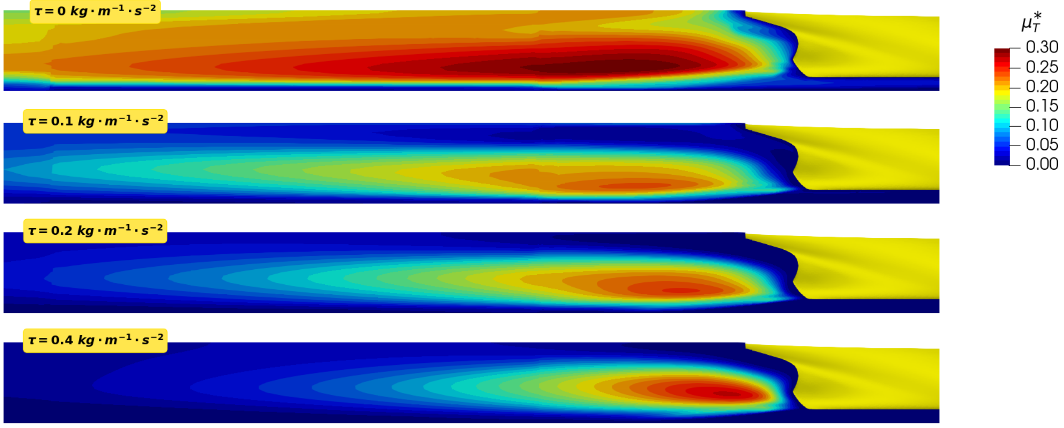

(b) KSKL

Figure 5.9: Eddy viscosity at the aft ship for different values of yield stress.

6

Two-phase flow simulations

This chapter describes a ship sailing through shallow water with a fluid mud layer on the seabed. While the results in Chapter 5 gave an indication of the effect of the yield stress for an object sailing through a single fluid, this chapter will investigate the combined effect of mud yield stress, mud density and mud layer thickness. Due to the addition of the interface, the effect on the wave-making resistance has been taken into account.

This chapter is divided into four sections. First, the computational set-up of the simulations is discussed. Second, the solution verification is discussed. The third section shows the influence of the domain width on the forces. The results are found in the last section.

6.1. Set-up

The two-phase simulations used the same grid as for the single-phase simulations, but with additional refinement around the water-mud interface. The grid around the ship is shown in figure 6.1. More information about the grid generation can be found in Appendix B.

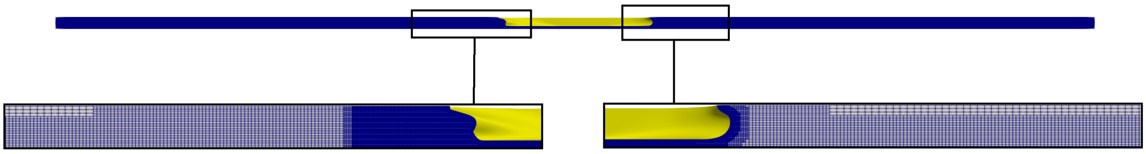

Figure 6.1: Final grid used in the two-phase simulations.

The grid with additional refinement has 15.5 million cells. To check the influence of the position of the side boundary, one additional grid is made with a width of 6 times the ship length using a total of 25.7 million cells.

Compared to the single-phase simulations, the two-phase simulations need to solve an additional equation for the water-mud interface. The schemes used and the initialisation to solve the 7 equations are shown in Table 6.1. The turbulence model used in these simulations is the SST model, which is often used in ship hydrodynamics [31].

Chapter 5 discussed a possible lack of accuracy of the SST model when simulating non-Newtonian fluids. This lack of accuracy is expected to be less significant for the two-phase simulations. First, the largest part of the domain is filled with water, for which the SST model can be used quite accurately. Second, the *dead-water resistance* will make the pressure coefficient even more dominant. Since the influence of the turbulence model was mainly visible in the *frictional resistance*, the influence of the turbulence model is expected to be less visible in the total results.

Table 6.1: Main settings for the two-phase flow calculations

Equation:	Momentum	Pressure	Turbulence	Free surface
Convection scheme	harmonic TVD	-	harmonic TVD	harmonic TVD
Initialisation	Inflow velocity	0	Turbulence intensity $I = 0.01$ (1%), $\mu_T/K = 1$	initial mud level depends on the mud layer thickness

The flow field is expected to be steady. However, to improve the convergence, unsteady simulations are performed. Each simulation ran for 150 timesteps with a timestep size of $\Delta t * V/L = 0.06$, except for the simulations with a non-Newtonian mud layer. These simulations started from the solutions with the Newtonian mud layer and ran for 100 timesteps. The resistance is the average of the last 30 timesteps, unless defined differently, due to the fluctuations in the results. The influence of the time discretisation is discussed in Section 6.2.2. The non-dimensionalisation used for the different quantities is shown in Table 6.2.

Table 6.2: Non-dimensionalisation of quantities for the two-phase calculations

Quantity	Symbol	Formula	Notes
Force	F_i	$C_i = \frac{F_i}{\frac{1}{2}\rho S_{wa} V_\infty^2}$	
Pressure	p	$p^* = \frac{p}{0.5\rho_1 V_\infty^2}$	
Density of mud	ρ_2	$\alpha = \frac{\rho_1}{\rho_2}$	
Velocity	u	$u_i^* = \frac{u_i}{V_\infty}$	
Yield stress of mud	τ_y	$\tau_y^* = \frac{\tau_y}{\tau_{max}}$	with $\tau_{y,max} = 1\ kg \cdot m^{-1} \cdot s^{-2}$
Apparent viscosity of mud	μ_{app}	$\mu_{app}^* = \frac{\mu_{app}}{L_{pp} V_\infty}$	
Eddy viscosity	μ_T	$\mu_T^* = \frac{\mu_T}{L_{pp} V_\infty}$	
Wave elevation	ζ	$\zeta^* = \frac{\zeta}{h_2}$	

Table 6.3: Summary of the parameters used in the two-phase simulations

Description	-	unit
Density of the water ρ_1	1000	$kg \cdot m^{-3}$
Molecular viscosity of the water μ_1	10^{-3}	$kg \cdot m^{-1} \cdot s^{-1}$
Density of the fluid mud ρ_2	ranging from 1050-1250	$kg \cdot m^{-3}$
Consistency Parameter / molecular viscosity of mud K	10^{-3}	$kg \cdot m^{-1} \cdot s^{-2+n}$
Flow index n	1	-
Regularisation parameter m	40	s
Yield stress of the mud τ_0	ranging from 0 to 0.6	Pa
Mud layer thickness h_2	ranging from 0 to 0.3	$[\times T]$ m

The parameters used for the two-phase simulations are summarised in Table 6.3. It must be noted that the UKC and mud layer thickness are dependent on each other for these simulations since the depth is fixed. Therefore, the influence due to UKC can also be due to the mud layer thickness and vice-versa. The different cases simulated are shown in Fig. 6.2. Simulations are performed for $Re = 3.71 \cdot 10^6$ [†], $Fn = 0.064$ and $Fn_h = 0.23$.

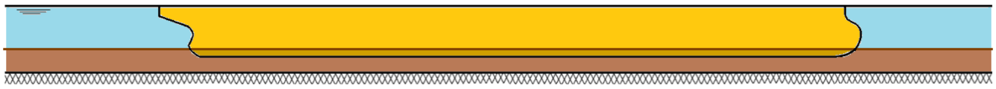

(a) UKC of -10% or mud layer thickness of $\frac{h_2}{T} = 0.3$

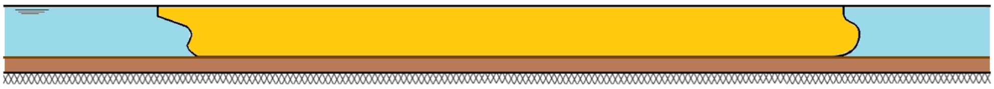

(b) UKC of 0% or mud layer thickness of $\frac{h_2}{T} = 0.2$

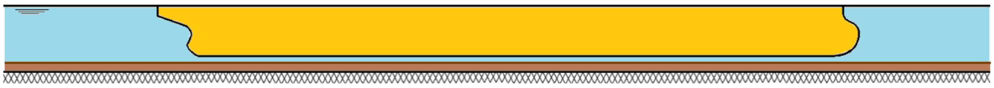

(c) UKC of 10% or mud layer thickness of $\frac{h_2}{T} = 0.1$

Figure 6.2: Different combination of UKC and mud layer thickness h_2.

6.2. Solution verification

In Chapter 5, the discretisation uncertainty of the grid without the additional refinement at the interface was estimated. Since the same grid is used, another grid refinement study is not performed. Uncertainties are expected to increase due to the addition of another equation for the interface. However, the grid is also more refined at the fluid interface, which should reduce the discretisation uncertainties. Hence, the discretisation uncertainty is expected to be approximately the same as in Chapter 5.

Although the solution is expected to be steady, the problem is modelled unsteady. Therefore, the discretisation error also has a contribution from time discretisation. The influence of the time discretisation is checked with a time refinement study. In addition, the iterative convergence is checked again. The iterative convergence can be different compared to the single-phase simulations due to the additional equation for the water-mud interface.

6.2.1. Iterative errors

Simulations are run until the L2-norm of the normalised residuals have dropped below 1×10^{-6} or when the maximum number of iterations has been reached. The convergence for the two-phase simulations is significantly worse than for the single-phase simulations. The L2-norm residuals never dropped below the limit set for the simulations as shown in Fig. 6.3.

The high residuals are mainly close to the hull. For example, the residuals for the volume fraction are high where the mud layer is close to the hull, as shown in Fig. 6.4. Unfortunately, the reasons for such poor iterative convergence are not clear.

The iterative convergence for ω becomes worse as the yield stress increases, as shown in Fig. 6.5. This was also visible in the iterative convergence of the single-phase simulations (see Section 5.2).

[†] This Reynolds number is defined with the density of water ρ_1

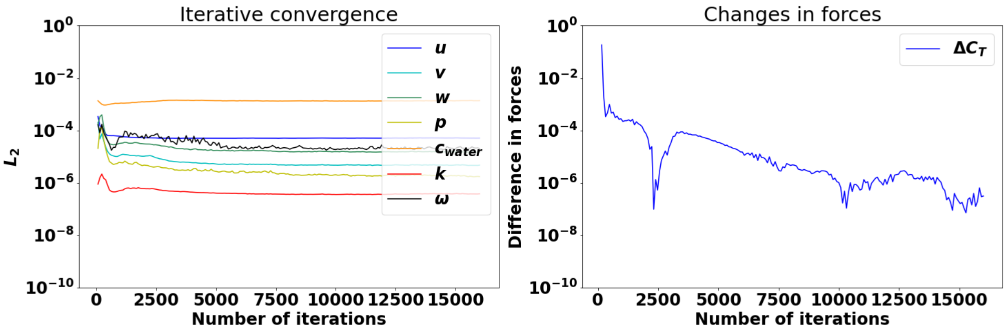

Figure 6.3: Iterative convergence, having a mud layer thickness of $\frac{h_2}{T} = 0.3$, a density ratio of $\alpha = 1.2$ and no yield stress.

Figure 6.4: Residuals for water volume fraction c that are larger than 0.01 (red) with a thick Newtonian mud layer.

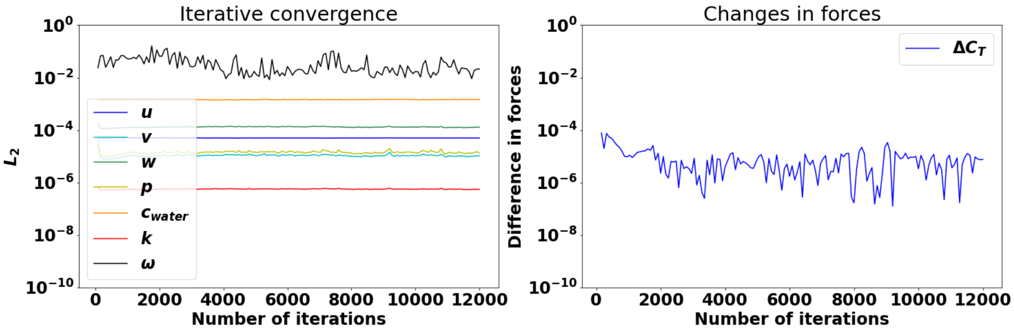

Figure 6.5: Iterative convergence, having a mud layer thickness of $\frac{h_2}{T} = 0.3$, a density ratio of $\alpha = 1.2$ and a yield stress of $\tau_y^* = 0.2$.

6.2.2. Time step size

The average forces and standard deviation σ using different timesteps are found in Table 6.4. The difference between the results is less than 0.3%, which suggest that the influence of the time discretisation on the resistance seems negligible. Furthermore, due to the use of an implicit scheme to solve the time discretisation, the stability of the simulations is less dependent on the size of the timestep. The timestep used in further simulations is $\Delta t * V/L = 0.06$.

Table 6.4: Average forces over the last 30 seconds using different time step size

stepsize $\Delta t * V/L$	$C_{P,avr}$	$\sigma\ C_P$	$C_{F,avr}$	$\sigma\ C_F$	$C_{T,avr}$	$\sigma\ C_T$
0.015	13.08	0.015%	4.37	0.003%	17.45	0.011%
0.030	13.09	0.028%	4.37	0.014%	17.47	0.024%
0.060	13.11	0.076%	4.37	0.031%	17.49	0.065%

6.3. Position of the side boundary

The calculation have been performed in the supercritical regime for the mud layer. Therefore, it is expected that the wave pattern will have large halve-wedge angles. With a small sized domain, this could cause reflection on the side domain and therefore disturbances in the flow field. In addition, a smaller domain can influence the forces on the ship due to a blockage effect which increases the flow velocity around the ship. The position of the side boundary is thus varied to see the effects on the wave pattern and forces.

Fig. 6.6 presents the wave patterns for the two different domains used. For the smaller domain, there is a reflective wave visible at the side boundary. The domain size also seems to affect the *total resistance*, as shown in Table 6.5. The *total resistance* is 4% higher for the smaller domain compared to results in the broader domain. Therefore, it is advised to have a broader domain for further studies. Due to the limited computational effort, the current study used the smaller domain.

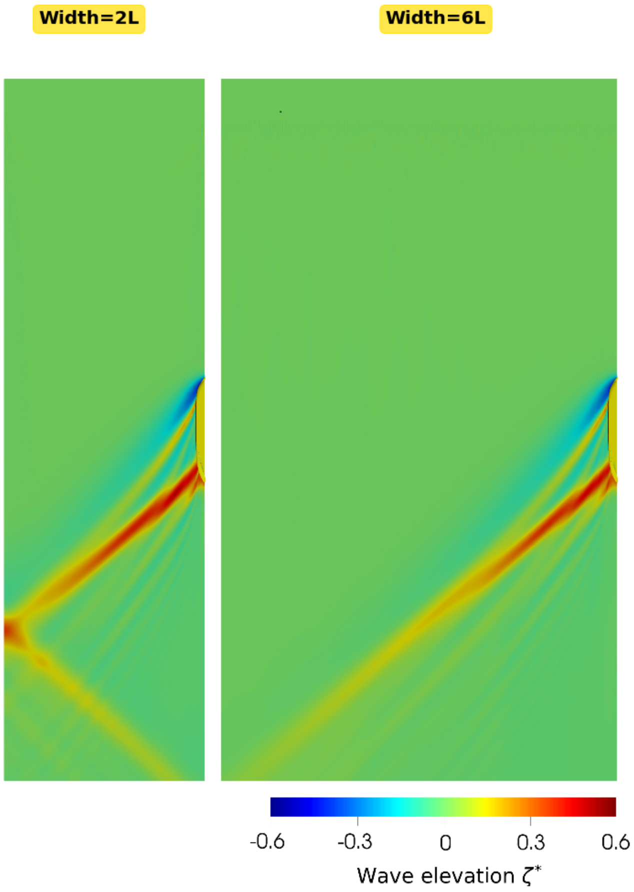

Figure 6.6: Influence of the domain size on the wave pattern. The mud layer is Newtonian, with a thickness of $\frac{h_2}{T} = 0.3$ and a density ratio of $\alpha = 1.2$.

Table 6.5: Difference in results due to domain width

	$2 \times L$	$6 \times L$	difference
$C_P \cdot 1000$	13.64	13.00	4.67%
$C_F \cdot 1000$	4.44	4.35	2.11%
$C_T \cdot 1000$	18.08	17.35	4.04%

6.4. Results and discussion

The simulations of a ship sailing over a mud layer are first performed with a Newtonian mud layer. After these simulations, the yield stress is increased to see the effect of that mud characteristic. The regularisation parameter is taken higher for the two-phase simulations compared to the single-phase simulations. The influence of the regularisation parameter is described in Appendix E.

The influence of mud viscosity and velocity on the wave pattern and resistance are not discussed in this chapter. The findings of changing the velocity can be found in Appendix F. More about the influence of the mud viscosity on the internal wave pattern and resistance can be found in Appendix G.

6.4.1. Newtonian mud layer

The resistance of the ship can again be divided into a *frictional* and *pressure resistance*. Due to the presence of the water-mud interface, the *pressure resistance* now consists out of the *viscous pressure resistance* and the internal wave-making resistance, which is also referred to as the *dead-water resistance*. As mentioned in Chapter 2, this means the forces are dependent on the Froude number for the internal wave. This internal Froude number is defined by Miloh et al. [1] as,

$$Fn_i = \frac{V}{\sqrt{g(1-\frac{1}{\alpha})\frac{h_1 h_2}{h_2/\alpha + h_1}}} \tag{6.1}$$

V is the ship velocity, $\alpha = \frac{\rho_2}{\rho_1}$ is the density ratio and h_1 and h_2 are the thickness of the water layer and the mud layer, respectively.
The internal Froude number Fn_i for the different cases computed are shown in Table 6.6. The vessel always sails in the supercritical regime for the mud layer $Fn_i > 1$. As discussed in Chapter 2, the supercritical regime is where the ship is sailing at a higher velocity than the critical wave velocity of the mud layer. Therefore, the wave pattern is expected to only show divergent waves. The angle of the wave should decrease as the flow becomes more supercritical, which happens as the internal Froude number increases.

Table 6.6: Internal froude numbers Fn_i for the different cases calculated.

Mud layer thickness h_2/T	Density α	Internal froude number Fn_i
0.3	1.20	1.27
0.3	1.15	1.44
0.3	1.10	1.73
0.3	1.05	2.41
0.2	1.20	1.48
0.2	1.15	1.68
0.2	1.10	2.02
0.2	1.05	2.80
0.1	1.20	2.02
0.1	1.15	2.28
0.1	1.10	2.74
0.1	1.05	3.79

The internal Froude Fn_i number depends on both the height and density of the two fluid layers. The Froude number increases as the mud layer thickness decreases and/or when the density ratio α decreases. Therefore, the half-wedge angle should be smaller when the mud layer thickness and/or density ratio decreases. Fig. 6.7 and Fig. 6.8 show that this is indeed the case.

The propagation velocity of the wave can be defined as $c = V \sin\psi$ [34], in which ψ is the half-wedge angle [°]. Since for the current research the ship is sailing in supercritical regime, the propagation velocity is limited. Assuming the wave is propagating at this limited velocity, the the half-wedge angle of the internal wave equals $\psi_2 = sin^{-1}(1/Fn_i)$. This relation is plotted against the internal Froude number Fn_i in Fig. 6.9

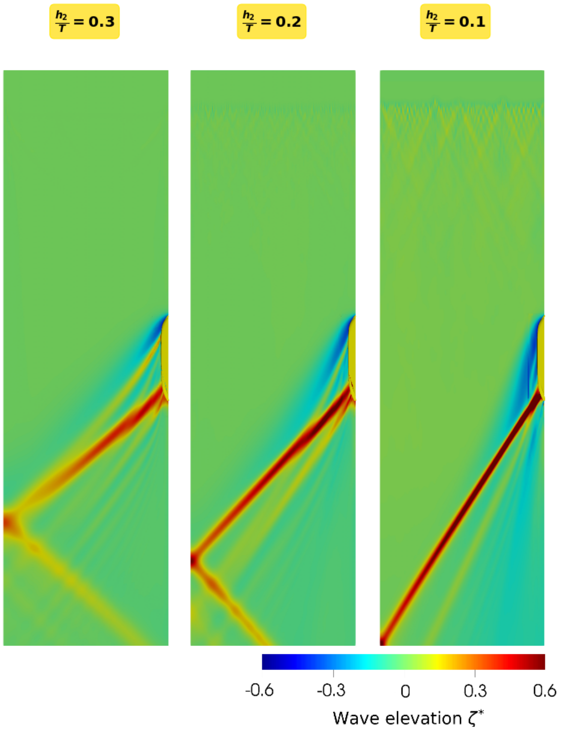

Figure 6.7: Internal wave patterns for Newtonian mud with a density of $\alpha = 1.2$ for different mud layer thickness.

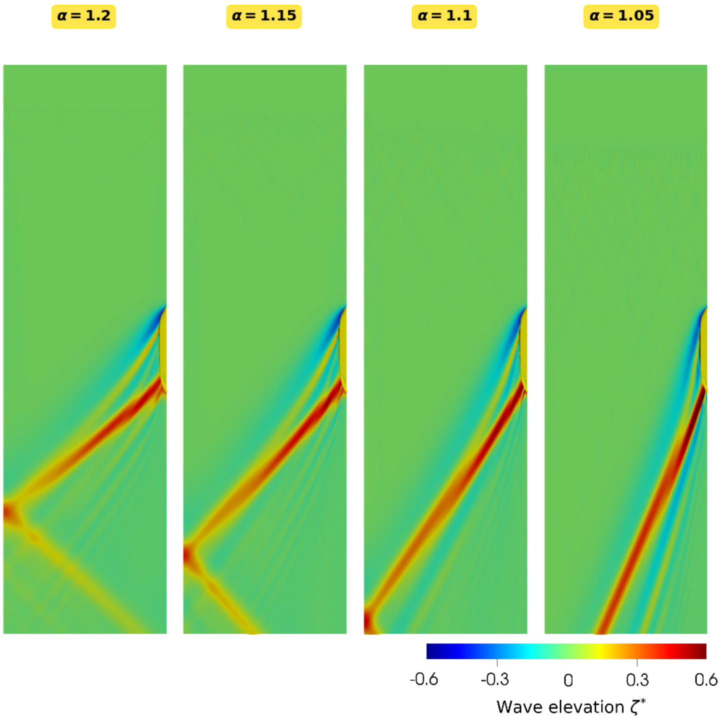

Figure 6.8: Internal wave patterns for Newtonian mud with different density with a mud layer thickness of $\frac{h_2}{T} = 0.3$.

and shows to be in very good agreement with the the present results. Only the half-wedge angle for the thin mud layer seems to differ. A possible explanation for this is that the grid is too coarse to capture this wave since the wave height for the thin mud layer is much lower.

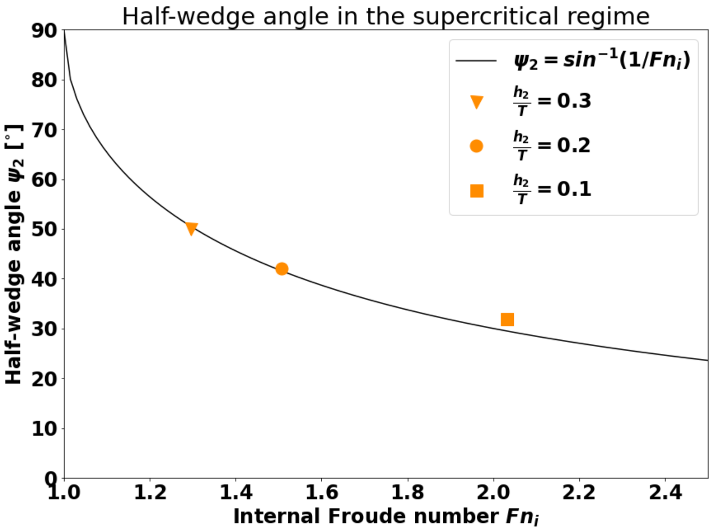

(a) Varying mud layer thickness ($\alpha = 1.2$)

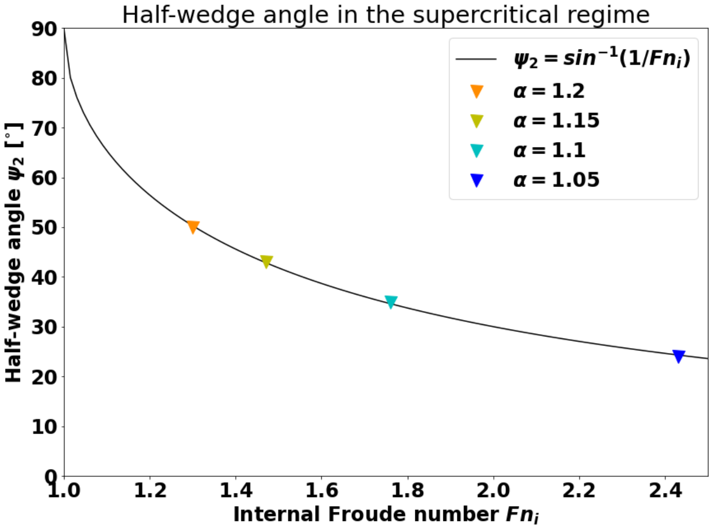

(b) Varying density ($\frac{h_2}{T} = 0.3$)

Figure 6.9: Half-wedge angle for different internal Froude numbers Fn_i.

The effect of the internal Froude number is also visible in the *pressure resistance*. The *dead-water resistance* occurs due to the formation of the internal wave. The maximum value of the *dead-water resistance* should occur at an internal Froude number Fn_i of around 1 [†] Fig. 6.10 shows the resistance for the different cases plotted against the internal Froude number.

[†] There is literature suggesting that this peak occurs for lower Froude numbers, $Fn_i = 0.7 - 1$ [1, 28, 63].

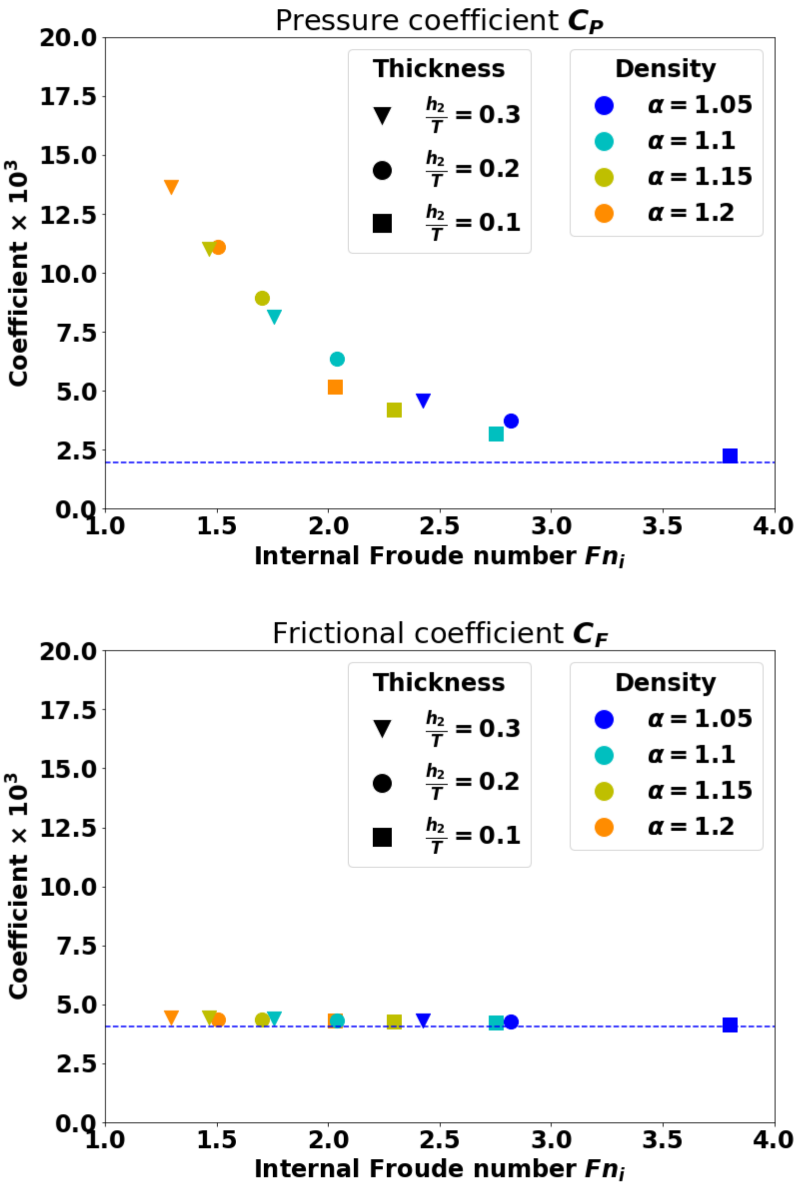

Figure 6.10: Ship resistance against the internal Froude number. The dashed line presents the ship resistance when sailing through only water.

The *pressure resistance* seems to increase as the internal Froude number approaches $Fn_i \approx 1$. Although it is not possible to separate the *viscous pressure resistance* and the *dead-water resistance*, this increase in pressure is most likely due to the *dead-water resistance*. At Froude numbers of $Fn_i > 2.5$, the *pressure resistance* tends to the *pressure resistance* of a ship sailing through only water. This suggest that the *dead-water resistance* vanishes and the *pressure resistance* is mostly the *viscous pressure resistance*.

The increase in the *pressure resistance* close to $Fn_i \approx 1$ is more than 4 times the *full water pressure resis-*

tance. This significant increase in *pressure resistance* can be explained by the increase in *dead-water resistance*. This large increase is also visible in different potential flow simulations.

Zilman and Miloh [20] performed a study for a different vessel sailing through shallow water with a fluid mud layer, also with potential flow. The vessel used in that research is similar to the vessel used in this study. They showed that the *dead-water resistance* reached $C_w = 12 \cdot 10^{-3}$ for a mud layer of $\frac{h_2}{T} \approx 0.2$.

Sano and Kunitake [22] determined the *total wave-making resistance*, thus the wave-making resistance from both interfaces, for the KVLCC2 in two-layer fluid using the Rankine source panel method. The *total wave-making resistance* reached up to $C_w = 10 \cdot 10^{-3}$, as shown in Fig. 6.11. These results also showed that the *total wave-making resistance* increases as the depth decreases.

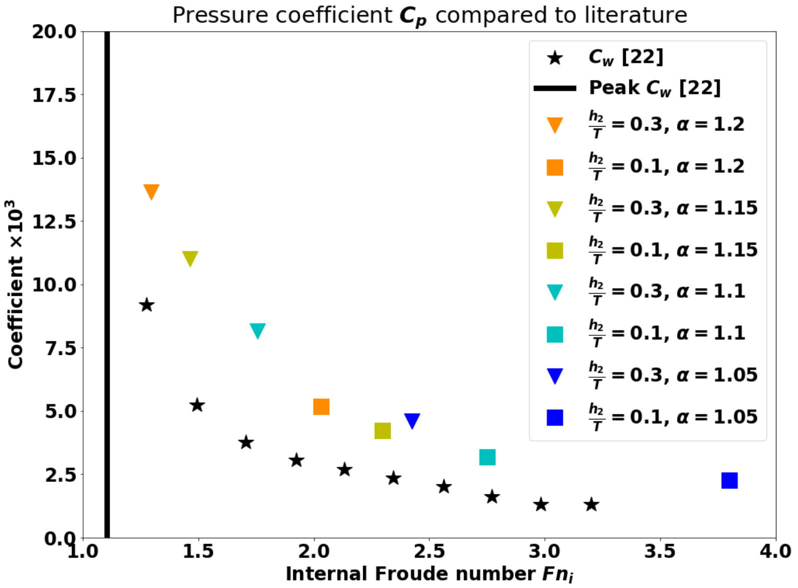

Figure 6.11: *Pressure resistance* coefficient against the internal Froude number compared to the *total wave-making resistance* coefficient determined by potential flow theory of Sano and Kunitake [22].

The result of Sano and Kunitake [22] do differ from results of this research due to a number of reasons. First, the domain they used is deeper. Second, the results in this research take into account the viscous pressure also. Third, Sano and Kunitake [22] takes into account the coupling with the air-water surface. Their results suggest that this coupling should also affect the internal Froude number and thus the position of the peak of the *dead-water resistance*. For future studies, it is advised to model the air-water interface when sailing in the critical regime $Fn_i \approx 1$ in order to get an indication on how big this influence is.

6.4.2. Influence of mud yield stress

The mud yield stress is varied to see the visco-plastic effect on the internal wave pattern and ship resistance. Fig. 6.12 shows the internal wave patterns for mud with different yield stress. In the far field the wave height seems to decrease. This is probably due to the higher viscosity in the far field of the domain.

In addition to decreasing wave height, Fig. 6.12 shows a growing depression in the wave behind the hull along the symmetry plane as the yield stress increases. As the fluid mud deforms, the yield stress causes the deformation to hold longer, which, in this case, causes a depression behind the vessel. Since the depression is still present at the outflow, it is possible that the position of the outflow boundary condition of the computational domain is also influencing this depression and thus the flow field around the vessel. This deserves further investigation.

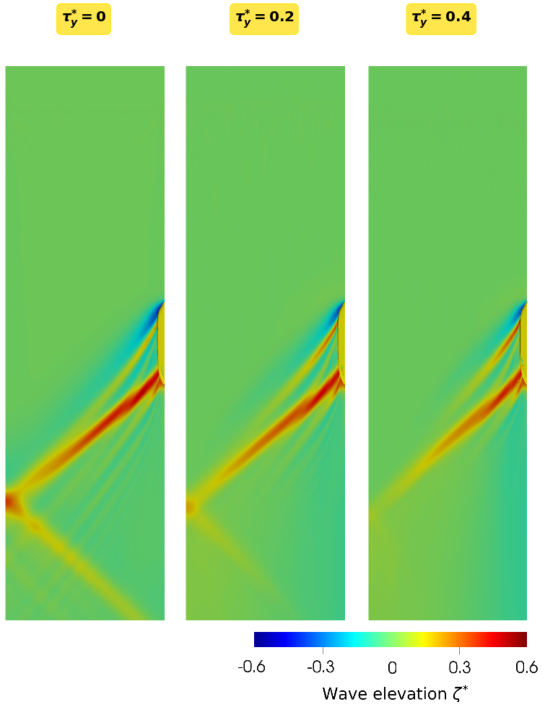

Figure 6.12: Influence of mud yield stress on the internal wave pattern ($\frac{h_2}{T} = 0.3$ and $\alpha = 1.2$).

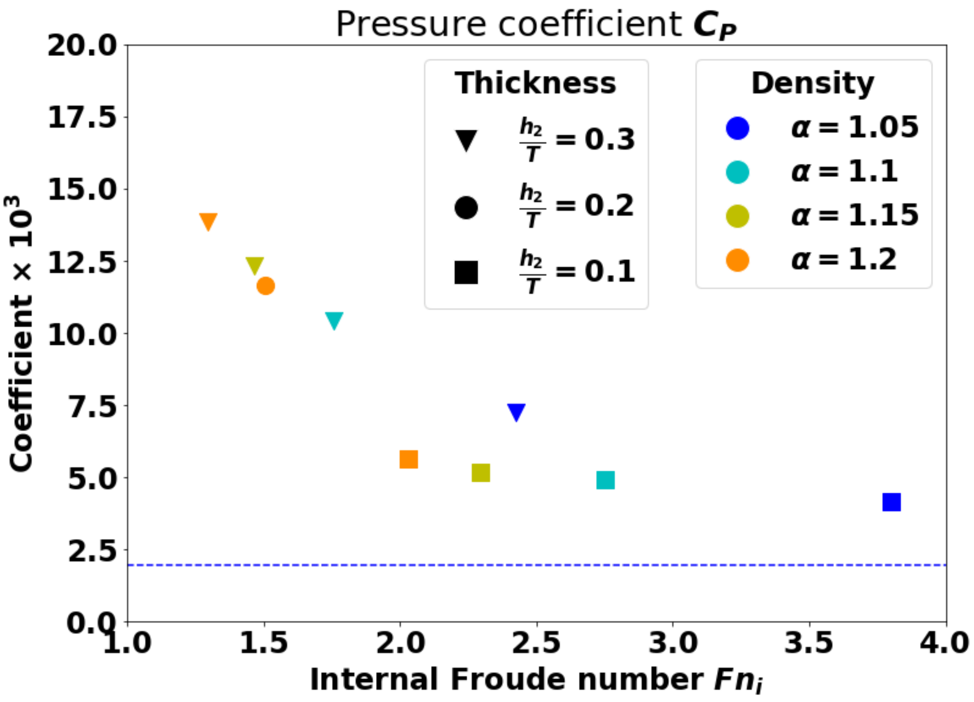

Figure 6.13: *Pressure resistance* against the internal Froude number for a flow with a mud layer with a yield stress of $\tau_y^* = 0.4$. The dashed line presents the ship resistance when sailing through only water.

Pressure resistance

The half-wedge angle seem not to be affected by the yield stress. This suggest that the yield stress does not affect the internal Froude number. Therefore, the pressure resistance is still expected to peak close to $Fn_i \approx 1$.

Fig. 6.13 shows the *pressure resistance* of the vessel for different cases with a mud yield stress of τ_y^*. Similar for sailing through the Newtonian mud, the *pressure resistance* indeed increases when sailing closer to the critical regime.

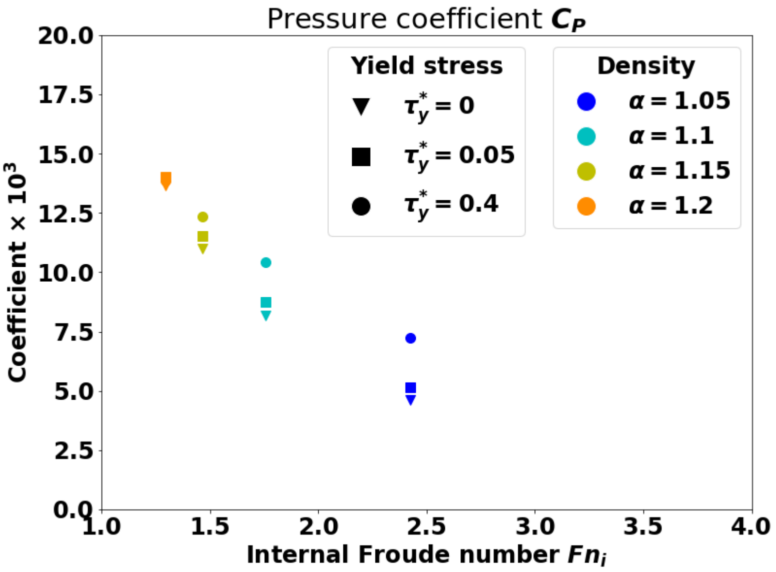

(a) Thick mud layer $\frac{h_2}{T} = 0.3$

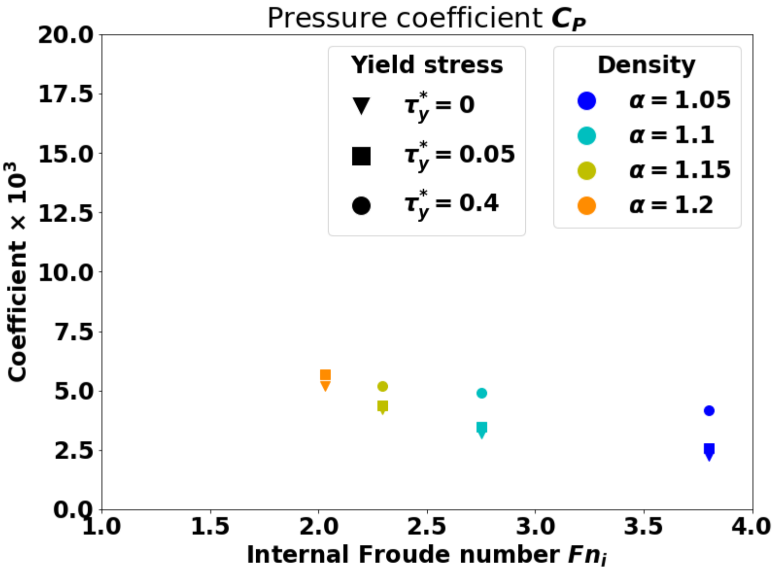

(b) Thin mud layer $\frac{h_2}{T} = 0.1$

Figure 6.14: Effect of mud yield stress on the *pressure resistance.*

Fig. 6.14 presents the *pressure resistance* for cases with different yield stress. The yield stress seems to influence the *pressure resistance* when the density ratios are low, independent of the mud layer thickness. Since both parameters are needed to determine the critical wave velocity, it is unlikely the pressure increase due to yield stress is influenced by the internal Froude number.

The influence of the yield stress on the pressure is also visible in the far critical regime, $Fn_i > 2.5$. When sailing through this regime, the *dead-water resistance* is expected to be negligible. Therefore, the increase in *pressure resistance* due to yield stress is most likely due to the *viscous pressure resistance*. This aligns with the conclusions from Section 5.3, which also showed an increase in *viscous pressure resistance* due to the mud yield stress.

The influence of yield stress is most visible for low mud density ratios. The reasons for this are unknown.

Frictional resistance

In contrast to the *pressure resistance*, the yield stress shows little effect on the *frictional resistance*. For the situation with a lower mud layer thickness, $\frac{h_2}{T} = 0.1$, the hull does not touch the mud layer. Therefore, the hull is surrounded fully with water. This explains why the frictional resistance is almost the same as for a ship sailing through only water.

The ship will sail through the mud layer for the thickest mud layer looked at, $\frac{h_2}{T} = 0.3$. Surprisingly, Fig. 6.15 shows that the *frictional resistance* still stays constant. This can be explained by the fact that the mud touching the hull will be sheared, causing the apparent viscosity of mud to be close to the viscosity of water. In addition, as the ship sails through the mud layer, the mud is pushed under the vessel. Fig. 6.16 shows the existence of a water cushion under the vessel. Due to the presence of this water cushion, a significant part of the surface of the hull is still covered by water.

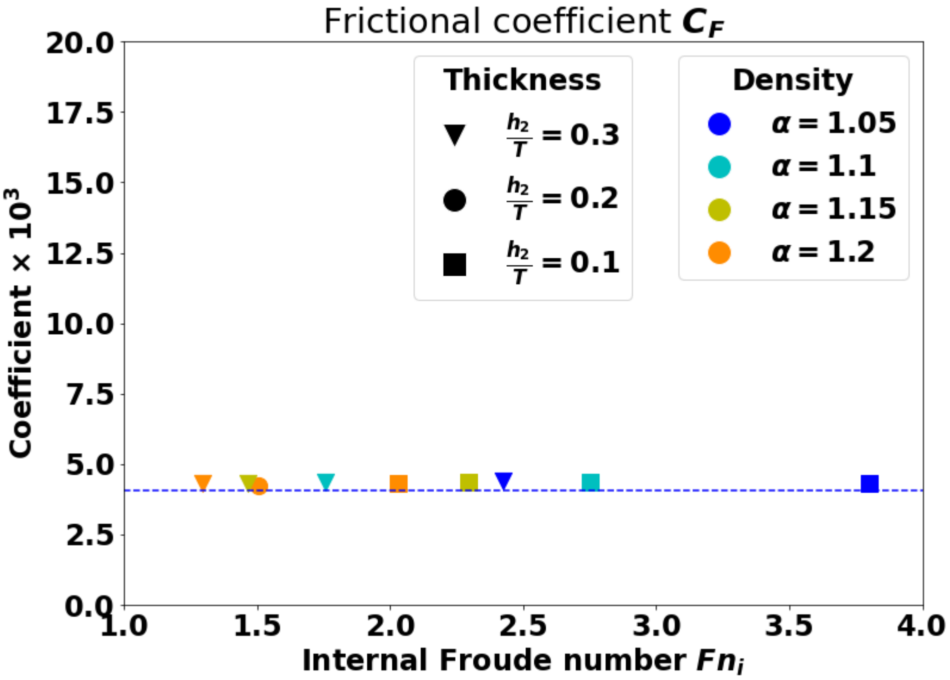

Figure 6.15: *Frictional resistance* against the internal Froude number for a flow with a mud layer with a yield stress of $\tau_y^* = 0.4$. The dashed line presents the ship resistance when sailing through only water.

Whether the water cushion below the vessel would happen in reality is in question. Due to the fixed vertical position of the hull, squat effects are not taken into account. It is known that sailing over a mud layer could reduce the squat effects, the ship could even rise [18]. Therefore, it is expected that the mud layer will not be as deformed and the ship will rise a little when sailing through shallow water with a fluid mud layer at the seabed. This squat effect will influence both the *pressure resistance* and the *frictional resistance*.

Figure 6.16: Water volume fraction at the symmetry plane for a flow with a Newtonian mud layer with a density of $\alpha = 1.2$ and a thickness of $\frac{h_2}{T} = 0.3$.

6.5. Conclusions

The resistance of a ship sailing through shallow water with a fluid mud layer at the seabed has been computed. The mud density, mud layer thickness and mud yield stress were varied. Solution verification is performed together with a check of the influence of the domain width.

The width of the domain influences the resistance. The current study used the smaller domain, which shows reflective waves and adds a blockage effect. Due to this blockage effect, the *total resistance* could be overestimated in this study. For future research it is advised to choose a broader domain.

The resistance of a ship sailing through shallow water seems to increase in the presence of a fluid mud layer. This increase in total resistance is due to the increase in *pressure resistance*, which consists out of the *viscous pressure resistance* and the *dead-water resistance*. Surprisingly, the *frictional resistance* does not seem to be influenced significantly by the presence of the mud layer, even with negative UKC.

For both, Newtonian and non-Newtonian mud, the increase in *pressure resistance* is largest when sailing close to the critical regime. This suggests the increase is due to the *dead-water resistance*. The *pressure resistance* can increase by more than 4 times compared to the resistance of a vessel sailing through only water. While this may appear excessive, a large increase in *dead-water resistance* close to $Fn_i \approx 1$ is also visible in previous research [1, 22, 63].

The yield stress seems to increase the *pressure resistance* only when the density ratio is low. This increase does not seem to be influenced by the mud layer thickness and is still visible in the far supercritical regime. This suggest the increase is due the *viscous pressure resistance*. The wave pattern is damped out when the mud has a yield stress, whereas the half-wedge angle of the internal wave does not seem to be influenced. Therefore, yield stress does not seem to influence the critical velocity of the internal wave and thus the internal Froude number.

The results are modelled without the air-water interface. It is possible the coupling between this interface and the water-mud interface influences the critical velocity of the water-mud interface and therefore the *dead-water resistance*. In addition, not taking into account the displacement of the ship in the vertical direction is expected to have influenced the total resistance.

7

Conclusions and Recommendations

This study focussed on ships sailing through shallow waters with a muddy seabed. The initial objective of this study was to test the ability of ReFRESCO to simulate and assess the influence of a fluid mud layer on the resistance of a ship. In this chapter, the main findings obtained are summarised and recommendations for futher research are given.

7.1. Conclusions

In this thesis, two situations are simulated: the single-phase and the two-phase simulations. The single-phase simulations focussed on a vessel sailing through only mud. The mud yield stress is increased to see the visco-plastic effect on the ship resistance. The main conclusions from the single-phase simulations can be summarized as follows:

- The *total resistance* overall increases as the yield stress increases.
- The *viscous pressure resistance* increases significantly when the yield stress increases. For a flow with high yield stress, the *viscous pressure resistance* is the most dominant contribution in the total force.
- The *frictional resistance* is highly dependent on the choice of turbulence model.

The two-phase simulations focussed on a vessel sailing through shallow water with a fluid mud layer on the seabed. The mud layer thickness, mud density and mud yield stress were varied. From these simulations, the following conclusions are drawn:

- The presence of a fluid mud layer on the seabed increases the resistance.
- The presence of a fluid mud layer does not show a significant influence in the *frictional resistance* regardless of the rheological model.
- The increase in *total resistance* is due to the *pressure resistance*, which consists of the *dead-water resistance*, or internal wave-making resistance, and the *viscous pressure resistance*.
- The *pressure resistance* peaks as the internal Froude number Fn_i defined by Miloh et al. [1] approaches 1. This suggest that the increase in resistance is due to the *dead-water resistance*. Close to the critical regime, $Fn_i \approx 1$, the *pressure resistance* can increase by almost 4 times compared to the resistance of a vessel sailing through full water. This is in agreement with potential flow theory [22, 63].
- The influence of the yield stress on the resistance is dependent on the density difference between the fluids. For low density differences, the *pressure resistance* can be affected by the yield stress. Yield stress does not seem to influence the results when the density difference is larger.

- The yield stress does not influence the half-wedge angle of the internal wave significantly. This suggests that the yield stress has no effect on the critical velocity of the wave. Therefore, the yield stress does not need to be taken into account when determining the internal Froude number Fn_i.

- The increase in mud yield stress does damp out the internal wave. In addition, a wave depression is formed behind the vessel for non-Newtonian mud.

7.2. Recommendations

The ability of ReFRESCO to simulate a ship sailing through shallow waters with a muddy seabed has been tested. However, there are a number of difficulties when simulating this situation. Based on those difficulties, a number of recommendations can be made for further research:

- Full-scale modelling
    - When modelling the full scale problem, the flow is more in turbulent regime. When increasing the yield stress, the amount of turbulence is expected to reduce. For full scale modelling, the chance of the flow going into transitional regime is smaller compared to model scale. Therefore, less difficulties are expected when using the RANS models at full scale.
    - In addition, it is not yet clear how to properly scale the mud properties to obtain realistic effects at model scale. Simulations at full scale will allow to use the real mud properties, thus without the need of scaling.

- More research into turbulence modelling for a non-Newtonian Flow
    - Modelling at full scale will partly help with better turbulence modelling. However, the accuracy of the turbulence models is still questionable when applied to non-Newtonian flow.

- Domain size
    - The domain size is more influential on the forces for shallow water and stratified flow than for deep water calculations. Therefore, it is advised to have a more elaborate study regarding the domain size. The position of the side boundary is most likely to influence the results due to reflecting waves. In addition, due to the depression in the mud behind the vessel when the mud yield stress increases, the influence of the position of the outlet should be checked.

- Effect of the air-water interface
    - In this research, the air-water interface was not modelled. Normally, the wave-making resistance due to the air-water interface is negligible when sailing at lower velocities. However, according to potential flow theory, there is a coupling effect between the air-water interface and the water-mud interface [2, 22]. This coupling effect is expected to have a significant influence on the *dead-water resistance* when sailing in the critical regime. It is advised to check the effects of the air-water interface on the forces on the ship around internal Froude number Fn_i of 1.

- More accurate modelling for mud
    - The shear-thinning effect is not taken into account in this research. This effect can be taken into account with the Herschel-Bulkley model by varying the flow index n. Based on the results on a sphere [88], the influence of the flow index on the resistance is expected to be similar to the influence of yield stress. However, there is no known literature on the effect on vessel resistance.

  - It is also possible to look at models capturing the time-dependent behaviour of fluid mud, thixotropy. However, the question remains whether this is needed. These models could be used to see the behaviour of the fluid mud over a longer period of time. For the current study, the thixotropy effects are expected to be negligible due to the small period it takes for the ship to sail over the mud layer.

- The squat effects
  - The squat effects of the vessel will be influenced by the mud layer [15, 18]. The squat effects could influence both the *pressure* and the *frictional resistance*. Therefore, there could be an indirect effect on the forces on the vessel due to yield stress when the squat effects are also taken into account.

A

Scaling and non-dimensional numbers

Within ship hydromechanics, it has always been a problem to extrapolate model scale results towards full scale results. The total ship resistance can be split into two components,viscous resistance F_v and wave resistance F_w. The viscous resistance is often determined by the form factor k_f as a ratio of the frictional resistance F_f. Hereby, the frictional resistance is depending on the Reynolds number and the wave resistance depends on the Froude number:

$$F_T(Fn, Rn) = (1+k_f)F_f(Rn) + F_w(Fn) \tag{A.1}$$

Since it is practically not possible to scale both the Froude and Reynolds number, Froude scaling laws are used:

$$\frac{V_{ship}}{\sqrt{gL_{ship}}} = \frac{V_{model}}{\sqrt{gL_{model}}} \tag{A.2}$$

$$L_{ship} = \alpha L_{model} \tag{A.3}$$

The quantities with the correct scaling can be found in table A.1. However, not all quantities are scaled. Viscosity, for instance, is not scaled due to the difficulties when performing model test and therefore the frictional resistance is determined based by empirical results of the flat plate resistance. The empirical results were used to determine the global trend in frictional resistance based on the corresponding Reynolds number. Eventually, the ITTC (International towing tank conference) in Madrid, 1957, made corrections to existing empirically determined formulas to take the form effects in to account. The following formula known as the ITTC-57 model-ship correlation line has been used in scaling practices:

$$C_{f,ITTC57} = \frac{0.075}{(\log Rn - 2)^2} \tag{A.4}$$

where the Reynolds number is:

$$Rn = \frac{\rho V L}{\mu} \tag{A.5}$$

Quantity		Scaling
Length	m	α
Velocity	m/s	$\sqrt{\alpha}$
time	s	$\frac{1}{\sqrt{\alpha}}$

Table A.1: Froude scaling for each quantity

This correlation is based on infinite water depths. When sailing through shallow waters, the friction on the hull is altered due to the shallow water effect. Zeng et al. [36] discusses the friction a 2D plate in shallow waters. It was shown that for low Reynolds numbers, the depth/length ratio will increase the friction of on the plate up to almost 50%. A new correlation line was proposed for the flat plate in shallow water:

$$C_{f,proposed} = \frac{0.08169}{(\log Rn - 1.717)^2} \times \left(1 + \frac{0.003998}{\log Rn - 4.393} \cdot \left(\frac{h}{L}\right)^{-1.083}\right) \tag{A.6}$$

To account for the form effects, the total frictional component in shallow water can be written as:

$$C_f = C_{f,ITTC57} + (C_{f,proposed} - C_{f,deep}) \cdot \frac{S_{bottom}}{S_{total}} \cdot \frac{V_{bottom}}{V_{free-stream}}^2 \tag{A.7}$$

Due to the presence of a fluid mud layer, current scaling laws could change. Due to the stratification, the use of the density and viscosity are not uniform anymore, making it difficult to determine the frictional resistance as calculated by equation A.4 when the hull would touch the mud layer. Therefore, a weighted approach can be used as described by Delefortrie [19], either for the frictional coefficient,

$$C_{f,total} = C_{f,water} \frac{S_{wa,water}}{S_{wa,total}} + C_{f,mud} \frac{S_{wa,mud}}{S_{wa,total}} \tag{A.8}$$

or by weighting the Reynolds number:

$$Rn_{weighted} = \frac{VL}{S_{wa,total}} \left(\frac{S_{wa,water}\rho_{water}}{\mu_{water}} + \frac{S_{wa,mud}\rho_{mud}}{\mu_{mud}}\right) \tag{A.9}$$

In addition, the mud has a yield strength that needs to be overcome. The effect of this yield strength also changes over the scale of the problem, therefore a non-dimensional parameter is needed to put this effect into perspective. A known parameter is the Bingham number,

$$Bm = \frac{\tau_{Bm} L}{\mu V} \tag{A.10}$$

which is the ratio between the yield stress and viscous stresses. However, since viscous stresses are seldom scaled in the extrapolation of model scale data to full scale data in ship hydromechanics, this may not be the right scaling parameter to use. The yield stress could also be scaled by the ratio between the forces due to the yield stress and the inertia forces, which is called Yield Reynolds number:

$$Rn_y = \frac{\rho V^2}{\tau_y} \tag{A.11}$$

Other non-dimensional parameters influencing the problem of sailing though stratified flow are as said in the report the Brunt-Vaisala frequency and the Richardson number:

$$N = \sqrt{-\frac{g}{\rho_0}\frac{\partial \rho}{\partial z}} \tag{A.12}$$

$$Ri_g = \frac{-(\frac{g}{\rho_0}\frac{d\rho}{dz})}{(\frac{du}{dz})^2} \tag{A.13}$$

These non-dimensional parameters will become more important when looking at a case for which the density gradually increases over depth. In this research, however, the interface is modelled as a sharp interface.

B

Grid generation in Hexpress

This appendixes focuses gives a description on how the grids used in this research are generated.

NUMECA's grid generator Hexpress (numeca.com) is used to generate the grids. The grids are first build for a domain that is 6 ship lengths long (2 lengths before the vessel, 3 after), 2 ship lengths wide and 1.2 times the draft of the vessel deep. After building the grids, the domain size is increased by expanding the grid one ship length at the inlet.

A total of four grids are generated for the solution verification. These grids need to have geometrical similarity, which is difficult for unstructured grids (see chapter 4). The method described by Crepier [84] is used to get close to geometrical similar grids.

Hexpress generates a grid with five separate steps: initial mesh, adapt to geometry, snap to geometry, optimise and adding viscous layers. The initial refinement of the domain for four grids is given in B.1. In the second step, adapt to geometry, additional refinement can be added in the domain. This is needed to capture the flow around the complex shape which is the hull. Therefore, the ships geometry is split into 5 different parts, as shown in figure B.1. In addition, volume refinement is used around the whole ship and the transom, aft and bow of the vessel. This is illustrated in figure B.2. The different refinement levels of the surfaces and the additional refined volumes is found in tables B.2 and B.3 respectively. For the final grids, the grid is expanded by one ship length at the inlet.

Table B.1: Initial refinement for the different grids as well as the diffusion depth.

Grid	1	2	3	4
X-direction	150	300	450	600
Y-direction	50	100	150	200
Z-direction	4	8	12	16
Diffusion depth	1	3	5	7

Table B.2: Refinement levels of the different hull surfaces.

	Surface names	refinement levels
a)	Transom	4
b)	Aft	3
c)	Mid ship	2
d)	Fore Ship	3
e)	Bow	4

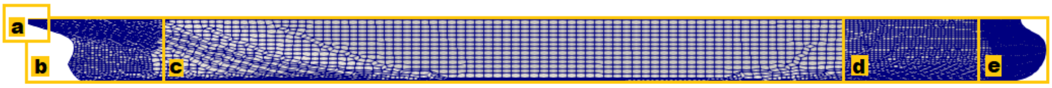

Figure B.1: Definition of the different surfaces on the ship.

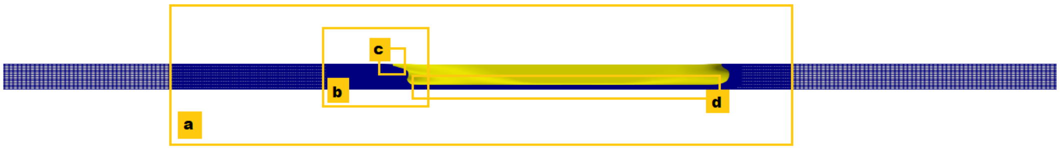

Figure B.2: Definition of the different refinement boxes around the ship.

Table B.3: Refinement levels in the additional volumes around the hull.

	Box name	refinement levels
a)	Ship	1
b)	Wake	3
c)	Box Transom	3
d)	Bow keel	4

The third and fourth step will make sure the grid is close to the geometry and the grid is optimized to get a better quality. The last step is to add refinement close to a wall to capture the boundary layer. This refinement is added by estimating a correct first cell height and the stretching ratio. The stretching ratio is the relation between a cell height and the cell height in the following layers. The input for the generation of the viscous layer is Hexpress is given in table B.4.

Table B.4: Refinement specifications in the boundary layer

Grid	1	2	3	4
First layer thickness	2.1552E-05	1.0285E-05	6.7520E-06	5.0253E-06
Stretching ratio	1.2000	1.0954	1.0627	1.0466
Layers	29-34	50-60	70-83	85-107

The size of the four grids used in the grid refinement study can be found in table 5.1. The dimensionless first cell height y^+ of these grids sailing through a Newtonian fluid can be found in table B.5. For the actual calculations the second finest grid is used. This grid is visualised in figure B.3.

Table B.5: y^+ for different grids through Newtonian fluid

Grid	y^+_{max} for the hull	y^+_{avr} for the hull	y^+_{max} for the bottom	y^+_{avr} for the bottom
4	0.102	0.068	158.645	11.605
3	0.143	0.091	203.302	14.813
2	0.196	0.137	280.153	20.752
1	0.400	0.271	459.279	35.825

The boundary layer around the hull can be captured well, since y^+ is less than 5. However, the first cell heights at the bottom boundary are quite high (see Table B.5). To refine the entire bottom, it would have cost a large number of additional cells. The extra refinement below the hull, however, is needed to capture the flow. In addition, the refinement under the hull wauss added to improve the convergence.

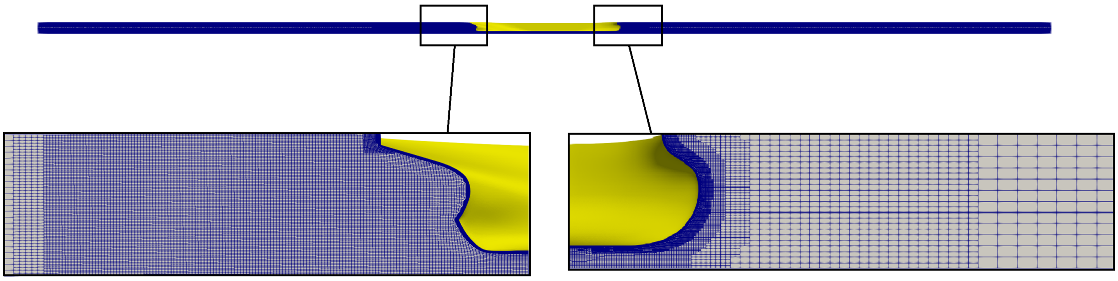

Figure B.3: Final grid used in the single-phase simulations.

The influence of the position of the inlet is also checked. For this check, three grids are generated using the second finest grid. The first domain has four ship lengths in front of the bow, the second three (like the final grid) and the last two. The grid size of these grids can be found in table C.1. The influence of the position of the inlet is discussed in Appendix C.

B.1. Free surface

An additional surface is placed at the height of 0.0455 m to refine around the water-mud interface when modelling the thickest mud layer, $\frac{h_2}{T} = 0.3$. Due to the small depth of the domain, the refinement at this level also refined around the other mud levels. The number of refinements, as used in Hexpress, is set at 1. A higher refinement level would have resulted in more cells and this would have costed too much computational effort.

C

Position of the inlet

The position of the inlet is checked by taking three different distances between the inlet and the bow of the ship and looking for the influence on the forces and flow patterns.

Two additional grids have been made to see the influence of the inlet position in reference to the ship on the resistance. The specifics of these grids are shown in Table C.1.

Table C.1: Grids used to determine the influence of the position of the inlet.

Position of the inlet from vessel	number of cells in volume ($\times 10^{-6}$)	$r_i = 4 \cdot L_{pp} / i \cdot L_{pp}$
2×L	10.71	2.000
$3 \times L$	**10.84**	**1.330**
4×L	10.98	1.000

The original grid has a distance of 3 times the ship length from bow to inlet. The other two grids have a distance of 2 and 4 times the ship length. From the forces of the three different grid, an uncertainty of the results can be determined with the procedure as proposed by Eça and Hoekstra [87]. The different results for the forces as well as the uncertainty determined are shown in Table C.2. The uncertainty due to the position of the inlet for the grid used is 2.3% and this decreases when the yield stress increases using the SST model. The uncertainty in pressure is mostly decreasing as the yield stress increases. This low uncertainty suggest less influence of the position of the inlet.

The uncertainty due to the position of the inlet is very significant when using the KSKL turbulence model when sailing through a non-Newtonian fluid. The reasons for this are unknown.

Table C.2: Uncertainty due to the position of the inlet for total resistance coefficient C_T

	$C_F \times 1000$	U_{inlet,C_F}	$C_P \times 1000$	U_{inlet,C_P}	$C_T \times 1000$	U_{inlet,C_T}
$\tau_y^* = 0$						
SST	4.201	1.00%	2.113	8.20%	6.314	2.30%
KSKL	4.114	0.90%	1.969	1.50%	6.083	1.10%
$\tau_y^* = 0.2$						
SST	4.404	0.70%	4.528	0.30%	8.932	0.50%
KSKL	3.066	51.0%	3.700	70.3%	6.765	11.7%

D

Discretisation error in the pressure resistance

Section 5.2 showed a large discretisation uncertainty for the pressure resistance. This appendix will give a more elaborate explanation for this large uncertainty.

The uncertainties for all four grids are shown in table D.1. The uncertainty of the total resistance coefficient is shown in figure D.1.

Table D.1: Uncertainty per grid using the SST model

	$C_P \cdot 10^3\,[-]$	$U_{C_P}\,[\%]$	$C_F \cdot 10^3\,[-]$	$U_{C_F}\,[\%]$	$C_T \cdot 10^3\,[-]$	$U_{C_T}\,[\%]$
$\tau = 0\ [Pa]$						
Grid 1	2.307	26.12%	4.186	1.38%	6.494	8.66%
Grid 2	2.113	35.78%	4.201	1.80%	6.314	11.86%
Grid 3	2.046	40.31%	4.179	3.34%	6.225	13.83%
Grid 4	2.129	35.78%	4.058	11.16%	6.187	14.56%

The discretisation uncertainty for the pressure resistance is around 35%. As discussed in Section 5.2, the pressure resistance is high since it is actually the sum of two large forces, which each there own discretisation errors. Since the two large forces sum up to a smaller force, these errors are more visible.

To check whether this uncertainty is actually exaggerated, the pressure resistance is divided into two part: pressure at the bow and the aft of the ship. For these forces, the uncertainty is recalculated as shown in figure D.2. The uncertainties are shown to be lower. However, the uncertainty for the pressure force at the aft is still above the 15-20 %. The most likely cause of the high uncertainty for the pressure forces at the aft is due to the transom. The grid quality around the transom is not as good as the rest of the grid, since it is difficult to capture the separation and reversed flow.

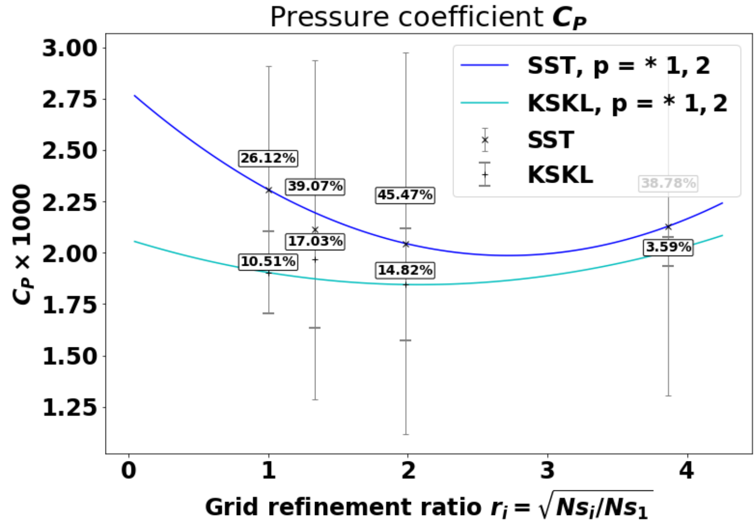

(a) Pressure coefficient

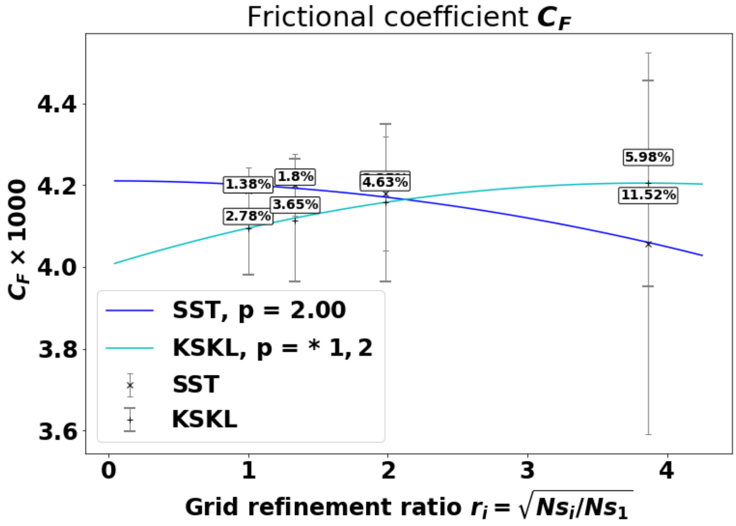

(b) Frictional coefficient

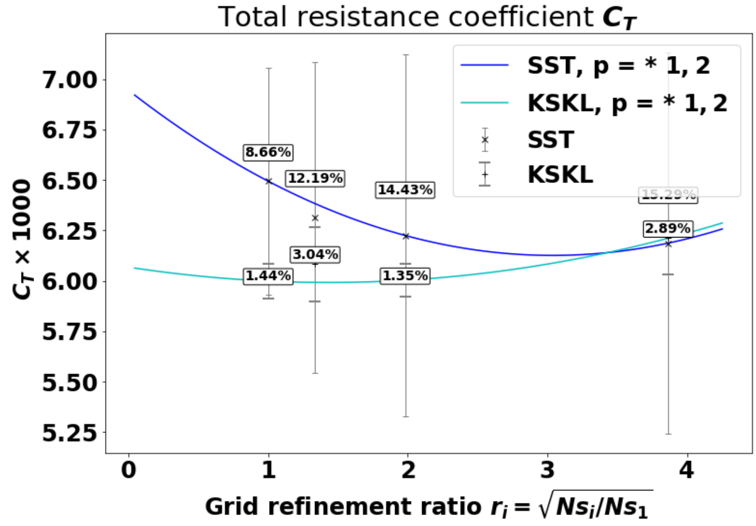

(c) Total viscous force coefficient

Figure D.1: Discretisation uncertainty for the different forces of the vessel sailing through a fluid with no yield stress.

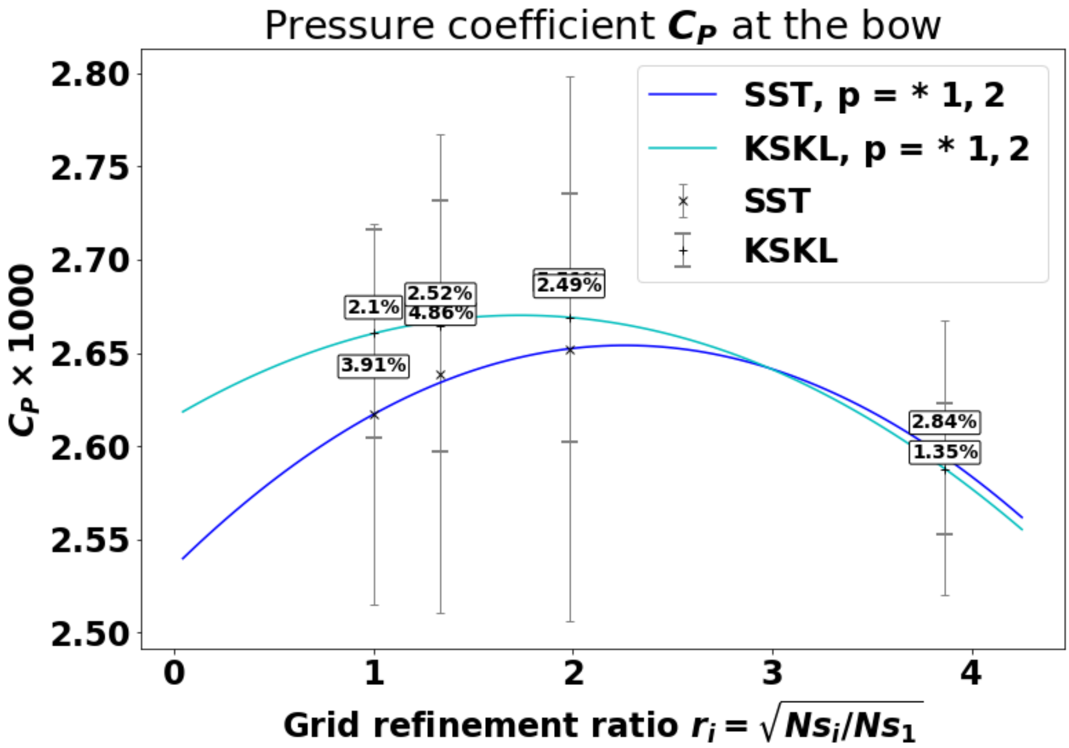

(a) Pressure coefficient of force at the bow

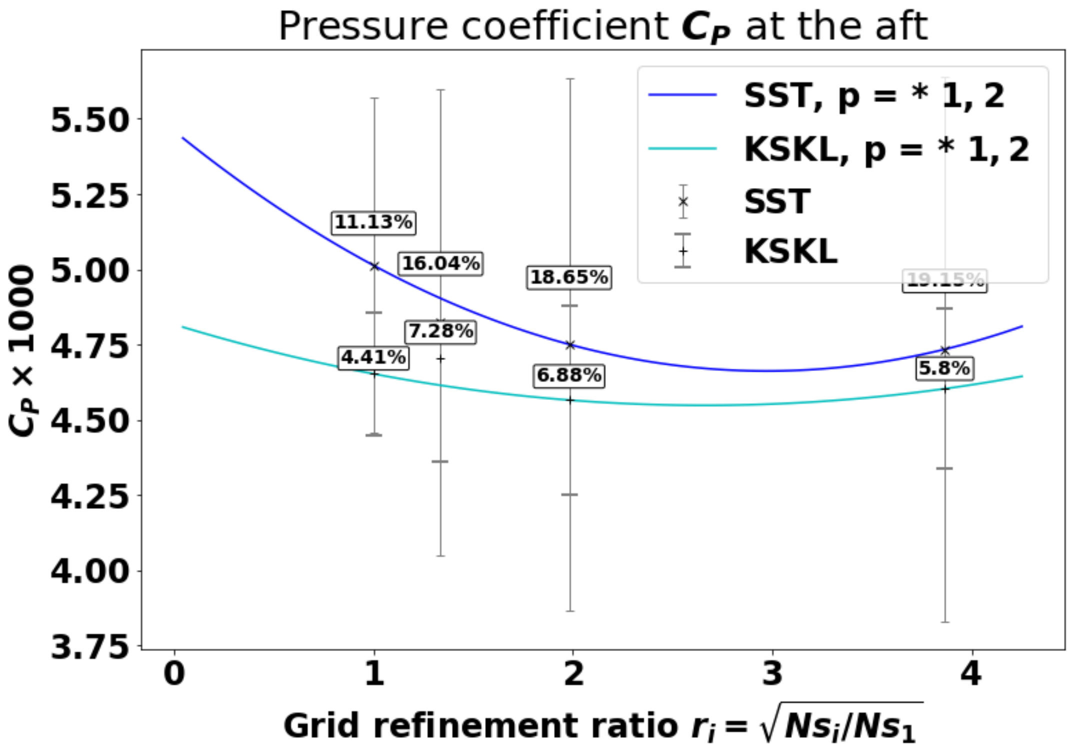

(b) Pressure coefficient of force at the aft

Figure D.2: Uncertainty of the pressure forces when sailing through a Newtonian fluid.

E

Influence of the regularisation parameter

This appendix discusses the influence of the regularisation parameter. The regularisation parameter is used to model a continuous Bingham fluid, as discussed in Section 3.2. The regularised Bingham model is repeated as:

$$\boldsymbol{\tau} = 2\left[\frac{\tau_0(1-e^{-m\dot{\gamma}})}{\dot{\gamma}} + k\right]\boldsymbol{S} \tag{E.1}$$

The regularisation parameter m $[s]$ influences the maximum apparent viscosity which can be reached. If m goes to infinity, the model is exactly like the Bingham model, as shown in Appendix E. The lower the regularisation parameter, the less high the maximum apparent viscosity will be, which is equal to $\tau_y \cdot m$. Therefore, this regularisation parameter can influence the flow field and the resistance.

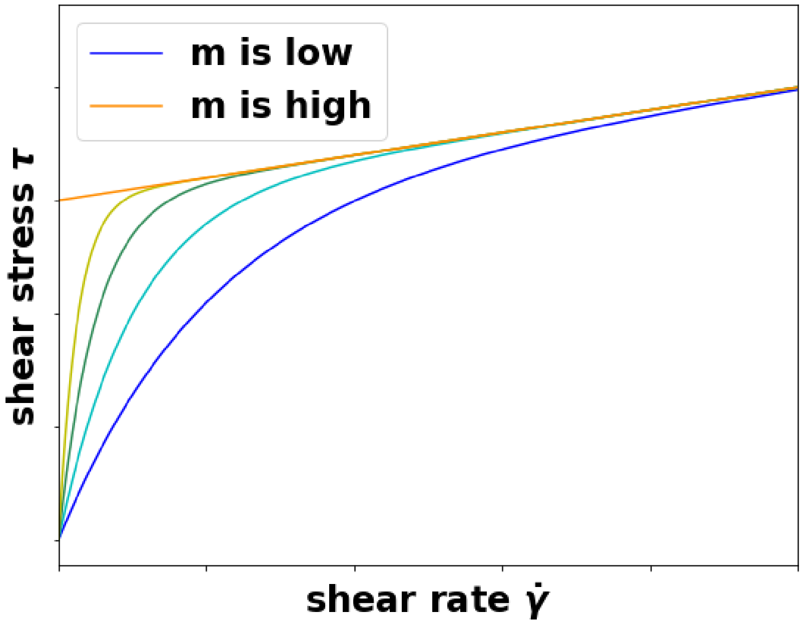

Figure E.1: Example of the influence of the regularisation parameter on the shear stress.

E.1. Single-phase simulations

The influence of the regularisation parameter on the resistance for the single-phase simulations is shown in Table E.1. The increase in regularisation parameter causes a increase of almost 10% in viscous pressure resistance. The frictional resistance is affected less, it decreases by less than 1% when the regularisation parameter increases.

Table E.1: Influence of the regularisation parameter on the resistance of a ship sailing through full mud

	C_P	C_F	C_T
m=10 seconds	9.08	6.79	15.87
m=20 seconds	10.07	6.74	16.81

E.2. Two-phase simulations

The regularisation parameter is expected to influence the flow field and resistance less for the two-phase simulations since the mud covers less of the domain. The computations with $\frac{h_2}{T} = 0.3$, $\frac{1}{\alpha} = 1.2$ and $\tau_y^* = 0.4$ are performed using three different regularisation parameters: 20 seconds, 40 seconds, 80 seconds.

The influence of the regularisation parameter on the resistance and the wave-pattern are visualised in Table E.2 and Appendix E.2. Both show little influence in the results.

Table E.2: Influence of the regularisation parameter on the ship resistance

	C_P	C_F	C_T
m=20 seconds	13.92	4.33	18.25
m=40 seconds	13.87	4.33	18.20
m=80 seconds	13.88	4.33	18.21

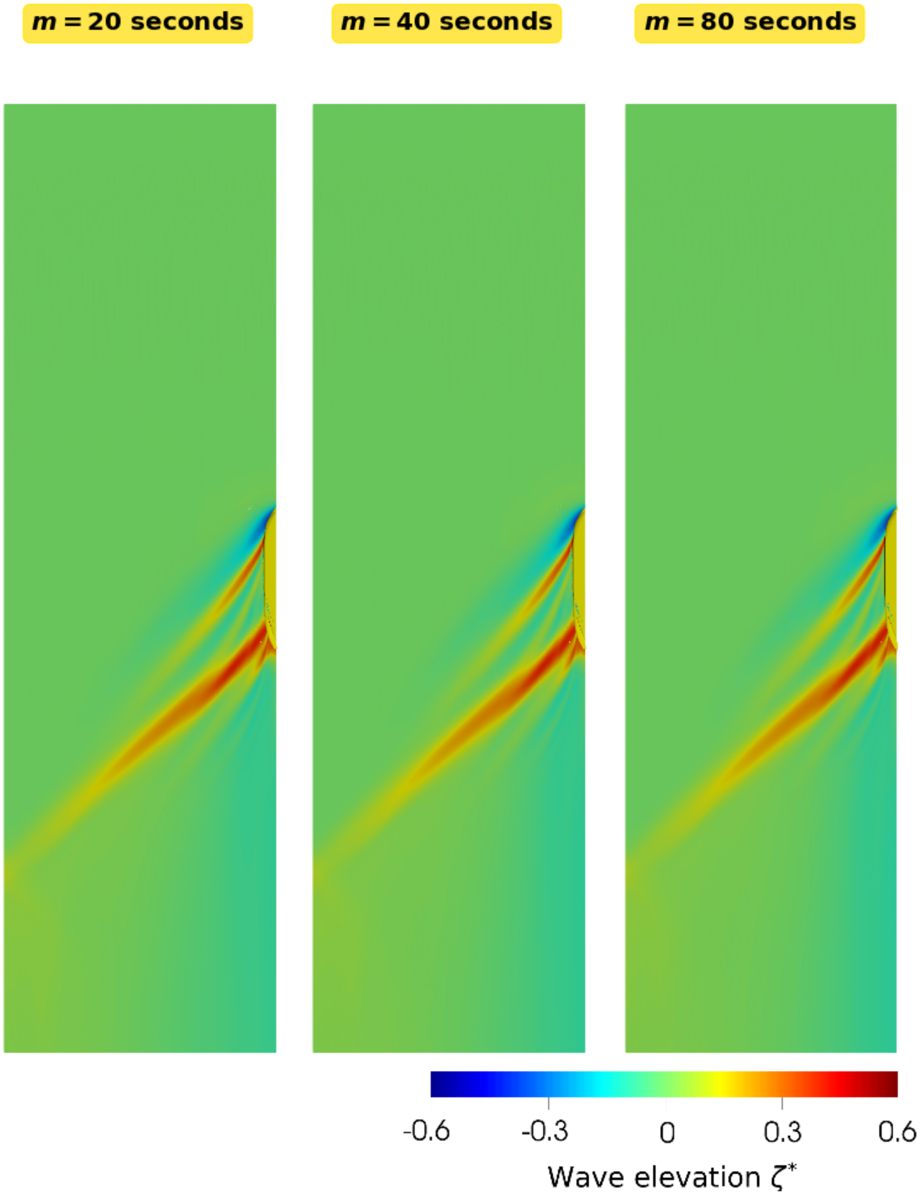

Figure E.2: Wave patterns of a fluid with a density ratio of $\frac{1}{\alpha} = 1.2$, a mud layer thickness of $\frac{h_2}{T} = 0.3$ and a yield stress of $\tau_y^* = 0.4$.

F

Different inflow velocity

This appendix shows the effect of adjusting the ship velocity. For lower velocities, the wave height decreased significantly. To capture the lower wave-heights, the grid needed more refinement. Therefore, this is not described in the actual thesis.

The decrease in wave height for lower ship velocities is shown in Appendix F. For a lower velocity, the flow is more critical. This is also visible in the wave pattern. The resistance of the ship sailing at different velocities is shown in Table F.1. Since the flow is more critical, the pressure resistance also seems to increase.

For the two cases with Froude numbers of $Fn = 0.032$ and $Fn = 0.016$, the wave patterns are not being captures properly due to the lack of refinement. Therefore, the forces are expected to be highly influenced by the discretisation.

Table F.1: Influence of the regularisation parameter on the ship resistance

	C_P	C_F	C_T
Fn=0.064	13.64	4.44	18.08
Fn=0.048	18.56	4.16	22.71
Fn=0.032	8.15	4.81	12.96
Fn=0.016	11.10	5.02	16.12

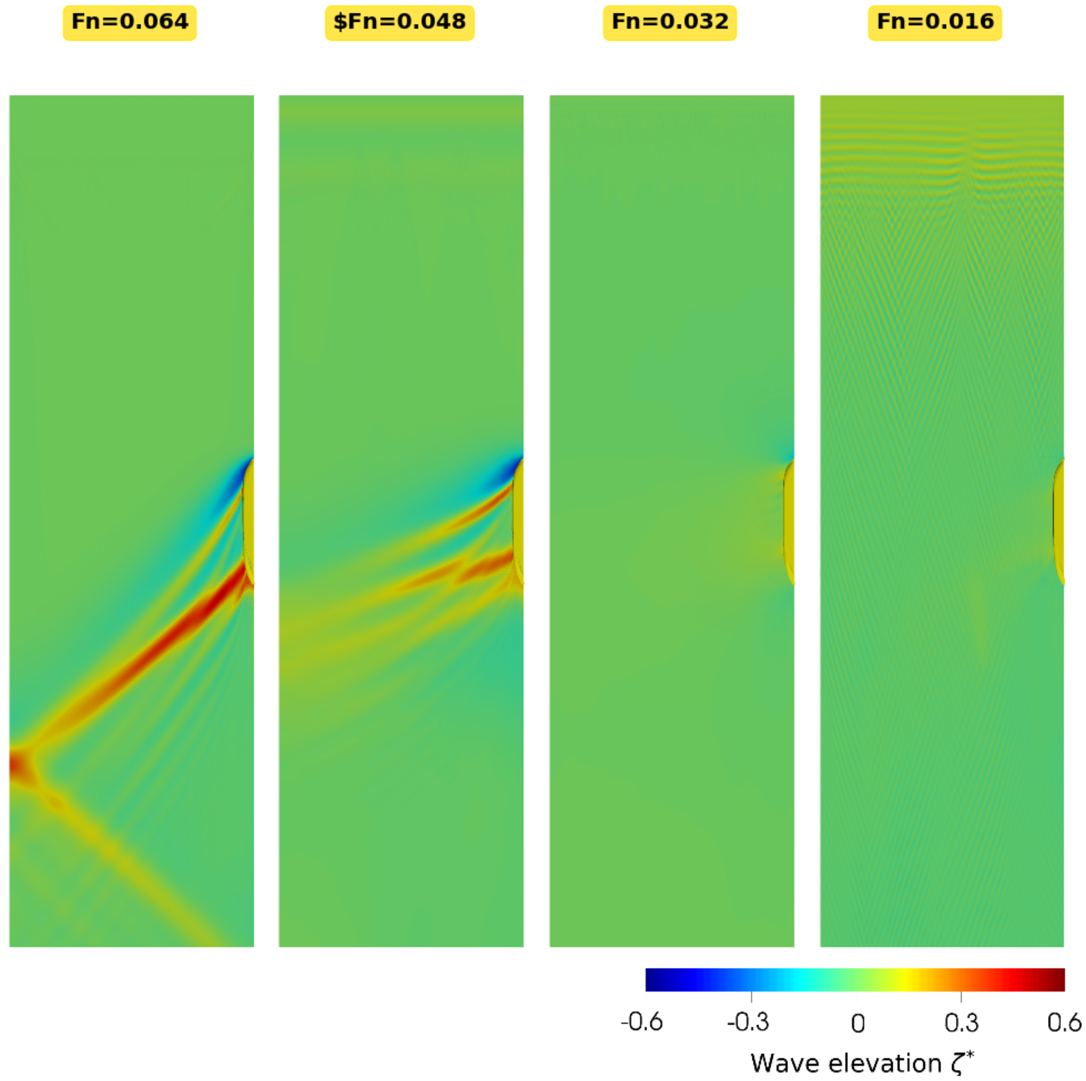

Figure F.1: Wave patterns with a Newtonian mud layer with different velocity.

G

Different mud viscosity

Chapter 6 discussed the influence of yield stress on the results. Based on literature [20, 30, 60, 63, 64], a changing viscosity should influence the dead-water resistance. Where some say the resistance only damps out the wave[20, 63, 64], others discuss the influence of the viscosity on the internal Froude number Kaidi et al. [30], Delefortrie and Vantorre [60]. If viscosity would influence the internal Froude number, this should be visible in the wave pattern.

Calculations are performed with four different consistency parameter K and no yield stress. The wave patterns are shown in Appendix G and the resistance is shown in Fig. G.1. It shows that even though the wave pattern damps out, the wave angle stays constant. In addition, the pressure resistance stays constant. This does not mean the dead-water resistance will stay constant, however, the viscosity shows little to no influence on the internal Froude number. This contradicts the statement made by Kaidi et al. [30] who said that higher viscosity should influence the internal wave pattern and therefore the dead-water resistance. It is possible that this difference is due to the influences of confinement.

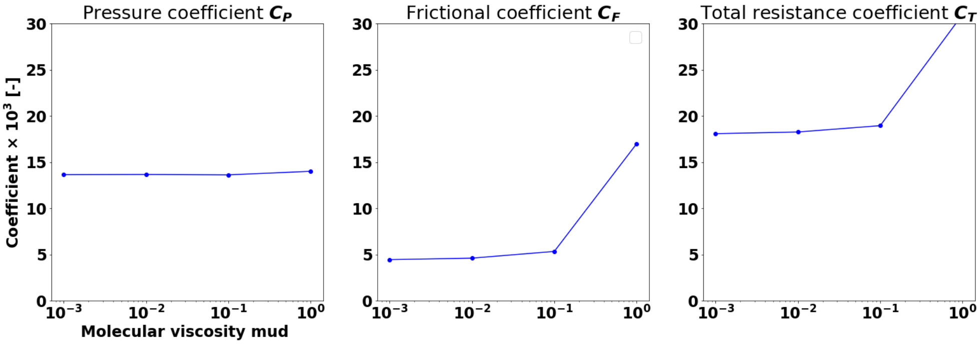

Figure G.1: Ship's resistance versus molecular viscosity.

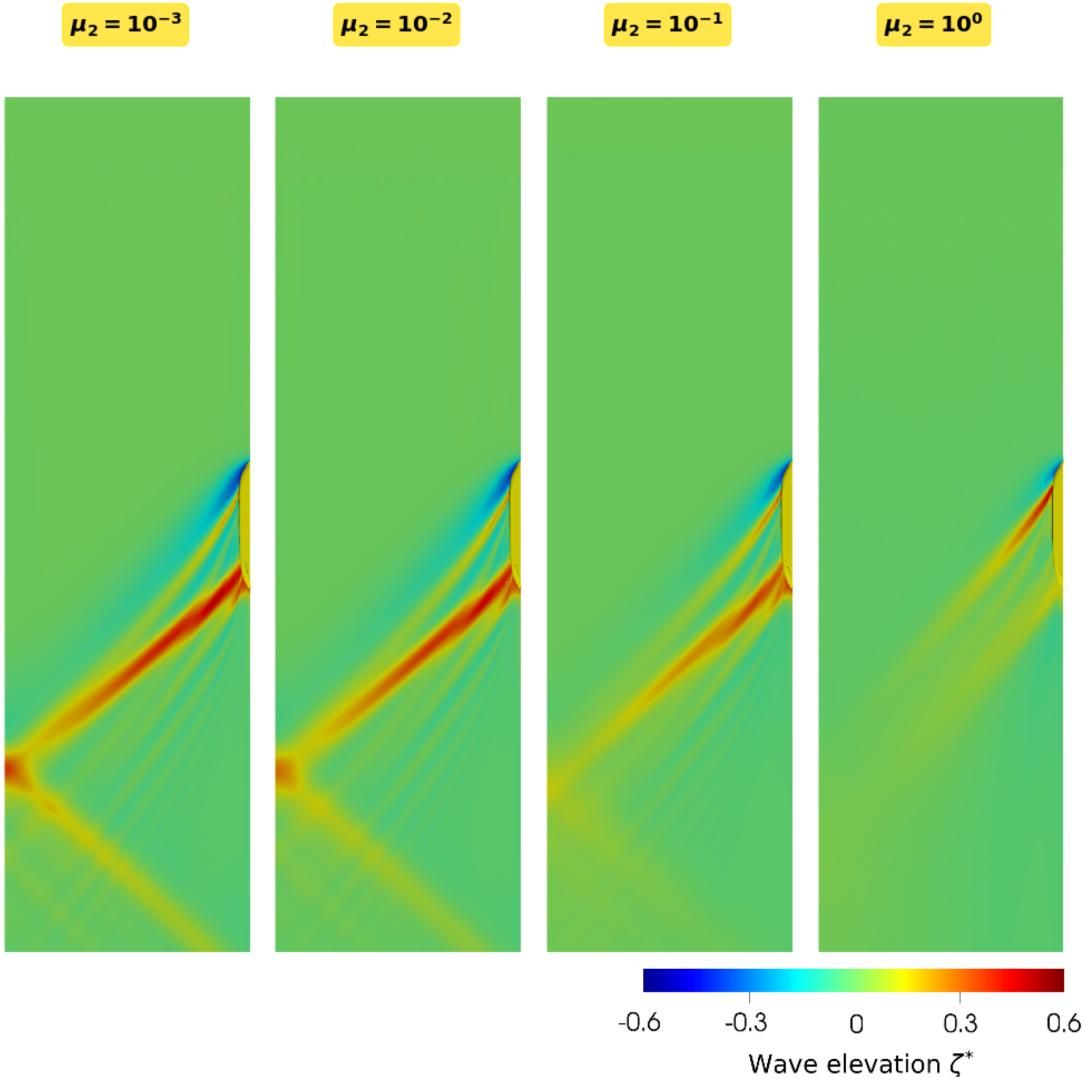

Figure G.2: Wave patterns with a Newtonian mud layer with different viscosity.

Bibliography

[1] T. Miloh, M. P. Tulin, and G. Zilman. Dead-Water Effects of a Ship Moving in Stratified Seas. *Journal of Offshore Mechanics and Arctic Engineering*, 115(2):105–110, 1993. `http://dx.doi.org/10.1115/1.2920098`.

[2] R. W. Yeung and T. C. Nguyen. Waves generated by a moving source in a two-layer ocean of finite depth. *Journal of Engineering Mathematics*, 35(1-2):85–107, 1999.

[3] M. Vantorre. Ship behaviour and control at low speed in layered fluids. *International Symposium on Hydro- and Aerodynamics in Marine Engineering HADMAR '91*, pages 5.1–5.9, 1991. `http://hdl.handle.net/1854/LU-225851`.

[4] Central Dredging Association (CEDA). Ecosystem Services and Dredging and Marine Construction. Technical report, 2013. `https://dredging.org/media/ceda/org/documents/resources/cedaonline/2013-07-ecosystemservices.pdf`.

[5] PIANC. Report No . 121 Harbour Approach Channels Design Guidelines. Technical report, 2014.

[6] J. Berlamont, M. Ockenden, E. Toorman, and J. Winterwerp. The characterisation of cohesive sediment properties. *Coastal Engineering*, 21(1-3):105–128, 1993. `http://dx.doi.org/10.1016/0378-3839(93)90047-C`.

[7] A. J. Mehta. An Introduction to Hydraulics of Fine Sediment Transport, volume 38 of *Advanced Series on Ocean Engineering*. 2013. `http://dx.doi.org/10.1142/8708`.

[8] A. Kirichek, A. Shakeel, and C. Chassagne. Using in situ density and strength measurements for sediment maintenance in ports and waterways. *Journal of Soils and Sediments*, 20(6):2546–2552, 2020. `http://dx.doi.org/10.1007/s11368-020-02581-8`.

[9] X. Ma, A. Kirichek, K. Heller, and D. Draganov. Seismic Reflection Investigations of Fluid Mud : Laboratory Tests for Layer-Specific Characterization. *EAGE Annual*, 2020. `http://dx.doi.org/10.3997/2214-4609.202011418`.

[10] W. H. McAnally, A. Teeter, D. Schoellhamer, C. Friedrichs, D. Hamilton, E. Hayter, P. Shrestha, H. Rodriguez, A. Sheremet, and R. Kirby. Management of Fluid Mud in Estuaries, Bays, and Lakes. II: Measurement, Modeling, and Management. *Journal of Hydraulic Engineering*, 133(1):23–38, 2007. `http://dx.doi.org/10.1061/(ASCE)0733-9429(2007)133:1(23)`.

[11] R. Kirby, W. Parker, and W. Oostrum. Definition of the seabed in navigation routes through mud areas. *International Hydrographic Review*, 57(1):107–117, 1980.

[12] G. Delefortrie, M. Vantorre, and E. Laforce. Revision of the nautical bottom concept in Zeebrugge based on the manoeuvrability of deep-drafted container ships. *Dredging: the extremes: CEDA dredging days 2005, Rotterdam, the Netherlands, 2-4 November 2005: proceedings*, 2004.

[13] R. W. Wurpts. 15 years experience with fluid mud: Definition of the nautical bottom with rheological parameters. *Terra et Aqua*, (99):22–32, 2005.

[14] A. Kirichek. Water injection dredging and fluid mud trapping pilot in the port of Rotterdam. *CEDA Dredging Days*, 2019.

[15] R. Sellmeijer and G. Van Oortmersen. The effect of mud on tanker manoeuvres. *Royal institution of Naval Architects Transactions*, 126, 1983.

[16] K. van Craenenbroeck, M. Vantorre, and P. de Wolf. Navigation in muddy areas: establishing the navigate depth in the port of Zeebrugge. *CEDA-PIANC Conference*, 1992.

[17] R. Barth, C. J. A. W. van der Made, L. Bourgonjen, J. van Dijken, M. Vantorre, and J. Verwilligen. Manoeuvring with negative underkeel clearance: 2nd full scale field test in the port of Delftzijl. *International Conference on Ship Manoeuvring in Shallow and Confined Water with Special Focus on Ship Bottom Interaction (MASHCON)*, pages 262–271, 2016.

[18] C. Brossard, A. Delouis, P. Galichon, J. Granboulan, and P. Monadier. Navigability in Channels Subject to Siltation Physical Scale Model Experiments. *Coastal Engineering*, volume 3, pages 3088–3101, New York, NY, 1991. American Society of Civil Engineers. `http://dx.doi.org/10.1061/9780872627765.236`.

[19] G. Delefortrie. Manoeuvring behaviour of container vessels in muddy navigation areas. PhD thesis, Ghent University, 2007.

[20] G. Zilman and T. Miloh. Hydrodynamics of a body moving over a mud layer - Part I: wave resistance. *Journal of Ship Research*, 39(3):194–201, 1995.

[21] G. Zilman, T. Miloh, and L. J. Doctors. Influence of a bottom mud layer on the resistance of marine vehicles. *Ship Technology Research*, 43(2):51–61, 1996.

[22] M. Sano and Y. Kunitake. Numerical solution for a ship-wave problem in a two-layer fluid using a double-model linearised interface condition. *Ships and Offshore Structures*, 13(3):293–302, 2018. `http://dx.doi.org/10.1080/17445302.2017.1371391`.

[23] J. Jachowski. Assessment of ship squat in shallow water using CFD. *Archives of Civil and Mechanical Engineering*, 8(1):27–36, 2008. `http://dx.doi.org/10.1016/S1644-9665(12)60264-7`.

[24] S. L. Toxopeus. Practical application of viscous-flow calculations for the simulation of manoeuvring ships. 2011. ISBN 9789075757057.

[25] T. Tezdogan, A. Incecik, and O. Turan. A numerical investigation of the squat and resistance of ships advancing through a canal using CFD. *Journal of Marine Science and Technology*, 21(1):86–101, 2016. `http://dx.doi.org/10.1007/s00773-015-0334-1`.

[26] Q. Zeng. A method to improve the prediction of ship resistance in shallow water. Doctoral thesis, Delft University of Technology, 2019.

[27] Y. Chang, F. Zhao, J. Zhang, F.-W. Hong, P. Li, and J. Yun. Numerical simulation of internal waves excited by a submarine moving in the two-layer stratified fluid. *Journal of Hydrodynamics*, 18(S1):323–329, 2006. `http://dx.doi.org/10.1007/BF03400467`.

[28] M. Esmaeilpour, J. Ezequiel Martin, and P. M. Carrica. Computational Fluid Dynamics Study of the Dead Water Problem. *Journal of Fluids Engineering*, 140(3):1–8, 2018. `http://dx.doi.org/10.1115/1.4037693`.

[29] Z. Gao, H. Yang, and M. Xie. Computation of Flow around Wigley Hull in Shallow Water with Muddy Seabed. *Journal of Coastal Research*, 73:490–495, 2015. `http://dx.doi.org/10.2112/si73-086.1`.

[30] S. Kaidi, E. Lefrançois, and H. Smaoui. Numerical modelling of the muddy layer effect on Ship's resistance and squat. *Ocean Engineering*, 199:106939, 2020. `http://dx.doi.org/10.1016/j.oceaneng.2020.106939`.

[31] L. Larsson and H. C. Raven. Ship resistance and flow. Principles of Naval Architecture. The Society of Naval Architects and Marine Engineers, 2010. ISBN 978-0-939773-76-3.

[32] F. M. White. Fluid Mechanics. McGraw-Hill Education, 7nd editio edition, 2011. ISBN 978-007-131121-2.

[33] ITTC Manoeuvring Committee. Captive Model Test - ITTC. *ITTC Quality System Manual Recommended Procedures and Guidelines*, pages 1–26, 2017.

[34] T. H. Havelock. The propagation of groups of waves in dispersive media, with application to waves on water produced by a travelling disturbance. *Royal Society of London. Series A, Containing Papers of a Mathematical and Physical Character*, 81(549):398–430, 1908. `http://dx.doi.org/10.1098/rspa.1908.0097`.

[35] ITTC. Resistance Uncertainty Analysis, Example for Resistance Test. *ITTC-Recommended Procedures*, 2002.

[36] Q. Zeng, C. Thill, R. Hekkenberg, and E. Rotteveel. A modification of the ITTC57 correlation line for shallow water. *Journal of Marine Science and Technology*, 24(2):642–657, 2019. `http://dx.doi.org/10.1007/s00773-018-0578-7`.

[37] H. C. Raven. A computational study of shallow-water effects on ship viscous resistance. *29th Symposium on Naval Hydrodynamics*, (August):26–31, 2012.

[38] A. Millward. Effect of water depth on hull form factor. *International Shipbuilding Progress*, 36(407), 1989.

[39] A. F. Molland, S. R. Turnock, and D. A. Hudson. Ship Resistance and Propulsion. Cambridge University Press, Cambridge, 2017. `http://dx.doi.org/10.1017/9781316494196`.

[40] S. L. Toxopeus. Viscous-Flow Calculations for KVLCC2 in Deep and Shallow Water. volume 29, pages 151–169. 2013. `http://dx.doi.org/10.1007/978-94-007-6143-8_9`.

[41] T. Constantine. On the movement of ships in restricted waterways. *Journal of Fluid Mechanics*, 9(2): 247–256, 1960. `http://dx.doi.org/10.1017/S0022112060001080`.

[42] H. J. de Koning Gans and H. Boonstra. Squat effects of very large container ships with drift in a harbor environment. *International Maritime-Port Technology and Development Conference, MTEC2007*, number September, pages 613–620, 2007.

[43] E. O. Tuck. Shallow-water flows past slender bodies. *Journal of Fluid Mechanics*, 26(01):81, 1966. `http://dx.doi.org/10.1017/S0022112066001101`.

[44] P. Mucha, O. el Moctar, and C.-U. Böttner. Technical Note: PreSquat – Workshop on Numerical Prediction of Ship Squat in Restricted Waters. *Ship Technology Research*, 61(3):162–165, 2014. `http://dx.doi.org/10.1179/str.2014.61.3.004`.

[45] K. Elsherbiny, M. Terziev, T. Tezdogan, A. Incecik, and M. Kotb. Numerical and experimental study on hydrodynamic performance of ships advancing through different canals. *Ocean Engineering*, 195(August 2019):106696, 2020. `http://dx.doi.org/10.1016/j.oceaneng.2019.106696`.

[46] J. Bechthold and M. Kastens. Robustness and quality of squat predictions in extreme shallow water conditions based on RANS-calculations. *Ocean Engineering*, 197:106780, 2020. `http://dx.doi.org/10.1016/j.oceaneng.2019.106780`.

[47] M. Esmaeilpour, J. E. Martin, and P. M. Carrica. Near-field flow of submarines and ships advancing in a stable stratified fluid. *Ocean Engineering*, 123:75–95, 2016. `http://dx.doi.org/10.1016/j.oceaneng.2016.06.038`.

[48] A. A. Hudimac. Ship waves in a stratified ocean. *Journal of fluid mechanics*, 11(2):229–243, 1961. `http://dx.doi.org/10.1017/S0022112061000482`.

[49] G. D. Crapper, Hudimac, and G. D. Crapper. Ship waves in a stratified ocean. *Journal of Fluid Mechanics*, 29(4):667–672, 1967. `http://dx.doi.org/10.1017/S0022112067001107`.

[50] T. Radko. Ship Waves in a Stratified Fluid. *Journal of Ship Research*, 45(1):1–12, 2001.

[51] J. Grue. Nonlinear dead water resistance at subcritical speed. *Physics of Fluids*, 27(8):082103, 2015. `http://dx.doi.org/10.1063/1.4928411`.

[52] M. J. Mercier, R. Vasseur, and T. Dauxois. Resurrecting dead-water phenomenon. *Nonlinear Processes in Geophysics*, 18(2):193–208, 2011. `http://dx.doi.org/10.5194/npg-18-193-2011`.

[53] J. Fourdrinoy, J. Dambrine, M. Petcu, M. Pierre, and G. Rousseaux. The dual nature of the dead-water phenomenology: Nansen versus Ekman wave-making drags. *Proceedings of the National Academy of Sciences*, 117(29):16770–16775, 2020. `http://dx.doi.org/10.1073/pnas.1922584117`.

[54] A. Shakeel, A. Kirichek, and C. Chassagne. Is density enough to predict the rheology of natural sediments? *Geo-Marine Letters*, 39(5):427–434, 2019. http://dx.doi.org/10.1007/s00367-019-00601-2.

[55] A. J. Mehta, F. Samsami, Y. P. Khare, and C. Sahin. Fluid mud properties in nautical depth estimation. *Journal of Waterway, Port, Coastal and Ocean Engineering*, 140(2):210–222, 2014. http://dx.doi.org/10.1061/(ASCE)WW.1943-5460.0000228.

[56] K. Liu and C. C. Mei. Effects of wave-induced friction on a muddy seabed modelled as a Bingham-plastic fluid. *Journal of Coastal Research*, 5(4):777–789, 1989.

[57] J. Winterwerp. Scaling parameters for High-Concentrated Mud Suspensions in tidal flow. *Proceedings in Marine Science*, volume 5, pages 171–186. Elsevier B.V., 2002. http://dx.doi.org/10.1016/S1568-2692(02)80015-8.

[58] R. Haldenwang, P. T. Slatter, and R. P. Chhabra. Laminar and transitional flow in open channels for non-Newtonian fluids. *15th International Conference on Hydrotransport*, (m):755–768, 2002.

[59] J. H. Burger, R. Haldenwang, and N. J. Alderman. Laminar and turbulent flow of non-newtonian fluids in open channels for different cross-sectional shapes. *Journal of Hydraulic Engineering*, 141(4), 2015. http://dx.doi.org/10.1061/(ASCE)HY.1943-7900.0000968.

[60] G. Delefortrie and M. Vantorre. Ship manoeuvring behaviour in muddy navigation areas : state of the art. pages 26–36. Bundesanstalt für Wasserbau, 2016. http://dx.doi.org/10.18451/978-3-939230-38-0{_}4.

[61] V. Ferdinande and M. Vantorre. The behaviour of a mud-water interface underneath a slowly advancing ship at small keel clearance. *Proceedings of the International Symposium on Hydro- and Aerodynamics in Marine Engineering HADMAR '91*, pages [4–1]–[4–10], Varna, Bulgaria, 1991. http://lib.ugent.be/catalog/pug01:225836.

[62] G. Delefortrie, M. Vantorre, K. Eloot, J. Verwilligen, and E. Lataire. Squat prediction in muddy navigation areas. *Ocean Engineering*, 37(16):1464–1476, 2010. http://dx.doi.org/10.1016/j.oceaneng.2010.08.003.

[63] T. Miloh. Ship motion in non-homogeneous media. *Ship Technology Research*, 42(3):140–156, 1995.

[64] L. Doctors, G. Zilman, and T. Miloh. The Influence of a Bottom Mud Layer on the Steady-State Hydrodynamics of Marine Vehicles. *Twenty-First Symposium on Naval Hydrodynamics*, chapter 50, pages 727–742. The National Academies Press, 1997. https://www.nap.edu/read/5870/chapter/50.

[65] P. Kundu, I. Cohen, and D. Dowling. Fluid Mechanics. Elsevier, 2016. http://dx.doi.org/10.1016/C2012-0-00611-4.

[66] J. H. Ferziger, M. Perić, and R. L. Street. Computational Methods for Fluid Dynamics. Springer International Publishing, Cham, 2020. http://dx.doi.org/10.1007/978-3-319-99693-6.

[67] S. B. Pope. Turbulent Flows. Cambridge University Press, 2000. http://dx.doi.org/10.1017/CBO9780511840531.

[68] R. P. Chhabra and J. Richardson. Chapter 1. Non-Newtonian fluid behaviour. *Non-Newtonian Flow and Applied Rheology: Engineering Applications*, page 536. 2011. ISBN 0080951600. https://books.google.com/books?id={_}6nnoh9PtF0C{&}pgis=1.

[69] P. Coussot and J. M. Piau. On the behavior of fine mud suspensions. *Rheologica Acta*, 33(3):175–184, 1994. http://dx.doi.org/10.1007/BF00437302.

[70] T. C. Papanastasiou. Flows of Materials with Yield. *Journal of Rheology*, 31(5):385–404, 1987. http://dx.doi.org/10.1122/1.549926.

[71] S. Lovato, S. L. Toxopeus, J. W. Settels, G. H. Keetels, and G. Vaz. Code Verification of Non-Newtonian Fluid Solvers for Single- and Two-Phase Laminar Flows. *Journal of Verification, Validation and Uncertainty Quantification*, 6(2), 2021. http://dx.doi.org/10.1115/1.4050131.

[72] C. Hirt and B. Nichols. Volume of fluid (VOF) method for the dynamics of free boundaries. *Journal of Computational Physics*, 39(1):201–225, 1981. `http://dx.doi.org/10.1016/0021-9991(81)90145-5`.

[73] G. Vaz, F. Jaouen, and M. Hoekstra. Free-Surface Viscous Flow Computations: Validation of URANS Code FreSCo. *Volume 5: Polar and Arctic Sciences and Technology; CFD and VIV*, volume 39, pages 425–437. ASMEDC, 2009. `http://dx.doi.org/10.1115/OMAE2009-79398`.

[74] C. M. Klaij, M. Hoekstra, and G. Vaz. Design, analysis and verification of a volume-of-fluid model with interface-capturing scheme. *Computers and Fluids*, 170:324–340, 2018. `http://dx.doi.org/10.1016/j.compfluid.2018.05.016`.

[75] L. Eça, P. S. Pereira, and G. Vaz. Viscous flow simulations at high Reynolds numbers without wall functions: Is $y^{+}1$ enough for the near-wall cells? *Computers & Fluids*, 170:157–175, 2018. `http://dx.doi.org/10.1016/j.compfluid.2018.04.035`.

[76] F. R. Menter, M. Kuntz, and R. Langtry. Ten Years of Industrial Experience with the SST Turbulence Model Turbulence. *Heat and Mass transfer*, 4:625–632, 2003. `https://cfd.spbstu.ru/agarbaruk/doc/2003{_}Menter,Kuntz,Langtry{_}TenyearsofindustrialexperiencewiththeSSTturbulencemodel.pdf{%}0A`.

[77] F. R. Menter and Y. Egorov. The Scale-Adaptive Simulation Method for Unsteady Turbulent Flow Predictions. Part 1: Theory and Model Description. *Flow, Turbulence and Combustion*, 85(1):113–138, 2010. `http://dx.doi.org/10.1007/s10494-010-9264-5`.

[78] N. Waterson and H. Deconinck. Design principles for bounded higher-order convection schemes – a unified approach. *Journal of Computational Physics*, 224(1):182–207, 2007. `http://dx.doi.org/10.1016/j.jcp.2007.01.021`.

[79] C. Hirsch. Structured and Unstructured Grid Properties. *Numerical Computation of Internal and External Flows*, pages 249–277. Elsevier, 2007. `http://dx.doi.org/10.1016/B978-075066594-0/50047-3`.

[80] S. Patankar and D. Spalding. A calculation procedure for heat, mass and momentum transfer in three-dimensional parabolic flows. *International Journal of Heat and Mass Transfer*, 15(10):1787–1806, 1972. `http://dx.doi.org/10.1016/0017-9310(72)90054-3`.

[81] C. M. Klaij and C. Vuik. SIMPLE-type preconditioners for cell-centered, colocated finite volume discretization of incompressible Reynolds-averaged Navier-Stokes equations. *International Journal for Numerical Methods in Fluids*, 71(7):830–849, 2013. `http://dx.doi.org/10.1002/fld.3686`.

[82] D. C. Wilcox. Turbulence modeling for CFD. 1993.

[83] ITTC Quality system group. Practical Guidelines for Ship Resistance CFD. *ITTC Quality System Manual Recommended Procedures and Guidelines*, 2014.

[84] P. Crepier. Ship resistance prediction: Verification and validation exercise on unstructured grids. *7th International Conference on Computational Methods in Marine Engineering, MARINE 2017*, 2017-May:365–376, 2017.

[85] A. L. Rocha, L. Eça, and G. Vaz. On the numerical convergence properties of the calculation of the flow around the KVLCC2 tanker in unstructured grids. Technical report, 2017.

[86] The Americam Society of Mechanical Engineers (ASME). Standard for Verification and Validation in Computational Fluid Dynamics and Heat Transfer. Technical report, 2009.

[87] L. Eça and M. Hoekstra. A procedure for the estimation of the numerical uncertainty of CFD calculations based on grid refinement studies. *Journal of Computational Physics*, 262:104–130, 2014. `http://dx.doi.org/10.1016/j.jcp.2014.01.006`.

[88] A. A. Gavrilov, K. A. Finnikov, and E. V. Podryabinkin. Modeling of steady Herschel–Bulkley fluid flow over a sphere. *Journal of Engineering Thermophysics*, 26(2):197–215, 2017. `http://dx.doi.org/10.1134/S1810232817020060`.